A STUDY OF LOWER HYBRID WAVE PROPAGATION ON THE VERSATOR II TOKAMAK USING MICROWAVE SCATTERING

by

Rajeev Rajan Rohatgi

M.Sc., Indian Institute of Technology, Bombay (1980)

Submitted to the Department of Physics in Partial Fulfillment
of the Requirements for the Degree of

DOCTOR OF PHILOSOPHY

at the

MASSACHUSETTS INSTITUTE OF TECHNOLOGY

May 1986

Signature of Author ______________________
Department of Physics
December 1985

Certified by ______________________
Prof George Bekefi
Thesis Supervisor

Accepted by ______________________
Prof George Koster
Chairman, Departmental
Graduate Committee

Section [2]

TABLE OF CONTENTS

A STUDY OF LOWER HYBRID WAVE PROPAGATION ON THE VERSATOR II TOKAMAK USING MICROWAVE SCATTERING

by

Rajeev Rohatgi

Submitted to the Department of Physics on May 2, 1986 in partial fulfillment of the requirements for the Degree of Doctor of Philosophy in Physics.

Abstract

A 139 GHz microwave scattering diagnostic is used to study the penetration of externally launched 0.8 GHz lower hybrid waves in current drive ($\bar{n}_e \lesssim 6 \times 10^{12} cm^{-3}$) experiments on MIT's Versator II tokamak. A 7 W Extended Interaction Oscillator is used to provide the incident 139 GHz beam. Waveguide optics are used. The scattered signal is measured by means of a homodyne detection technique using a balanced mixer, with a spectrum analyzer as the IF detector. The receiver noise is under 10^{-13} W in a 300 kHz bandwidth; however, the experimental sensitivity is usually limited by background plasma emission. Various scattering geometries are available. The 0.8 GHz lower hybrid waves are launched using a 150 kW klystron and a phased 4 waveguide grill.

A variety of experiments has been performed. Our results indicate a spatially defined resonance cone near the edge of the plasma, with very directional power flow that is in excellent agreement with theoretical modelling. Power does reach the plasma center; some evidence of wave absorption during current drive is seen. Wavenumber spectra and frequency spectra have also been measured. Some data has been taken at densities outside the current drive regime. A major discrepancy between theory and experiment is the measured power levels, which are low by 2-3 orders of magnitude.

Experimental setup, procedure, analysis, results, and the theoretical modelling are all described in some detail.

Thesis Supervisor: George Bekefi
Title: Professor of Physics

Section [4] ACKNOWLEDGMENT

The Versator lab has been an excellent place to work. I do not think I could have asked for better, either in terms of enthusiastic, able, and easy-to-get-along-with people or in terms of facilities.

My foremost debt of gratitude is to Kuo-In Chen, who was my partner during almost all of my experimental runs. I really do not know what shape my experiment and myself would have been in, were it not for his selfless generosity and willingness to help me. Second, I must thank Ed Fitzgerald, our senior technical staff member, from whom I have probably learnt more than from any other individual (well, except my parents, I guess). He has also been an invaluable ally, willing to tackle any problem with resourcefulness and good humor.

Prof George Bekefi has supported me and trusted me through thick and thin; I would especially like to thank him for the opportunity I have had to work with this group. I would also like to thank Prof Miklos Porkolab and Stan Luckhardt for their encouragement and guidance. The students and staff of Versator have over the years been both good friends and colleagues; I would like to acknowledge with gratitude the willing help and support I have received from

Tom Evans
Alan Fisher
Kirk Hackett
Bob Kaplan
Steve Knowlton
Jerry Lorden
Ivan Mastovsky
Scott McDermott
Alan Palevsky
Burton Richards
Adam Sapirstein
Joel Villasenor

with special mention for Matt Mayberry, who has been my fellow graduate student, neighbor, and close friend for the last five years, as we have gone through the ups and downs of graduate life.

There have been occasions when I have had to seek the assistance of others to help me with some specific problem. Without exception, they have helped me generously. Paul Bonoli provided me with his ray tracing code and helped me a lot with difficulties I ran into while doing the theoretical modelling. Others I would like to thank include Jack Barrett, Mike Doucette, Cliff Surko, Dave Taylor and Paul Woskoboinikow. I would also like to take this opportunity to thank two faculty members who, although not associated with my experiment, have taught me a lot: Prof Jeff Freidberg and Prof Robert Kyhl.

And lastly my gratitude to my parents and my numerous friends over the years for just being there. (Ken and Joel*, this includes you !)

Section [5] LIST OF FIGURES

Radial Scans

$N_\parallel$ Spectra

($N_\parallel$ Spectra)

Section [6] LIST OF TABLES

Section [7] NOTATION

a	minor radius of plasma
a	subscript denoting plasma edge
a,b,c	coefficients in lower hybrid dispersion relation
a,b,c,d	constants used in k-resolution calculation
b	wall radius (theoretical model)
b	subscript denoting vacuum vessel wall
c	speed of light
e	electron charge
e	subscript denoting electrons
$\hat{e}$	unit vector
f	wave phase
$f(\vec{r})$	radiation pattern of transmitting antenna
f	lower hybrid wave frequency (0.8 GHz)
$g(\vec{r})$	radiation pattern of receiving antenna
i	subscript denoting ions
j	square root of -1, used in wave phase terms
k	Boltzmann's constant
$\vec{k}$	wavevector
k_r k_θ	components of $\vec{k}$ in scattering plane
$k_\parallel$ $k_\perp$	components of $\vec{k}$ relative to total magnetic field $\vec{B}$
$\vec{k}_I$	wavevector of incident beam
$\vec{k}_S$	wavevector of scattered beam
$\vec{k}_W$	wavevector of wave responsible for scattering
l	path length
m_e	electron mass

n n_e	electron density
$\bar{n},\bar{n}_e$	line average electron density
$\tilde{n}_e$	fluctuating electron density (as due to lower hybrid wave)
o,0	subscript denoting plasma center
r	minor radius coordinate in scattering plane
$\hat{r}$	radial unit vector
$\vec{r}$	spatial coordinate in scattering volume
r_m	radius of magnetic surface (~ magnetic coordinate)
r_o	classical electron radius
t	time
t_1	retarded time to first order approximation
$\vec{v}$	fluid velocity
$\vec{v}_e$	electron drift velocity
x,y	orthogonal coordinates in scattering plane (not horizontal and vertical)
x_I	coordinate along incident beam
x_S	coordinate along scattered beam
$\hat{z}$	unit toroidal vector

A_R	effective area of receiving antenna
A_W	cross-sectional area of lower hybrid beam, measured normal to $\hat{r}$
A,B,C,D,X	constants in $\vec{k}$-resolution calculation
B B_T	toroidal magnetic field
B	bandwidth
B_R	receiver bandwidth
B_W	bandwidth of lower hybrid waves
$C(\vec{K})$	Fourier transform of antenna pattern overlap $f(\vec{r})g(\vec{r})$

C_L	transmission loss of receiving waveguide
$\vec{E}$	electric field
$\vec{E}'$	' designates fields for (artificial) complex incident wave
$\vec{E}_O$	electric field amplitude
$\vec{E}_S$	total scattered electric field
$\vec{E}_{S1}$	scattered electric field due to single electron
F	electronics calibration factor (dB/Volt)
F_2	dimensionless quantity relating wave density amplitude to electric field amplitude
F_3	dimensionless quantity relating electric field amplitude squared to wave power (Poynting flux)
G	preamplifier gain
$H(\vec{k}_\perp)$	lower hybrid dispersion relation solution for $k_\parallel$
$\vec{H}_S$	total scattered magnetic field
$\vec{H}_{S1}$	scattered magnetic due to single electron
I, I_P	plasma current
$\hat{I}(N_\parallel)$	lower hybrid wave power per unit area, per unit $N_\parallel$, per unit launched power
I_I	inductively driven part of plasma current
I_R	RF driven part of plasma current
J	geometric factor related to $\vec{k}$-resolution of scattering volume
L	inductance of plasma current
L	mixer conversion loss
$\vec{N}$	refractive index
$N_\parallel$	parallel refractive index of lower hybrid wave
P	power
P,S,D	plasma quantities in Stix' notation

P_C	CW transmitted power with system aligned
P_L	launched lower hybrid power
P_S	measured scattered power (absolute units)
$\hat{P}_S$	measured scattered power (in units of receiver noise power)
R	plasma resistance
R	$\lvert\vec{R}\rvert$
$\hat{R}$	unit vector in $\vec{R}$ direction
$\vec{R}$	vector from scattering volume to (far) field point
R_R	distance from scattering volume to receiving antenna
R_X	distance from scattering volume to transmitting antenna
S_e	lower hybrid wave Poynting flux in direction $\hat{e}$
S_I	Poynting flux of incident beam at scattering volume
S_R	Poynting flux of incident beam at receiving antenna
T	time interval for received scattered power
T_e	electron temperature
T_i	ion temperature
T_N	signal noise temperature
T_R	receiver noise temperature
V_E	recorded voltage with 0.8 GHz system off (emission + noise)
V_L	loop voltage
V_N	recorded voltage corresponding to noise level
V_S	recorded voltage with 0.8 GHz system on (scattering + emission + noise)
X	constant in k-resolution calculation
α	orientation angle between $\vec{k}_\perp$ and $\hat{r}$

α	angle appearing in calculation of scattering volume's $\vec{k}$-resolution
$\Delta\omega$	frequency broadening (HWHM) of lower hybrid waves by density fluctuations
ε_0	permittivity of vacuum
θ	angle coordinate in scattering plane
θ_{RE}	halfwidth of receiving antenna pattern in E plane; subscripts x for transmitting antenna and H for H plane
θ_S	scattering angle
$\xi_n\ \xi_e\ \xi_i$	form factors for density and temperature profiles
τ	retarded time
τ	optical depth for scattering of lower hybrid waves by density fluctuations
$\psi(\omega)$	(scattered) spectral intensity
ω	(angular) frequency
ω_{ce}	electron cyclotron frequency
ω_{ci}	ion cyclotron frequency
ω_I	incident beam frequency
ω_{pe}	electron plasma frequency
ω_{pi}	ion plasma frequency
ω_S	frequency of scattered wave

Section [8] INTRODUCTION

A lot of interest in recent years has been focused on the phenomenon of lower hybrid current drive in tokamaks, as a means of obtaining steady state operation. Tokamaks depend on toroidal current for equilibrium; the radially inward pinch force (parallel filaments of current attract each other) balances the radially outward force due to the pressure gradient. Conventionally this toroidal current is generated inductively. However, inductively driven (DC) currents cannot be sustained indefinitely; this restricts tokamaks to be inherently pulsed devices. In contrast, RF driven currents may be sustained indefinitely, thus opening up the possibility of CW tokamak operation. CW operation, of course, tremendously enhances the attractiveness of the tokamak as a fusion reactor.

The basic idea of lower hybrid RF current drive is that one launches 'slow' lower hybrid waves (phase velocity less than the speed of light) travelling in the direction of electron drift. These waves interact with the plasma and transfer momentum to resonant electrons (enhancing the tail of the electron velocity distribution), thus driving current.

Lower hybrid current drive was proposed by Fisch in 1978 [Fisch.78], and first observed experimentally on JFT-2 in Japan [Yamamoto.80] and Versator II in the US

[Luckhardt.81]. In initial experiments, current was sustained with both inductive and RF drives simultaneously; the RF current drive effect was inferred from the drop in loop voltage $V_L = \oint \vec{E}\cdot d\vec{l}$ around the torus, with no attendant drop in plasma current. The governing equation is

$$V_L = I_I R + \frac{d}{dt}\left[L(I_I + I_R)\right] \tag{8.1}$$

where I_R and I_I are the RF and inductively driven components of the plasma current, R is the effective plasma resistance, and L is the inductance (internal plus external) of the plasma current distribution. (Equation 8.1 assumes that the RF driven current is carried by low-resistivity tail electrons.) The Versator experiments observed current increases. These early experiments also observed that lower hybrid current drive failed to work at high densities -- whence the concept of a density limit. These experiments (both around 0.8 GHz) showed density limits around $6 \times 10^{12}\,\mathrm{cm}^{-3}$ line-average density.

Subsequently lower hybrid current drive experiments were performed on a number of major tokamak experiments, most notably the Princeton Large Torus (PLT) at Princeton and Alcator C at MIT. Numerous experiments have shown that plasma current can be sustained solely with RF, and, indeed, some impressive steady state results have been obtained: Bernabei et al [Bernabei.82] document the sustainment of 165 kA of plasma current for 3.5 s on PLT; the time limitation was due to heating of a ferrite isolator in the RF transmission system. Experiments on FT (Frascati) at 2.45 GHz [Alladio.82] and Alcator C at 4.6 GHz [Porkolab.84-a] succeeded in driving 'flat-top' currents at $4\times 10^{13}\text{cm}^{-3}$ (line-average) and $1\times 10^{14}\text{cm}^{-3}$ respectively, suggesting that the current drive density limit scales with frequency. This has now been conclusively shown on Versator II [Mayberry.85], where a new 2.45 GHz experiment has yet to find a density limit. (The 0.8 GHz system had a density limit of $6\times 10^{12}\text{cm}^{-3}$ line-average [Luckhardt.82]; the new system has demonstrated current drive at $2.5\times 10^{13}\text{cm}^{-3}$ -- the experiment is limited by available power and the operating regime of the tokamak).

Aside from sustainment of the plasma current, lower hybrid current drive has demonstrated the capability for both starting up the plasma in the absence of inductive drive, and for ramping up the plasma current. PLT in 1983 demonstrated the formation of 100 kA plasmas with RF drive alone [Motley.84, Jobes.84] -- opening up the possibility of building a tokamak with no inductive drive, a substantial saving in engineering. Both Alcator C [Takase.85-b] and PLT [Jobes.85] have demonstrated the ability to significantly increase the plasma current with RF drive; on Alcator C the magnetic energy content of a 100 kA plasma was doubled in 0.3 s. The "ramp-up" efficiencies of both experiments (ie the efficiency with which delivered RF power is converted to stored magnetic energy) are in excellent agreement with theory [Karney.84].

A suitable review of lower hybrid experiments can be found in [Porkolab.84-b].

Despite the progress and successes in the field, both experimental and theoretical, much remains to be learnt. Between wave launching and wave absorption, a number of processes come into play. The waves propagate in an inhomogeneous medium undergoing refraction and bounces; the effects on different waves (at different initial spatial locations and having different wavevectors) can be quite varied. Toroidal effects are responsible for changes in the spectrum of the waves. Waves are scattered by density fluctuations, causing spectral broadening. Mode conversion and wave absorption are also present. Thus wave propagation is a complicated process, and not very well understood. While theories exist for various facets of the problem, experimental data on lower hybrid wave propagation in contemporary devices is meager.

Current drive experiments are predominantly analyzed from global measurements (current, loop voltage); more detailed and specific diagnostics are necessary to improve the understanding of lower hybrid wave physics. Spatially resolved X-ray measurements provide some insight into 'where is the power going ?', as do density and temperature profile measurements, RF probes and a few other diagnostics. Nonetheless the diagnostic of choice for studying wave propagation is without doubt coherent scattering of electromagnetic waves. A scattering diagnostic can look for the waves in the plasma directly, and measure their strength, spatial distribution and both frequency and wavenumber spectra.

Coherent scattering diagnostics have been used to detect and study lower hybrid waves on other tokamaks, such as Alcator A [Slusher.82], Alcator C [Watterson.85, Takase.85-a] and WEGA [Ichtchenko.83], as well as previously on Versator II [Richards.81]. The Alcator results are perhaps the most complete to date; Watterson et al have used a CO_2 laser scattering system to measure power, $N_{\parallel}$ spectra and radial profiles, and have also studied the parametric decay of the lower hybrid waves and ion cyclotron sidebands. The WEGA experiment operated at 136 GHz, using a fixed geometry inside the vacuum chamber. The present experiment is an upgrade of Richards' previous experiment on Versator (used primarily to study low frequency drift wave turbulence). It is a 139 GHz microwave experiment and offers more geometric flexibility than the other published experiments. Portions of this work have been previously published [Rohatgi.85a].

Our microwave scattering experiment uses a 7 W Extended Interaction Oscillator to generate power at 139 GHz. Waveguides are used to transmit the power to the tokamak, where a narrow beam is launched into the plasma. Electrons oscillate in this radiation field; some power is scattered. An electron density wave acts like a diffraction grating, causing coherent scattering in directions satisfying the Bragg condition $\vec{k}_S = \vec{k}_I \pm \vec{k}_W$, where $\vec{k}_I$ and $\vec{k}_S$ are the wavevectors of the incident and scattered radiation, and $\vec{k}_W$ is the wavevector of the electron density wave responsible for the scattering (see Fig 8.1). The scattered radiation is also shifted in frequency by the frequency of the electron density wave. The scattered radiation is received by a suitably positioned antenna, and mixed down to the intermediate frequency (IF) in a standard homodyne detection scheme. The IF signal is detected using a spectrum analyzer. A distinguishing feature of this experiment is the use of movable mirrors on both the transmitting (for the

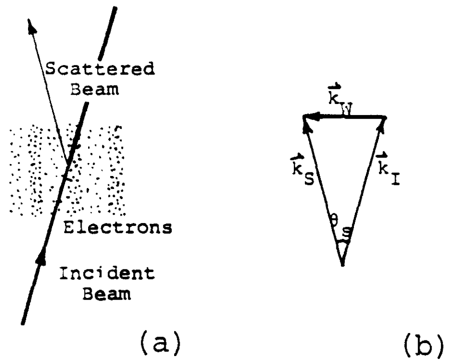

Fig 8.1 SCATTERING WAVEVECTORS

(a) shows an incident beam impinging on an electron plasma. The wave in the electrons results in a scattered beam. (b) The relation between the wavevectors of the incident beam ($\vec{k}_I$), the scattered beam ($\vec{k}_S$) and the electron density wave ($\vec{k}_W$) is shown, as is the scattering angle θ_S. [Note that a wave with $\vec{k}_W$ and frequency ω is identical to one with $-\vec{k}_W$ and $-\omega$; consequently scattered power may exist with $\vec{k}_S=\vec{k}_I-\vec{k}_W$ too.]

incident beam) and receiving antennae, which affords us a fair amount of flexibility in selecting scattering volumes. (Scattering volumes are defined by the overlap of the radiation patterns of the transmitting and receiving antennae.)

Before discussing the experiments we have performed, it is necessary to say a few words about the system used on Versator II to launch lower hybrid waves. The antenna used consists of 4 adjacent open-mouthed waveguides with independent phase controls. The waveguides are suitably phased in order to produce an electric field pattern at the face of the antenna that couples to slow (phase velocity less than the speed of light) lower hybrid waves in the plasma. The launched power typically has a broad spectrum in $\vec{k}$-space. The waves are characterized by the component of the wavevector parallel to the magnetic field, $k_{\|}$, or equivalently the parallel refractive index $N_{\|} = c\, k_{\|} / \omega$; either of these quantities is conserved to zeroth order during wave propagation. ($N_{\|}$ is conserved exactly if the magnetic field is purely toroidal, by toroidal symmetry, or in a cylindrical geometry because of axial and azimuthal symmetry. In a tokamak, $N_{\|}$ has a poloidal component which is not conserved; the consequent change in $N_{\|}$ during wave propagation affects the interaction between waves and plasma.)

With this setup we have sought to address the question of propagation of externally launched 0.8 GHz waves in Versator plasmas during current drive. Specifically we have measured the dependence of lower hybrid wave power on both radius and $N_{\parallel}$ (as well as on several other quantities.) Our results indicate the presence of a spatially defined resonance cone near the edge of the plasma, with very directional power flow that is in excellent agreement with theoretical modelling. The $N_{\parallel}$ spectrum for the +90° waveguide phasing is in good agreement with the computed spectrum. Power is seen to reach the center of the plasma. A special experiment has been conducted to look for wave absorption during current drive; evidence of absorption is seen. The measured frequency spectrum of the lower hybrid waves is consistent with theory. Some data has been taken at densities above the current drive density limit; no dramatic difference is seen.

The outline of this thesis is as follows. The experimental setup and procedure are described in Sections 9 and 10. (A single set of numbers is used serially to denote the various sections into which this thesis is divided; this introduction is already Section 8.) Section 11 covers the data analysis. The experimental results are presented in Section 12. Theoretical modelling was performed to compare with the experimental results; the modelling and comparison with experiment are presented in Sections 13 and 14 respectively. Section 15 is the conclusion. Several appendices follow the references (Section 16); these cover aspects of the calculation, microwave calibration measurements, hardware details, and computer programs, and are numbered as Appendices 17 through 21. The appendices are suitably referenced from the main text.

Section [8A] LOWER HYBRID WAVES

This section provides a background on lower hybrid waves. Lower hybrid waves are one of many normal modes of a magnetized plasma. The name is applied to waves in the frequency range just above the lower hybrid resonant frequency $\omega_{LH}^{-2}=\omega_{pi}^{-2}+(\omega_{ce}\omega_{ci})^{-1}$. (We are assuming the typical scaling for tokamak plasmas, $\omega_{ci}<<\omega_{pi}<<\omega_{pe}\sim\omega_{ce}$). The cold plasma dispersion relation in this frequency range has two branches, one being a slow wave characterized by refractive index N>>1 and the other a 'fast' wave with smaller N. The term lower hybrid wave is usually used to refer to the former. The name arises from the fact that the electrons are driven both by the electric field and the magnetic field.

$$m\,\frac{d\vec{v}_1}{dt} = q(\vec{E}_1 + \vec{v}_1 x \vec{B}_0) \qquad 8A.1$$

'Lower hybrid' refers to the mode where the driving terms have opposite sign, and is the lower frequency solution; the other mode is referred to as 'upper hybrid' and exists at frequencies above the electron plasma and cyclotron frequencies.

As a consequence of large N, the magnetic field perturbation associated with these waves is small ($cB_1<<E_1$), the magnetic energy content of the waves is small, and the electrostatic approximation may be used in the analysis. Electrostatic

analysis yields the standard Trivelpiece-Gould dispersion relation,

$$1 = \sum_j \left(\frac{\omega_{pj}^2 \cos^2\theta}{\omega^2} + \frac{\omega_{pj}^2 \sin^2\theta}{\omega^2 - \omega_{cj}^2} \right) \tag{8A.2}$$

where the summation j is over the species e (electron) and i (ion), and θ is the angle between the wavevector $\vec{k}$ and the magnetic field. Using the assumed scaling (above), this can be rewritten

$$\omega^2 = \frac{\omega_{pi}^2}{1 + (\omega_{pe}^2 \sin^2\theta/\omega_{ce}^2)} \left(1 + \frac{m_i}{m_e}\cos^2\theta\right) \tag{8A.3}$$

Notice that for $\cos^2\theta \sim 1$, $\omega \sim \omega_{pe}$. Since our interest is in waves with $\omega \ll \omega_{pe}$, we may use $\sin^2\theta \cong 1$ and $\cos^2\theta \cong (k_\parallel/k_\perp)^2 \ll 1$, whence

$$\omega^2 = \frac{\omega_{pi}^2}{1 + \omega_{pe}^2/\omega_{ce}^2} \left(1 + \frac{m_i}{m_e} \cdot \frac{k_\parallel^2}{k_\perp^2}\right) \tag{8A.4}$$

This is the standard electrostatic lower hybrid dispersion relation.

The size of electromagnetic corrections is approximately 10% in $k_\parallel$ or $k_\perp$; we do in fact use the electromagnetic dispersion relation in all our analysis -- this is discussed in Appendix 18. Nonetheless the electrostatic dispersion relation is reasonably accurate, easier to grasp, and may be used to illustrate two of the interesting characteristics of lower hybrid waves.

It is worthwhile to indicate the relative magnitudes of the quantities in Eqn 8A.4. Typically for our experiments, $\omega/2\pi=0.8$ GHz, $\omega_{pi}/2\pi\cong 0.5$ GHz, $\omega_{pe}/2\pi\cong 20$ GHz, $\omega_{ce}/2\pi\cong 35$ GHz, from which we see that the quantity in brackets must be approximately 4. Since $m_i/m_e=1836$, $k_\perp/k_\parallel=25$, and the wavevector is indeed nearly perpendicular to the magnetic field.

The two interesting characteristics of lower hybrid waves mentioned above are (1) propagation in resonance cones and (2) the fact that the group velocity of these waves is nearly perpendicular to the wavevector. Both of these are a consequence of the fact that, at least in the electrostatic approximation, the dispersion relation is independent of the magnitude of the wavevector k. If the components of $\vec{k}$ are (k,θ_k,ϕ_k) in spherical polar coordinates (with the magnetic field as axis), then $\omega=\omega(\theta_k)$ and

$$\vec{k}\cdot\vec{v}_g = \vec{k}\cdot\frac{\partial\omega(\vec{k})}{\partial\vec{k}} = k\,\frac{\partial\omega(\theta_k)}{\partial k} = 0 \tag{8A.5}$$

We see that although lower hybrid waves have wavevectors nearly perpendicular to $\vec{B}$, the wave propagation is predominantly toroidal. It is easy to show that the toroidal components of $\vec{v}_g$ and $\vec{k}$ are in the same direction and that the poloidal components are opposite. This means that a wave propagating radially inwards has a $\vec{k}$ pointing radially outward.

To show resonance cone propagation, consider waves in the same plane (say with $k_y=0$). Then the ratio of the components of the group velocity

$$\frac{v_{g\parallel}}{v_{gx}} = \frac{\partial\omega/\partial k_{\parallel}}{\partial\omega/\partial k_x} = -\frac{k_x}{k_{\parallel}} \tag{8A.6}$$

which is determined by the dispersion relation and is the same for all waves, regardless of wavenumber. Thus waves with different wavenumbers (and in general different group velocities) follow the same trajectories. This is resonance cone propagation; we have already seen that the propagation is predominantly toroidal.

Further discussion of lower hybrid waves is contained elsewhere in this thesis. Lower hybrid waves were already briefly touched on in the Introduction (p.21). A discussion of how the waves are launched in the plasma may be found in Section [9.9]. The electromagnetic analysis and power transport are both covered in Appendix [18].

Section [9] EXPERIMENTAL SETUP

[9.1] Outline

This section contains a description of the experimental setup used for the detection of lower hybrid waves in the plasma. A general description of the microwave scattering system in [9.2] is followed by more detailed sub-sections ([9.3] - [9.8]). Some procedures are mentioned, where they relate more to the setting up of the experiment than to running the experiment. The Versator II tokamak and its operation have been adequately discussed elsewhere [Richards.78,81; Stone.79] and are not discussed here. Table 9.1.1 shows typical parameters of Versator II plasmas. Versator ports and diagnostics are shown in Fig 9.1.1. The lower hybrid system is discussed in sub-section [9.9]. Other diagnostics that bear on the present experiments are covered in [9.10].

Table 9.1.1 VERSATOR II PLASMA PARAMETERS

Quantity	Symbol	Value
Major Radius	R	40.5 cm
Minor Radius	a	13.0 cm
Toroidal Field	B_T	0.8 - 1.5 T
Plasma Current	I_P	20 - 60 kA
Electron Density	$\bar{n}_e$	2×10^{12} - 3×10^{13} cm^{-3}
Electron Temperature	T_e	200 - 500 eV
Ion Temperature	T_i	100 - 180 eV
Shot Duration		30 ms typ.

RF Systems:	(1)	(2)
Frequency	0.8 GHz	2.45 GHz
Max Power	100 kW	100 kW
Max Pulse Length	20 ms	40 ms

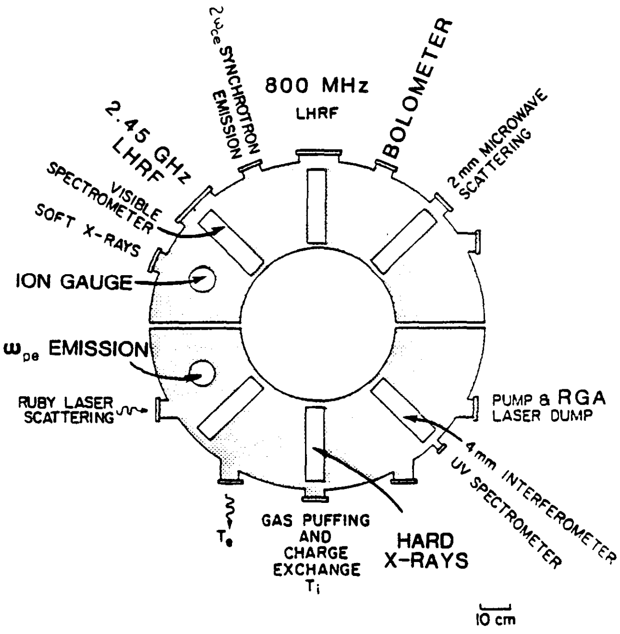

Fig 9.1.1 VERSATOR PORT ALLOCATION

Top view of Versator II showing the microwave scattering port, the lower hybrid (LH) RF ports, and other equipment and diagnostics. The microwave scattering port is 45° toroidally from the 0.8 GHz LHRF port.

[9.2] General Description

An experimental schematic is shown in Fig 9.2.1. Much of the equipment used for this experiment was inherited from previous microwave scattering experiments on the Versator II tokamak [Richards.81]. An extended interaction oscillator (EIO) made by Varian is used as a 7 W CW source at 139 GHz. Most of the power is transmitted through waveguide to the tokamak, where a horn and lens are used to launch a narrow (approx 4.5° FWHM) incident beam. The incident beam bounces off an adjustable mirror and into the vacuum vessel. The scattered beam is received by similar apparatus. The adjustable mirrors have two degrees of freedom: rotation in the poloidal plane and translation along the ports on which they are mounted. This system permits complete flexibility

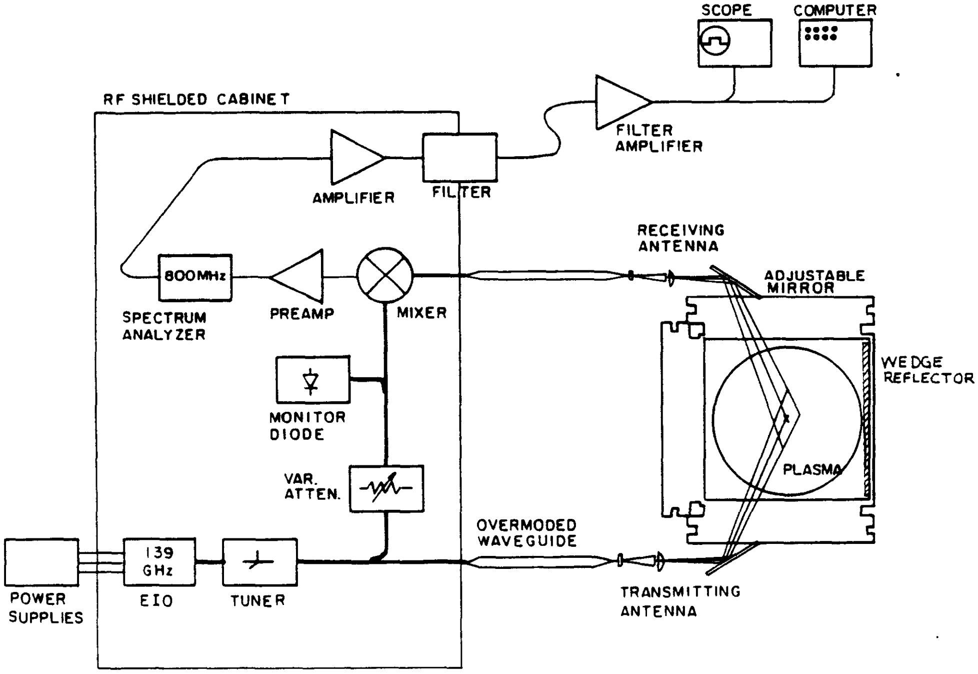

Fig 9.2.1 EXPERIMENTAL SCHEMATIC

in choosing scattering geometry (location of scattering volume, scattering angle, and poloidal orientation) limited only by port access. A wedge shaped reflector inside the vacuum vessel is used to deflect unwanted microwave power and reduce stray signal.

The power scattered by the 0.8 GHz lower hybrid waves is at 139±0.8 GHz. The received scattered power is transmitted by waveguide back to the main cabinet, where it is mixed with a local oscillator signal (taken by a 20 dB tap off the forward power line), to produce an IF signal at 0.8 GHz. (This is the standard homodyne detection method.) This IF signal is amplified, and then detected by a spectrum analyzer which is set to a fixed frequency (0.8 GHz) and used as a tuned detector. The purpose of the amplifier is to boost the signal power above the spectrum analyzer noise level. This receiver has a noise temperature of 6600 K, which corresponds to a sensitivity of about 3×10^{-14} W in a bandwidth of 300 kHz (this bandwidth is used for all experiments except frequencyspectrum measurements). The detected signal (output of the spectrum analyzer) is driven by an amplifier through microwave filters and a triax line over to the control room, where it is smoothed and then stored in our computer.

[9.3] EIO Source

The 139 GHz source used in this experiment is a Varian

VKT 2438 E1 Extended Interaction Oscillator. The EIO is a linear beam tube which offers a significant advantage over conventional millimeter wave sources (such as reflex klystrons) in that the beam power is not dissipated by the delicate RF structure within the tube. Consequently, sustained high power operation is feasible. Our model is a water-cooled tube rated at 20 W nominal, although it is used at a more modest level of 7 W in order to prolong the tube lifetime.

The EIO requires 3 power supplies for operation, as well as protection against high-voltage faults. A Hipotronics 10 kV 300 mA regulated power supply is used for the cathode supply; smaller supplies are used for the anode (typical operation at 5 kV, < 1 mA) and filament (typical 1 A at 6 V). The anode power supply is used to switch the tube on and off. The power circuit is shown in Fig 9.3.1. Also, Fig 9.3.2 shows the cooling system for the tube.

An important consideration is how to get the high voltage power into the RF shielded cabinet, since any wire going through a hole in the cabinet looks like a co-axial transmission line. What is needed is a microwave filter with 10 kV standoff. Our experiences with graphite- and iron-loaded compounds were not entirely satisfactory; eventually we designed and built multistage LC-type filters that worked very well. These are further described in

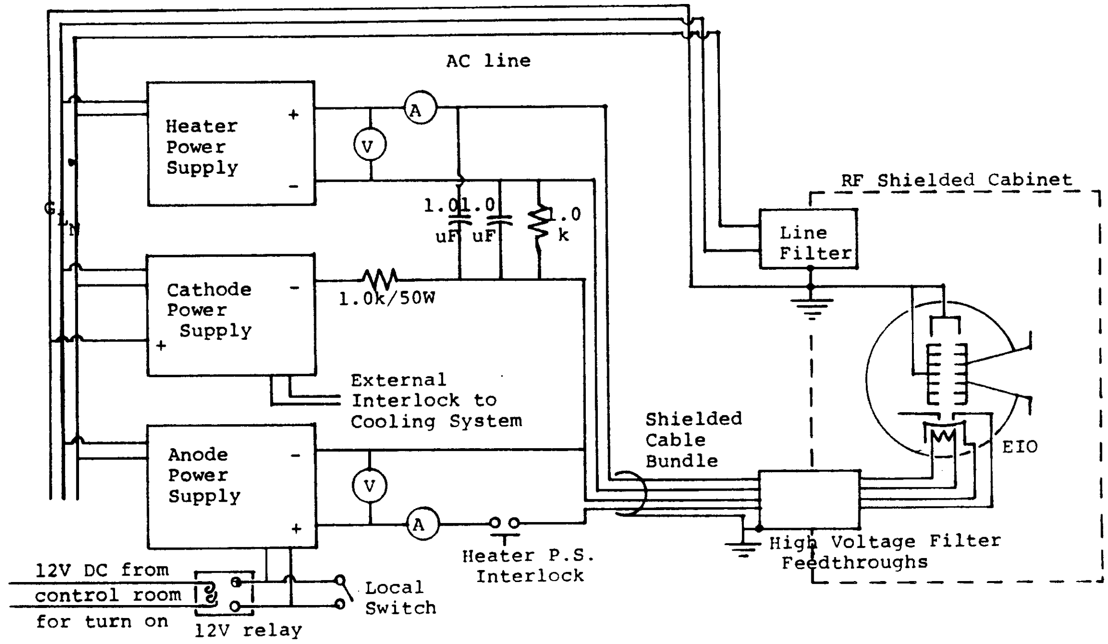

Fig 9.3.1 EIO POWER CIRCUIT

Note that the ground (= HV return) connection is through the line cord supplying AC power to the RF shielded cabinet.

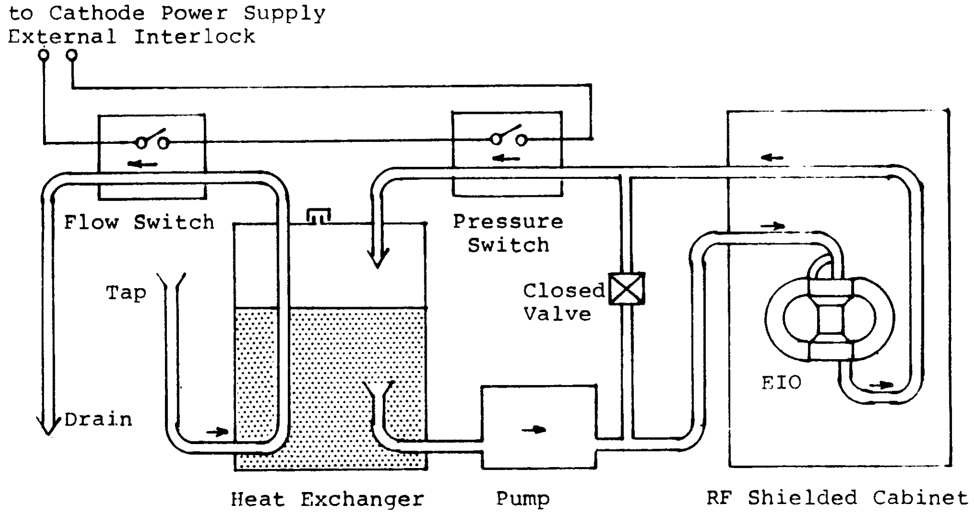

Fig 9.3.2 EIO COOLING SYSTEM

The two stage cooling system has a tap water primary and a distilled water secondary coupled through a heat exchanger.

Appendix [20].

By and large our EIO has served us well. A couple of times the tube gave some difficulty turning on; we found in such cases that running the tube for a couple of hours with low anode voltage (well below turn-on, typical beam current about 15-20 mA) was quite effective.

[9.4] Transmitting/Receiving Antennae

Gain standard horns with 25 dB gain are used. These are rectangular horns flared in both planes. As mentioned above the horns have focussing lenses mounted in front of them. Quartz lenses were chosen for availability and good microwave transmission properties. The refractive indices at 25 GHz [von Hippel.54] and at optical frequencies [CRC.79] were used to estimate a desirable (optical) focal length. (Suitable information at 140 GHz was not available.) The gain patterns of the horn + lens combination have been measured; this measurement is further described in Appendix [19.3].

The adjustable mirrors used to reflect the incident and scattered beams are simple aluminum mirrors on plexiglass assemblies. One is shown in Fig 9.4.1. A protractor scale on the assembly permits the mirror angle to be set to 0.5°; the position is held by friction at the pivot. The mirror assemblies bolt onto a plexiglass track (which has threaded

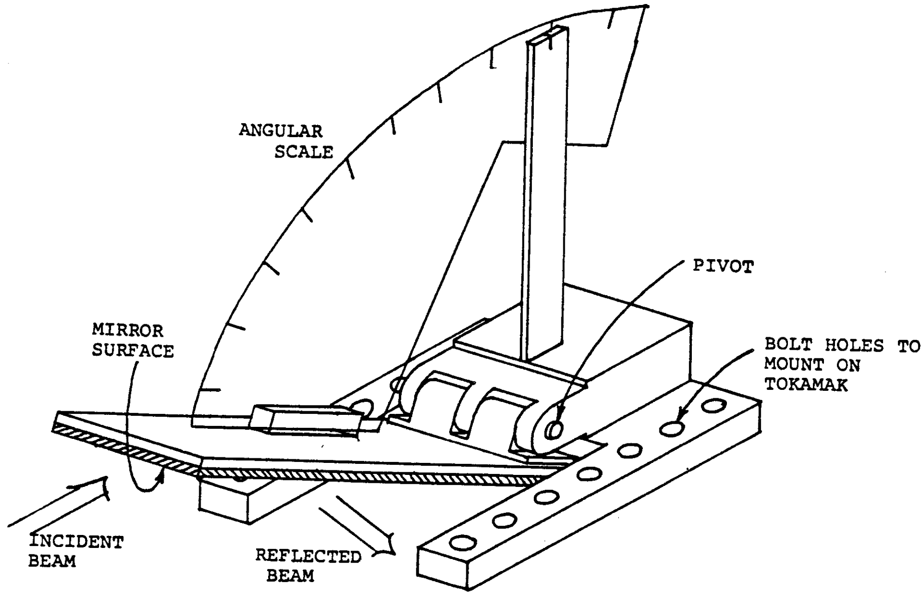

Fig 9.4.1 MIRROR ASSEMBLY

Mirror surface is aluminum; all other parts are plexiglass.

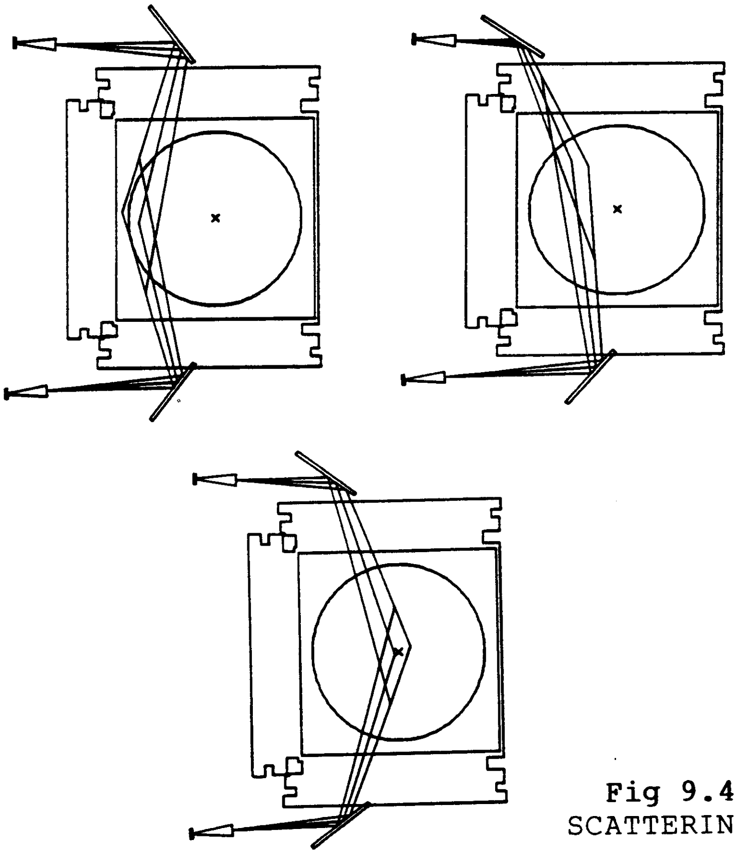

Fig 9.4.2 SAMPLE SCATTERING GEOMETRIES

holes) that is mounted on the tokamak port. The position may be set to 0.5".

The overlap of the incident and scattered beam patterns (which are reflected by the mirrors) defines the scattering volume, ie the volume from which electron density waves are detected. Some of the scattering volumes possible with this setup are shown in Fig 9.4.2. As is evident, the scattering volumes are not small; spatial resolution is a problem with this experiment. Typical scattering volumes are diamond shaped, with the long diagonal vertical and ~10 cm long; the short diagonal is typically ~5 cm. (Of course, the exact sizes vary from one scattering volume to another.) The scattering volume dimensions are comparable to the plasma scale lengths, consequently the plasma parameters may vary somewhat over the plasma volume (especially near the edge). Because of the spread in density across the scattering volume, a given scattering angle also corresponds to a spread in values of parallel refractive index ($N_{\parallel}$). Nonetheless the scattering volumes are still somewhat smaller than the plasma cross-section, and meaningful comparisons between different regions of the plasma and different scattering angles may be made. Values quoted for scattering parameters in this thesis always refer to the values computed at the nominal center of the scattering volume; the nominal center is the point of intersection of the central rays of the incident and scattered beams.

The entire geometry is aligned using a CW beam, by adjusting the horn and mirror positions until maximum power is received at the end of the receiving waveguide (Appendix [19.4]). The receiving waveguide is attached to the machine by a 2-D sliding dovetail bracket (Fig 9.4.3) to facilitate this adjustment. Waveguide transmission losses for this system are approximately 5 dB: in addition to waveguide copper losses, there are losses at waveguide flanges and losses associated with transitions to and from the overmoded waveguide.

Fig 9.4.3 SLIDING DOVETAIL BRACKET

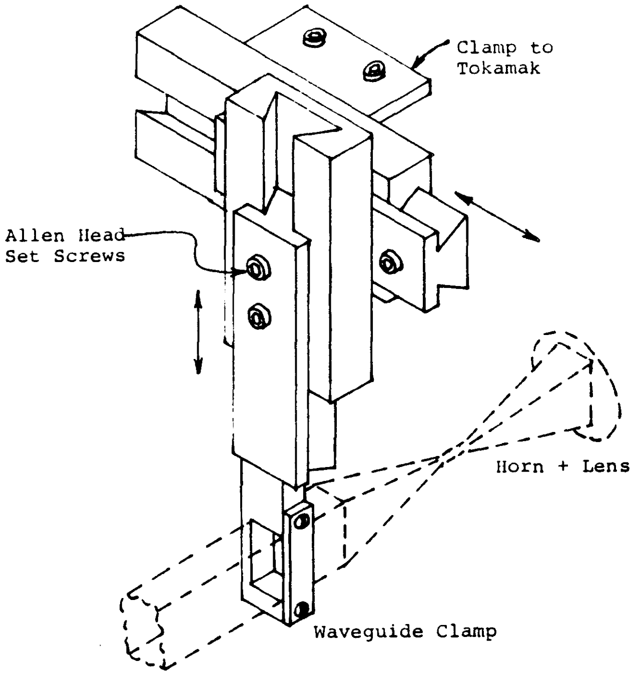

[9.5] Wedge Reflector

A wedge reflector, shown in Fig 9.5.1, is installed in the vacuum vessel in order to minimize problems associated with stray multiply reflected signal getting into the receiver. The idea is that a multiply reflected beam will impinge once on the wedge (located on the inside wall) and be deflected toroidally away from the scattering port. A salient feature of the design is the absence of electrical contact between various pieces and the vacuum vessel. This was necessary to eliminate eddy currents and associated forces that ruined two previous assemblies.

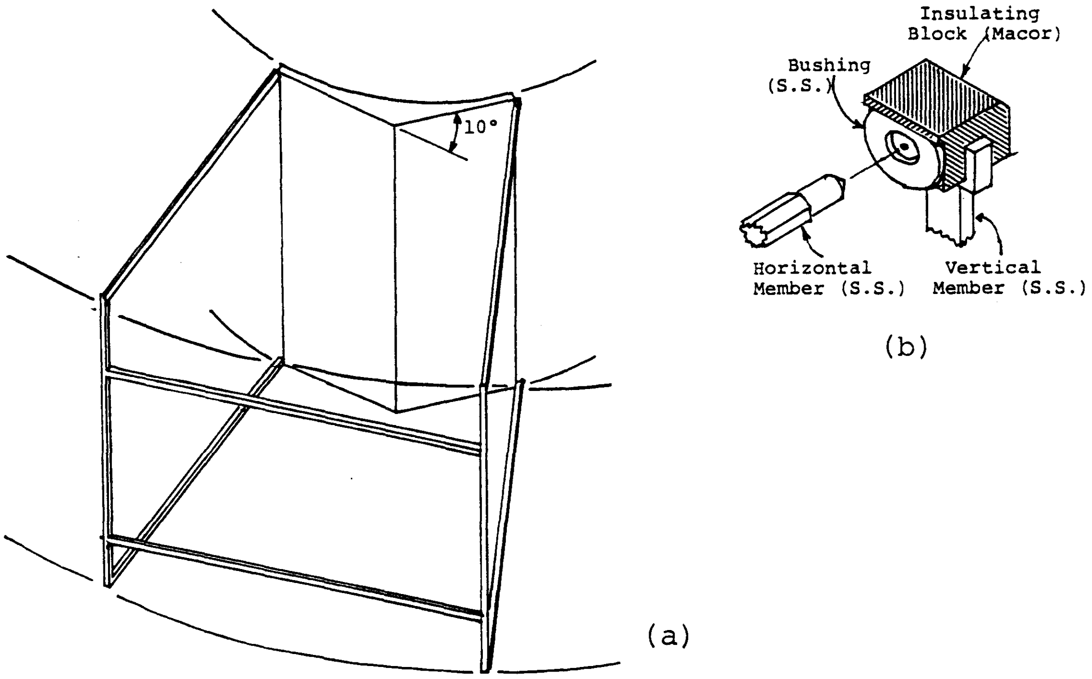

Fig 9.5.1 WEDGE REFLECTOR

(a) shows wedge reflector and frame as assembled inside the tokamak. (b) shows corner detail.

[9.6] Microwave Receiver

The microwave receiver comprises a mixer, a pre-amplifier and a spectrum analyzer and is shown in Fig 9.6.1. The mixer is an Alpha/TRG model F9100. Local oscillator drive at the 3 mW level is provided by a 20 dB tap off the forward power line, adjusted with a variable attenuator. A crystal diode is used to monitor the L.O. drive level; this also serves as a convenient power monitor. The mixer IF output at 0.8 GHz is fed directly into a broadband (10-1000 MHz) low-noise MITEQ pre-amplifier with a 35 dB nominal gain. This boosts the signal above the spectrum analyzer noise level. The spectrum analyzer (Tektronix 7L12) is used as a fixed frequency detector, with usually 300 kHz bandwidth. Owing to the wide dynamic variation of the scattered signal, the 10 dB/div log scale on the spectrum analyzer is used. Care is taken to protect the spectrum analyzer with a DC block and a DC short on the RF input. Calibrations of the mixer and preamplifier are covered in Appendices [19.2] and [19.5] respectively.

It is worth pointing out that the receiver is sensitive to suitably polarized radiation at 139 ± 0.8 GHz, and aside from scattered power there is also some background emission from the plasma. Thus the detected signal has three components: noise, plasma emission, and scattered signal. In practice it is the plasma emission and not the noise which usually limits the detection sensitivity. The plasma emission is

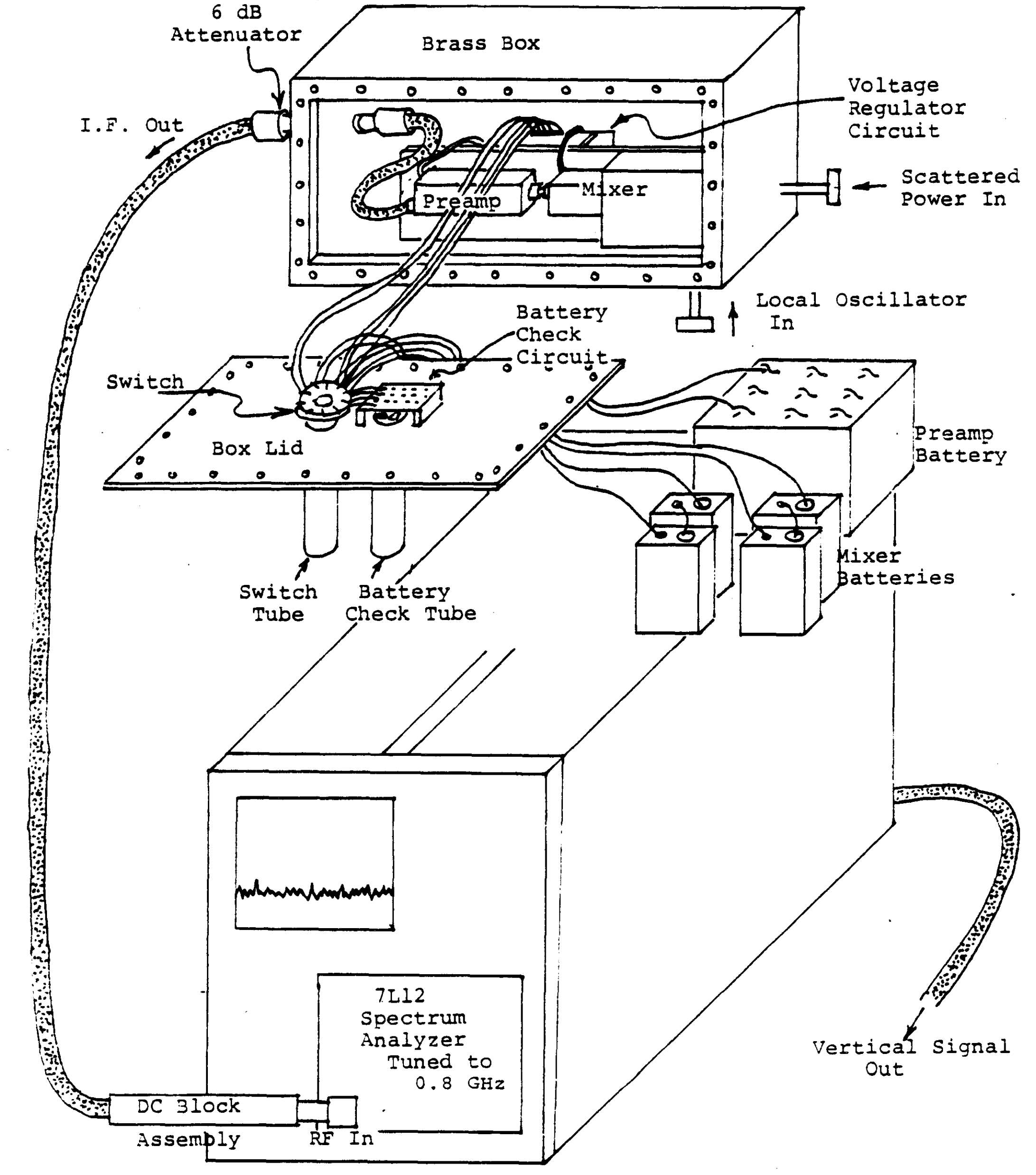

Fig 9.6.1 MICROWAVE RECEIVER (disassembled view)

thought to be 4-5th harmonic cyclotron emission from tail (ie energetic) electrons.

[9.7] Shielding

Excellent shielding is necessary for this experiment because we are trying to measure extremely weak ($\tilde{}10^{-13}$W) signals at the same time as we are pumping ~50 kW of power at <u>the same frequency</u> into the plasma. Shielding also serves to isolate the apparatus from the substantial electromagnetic noise associated with a tokamak discharge.

The entire microwave system is housed in a RF-tight cabinet, with finger-stock along the door joints, absorber strips along the door frame, a double layer of aluminum foil along the hinge, and sheets of microwave absorbing foam on the inside. Power lines going in and signal lines coming out are all filtered. This box is good for about 60+ dB isolation. The most sensitive components, namely the mixer and preamp, are housed along with their batteries in a second shielded box within the first. This small brass box (Fig 9.6.1) has a 32-screw lid, and 3 ports. Two tubular holes are for turning the devices on/off and for a battery-status LED indicator. These are 'safe' because the tubes are cut-off at 0.8 GHz. The third port is for the output signal. Unfortunately the preamp output is at the same frequency that we are trying to shield against, and cannot be filtered. Instead there is a 6 dB attenuator on this port.

Since the preamp output noise level is still higher than the spectrum analyzer noise level, this attenuator does not adversely affect the signal to noise ratio or the sensitivity. The shielding described above is adequate to provide a clean signal, free from pickup.

[9.8] Electronics

The detected scattered power signal from the spectrum analyzer goes through a simple amplifier, shown in Fig 9.8.1, whose purpose is to provide a low impedance signal to drive a microwave filter and 75' triax cable, and also to isolate the control room and shielded cabinet grounds. The amplifier is grounded at the control room through the middle triax conductor. The triax outer shield is grounded at the shielded cabinet. In the control room the signal goes

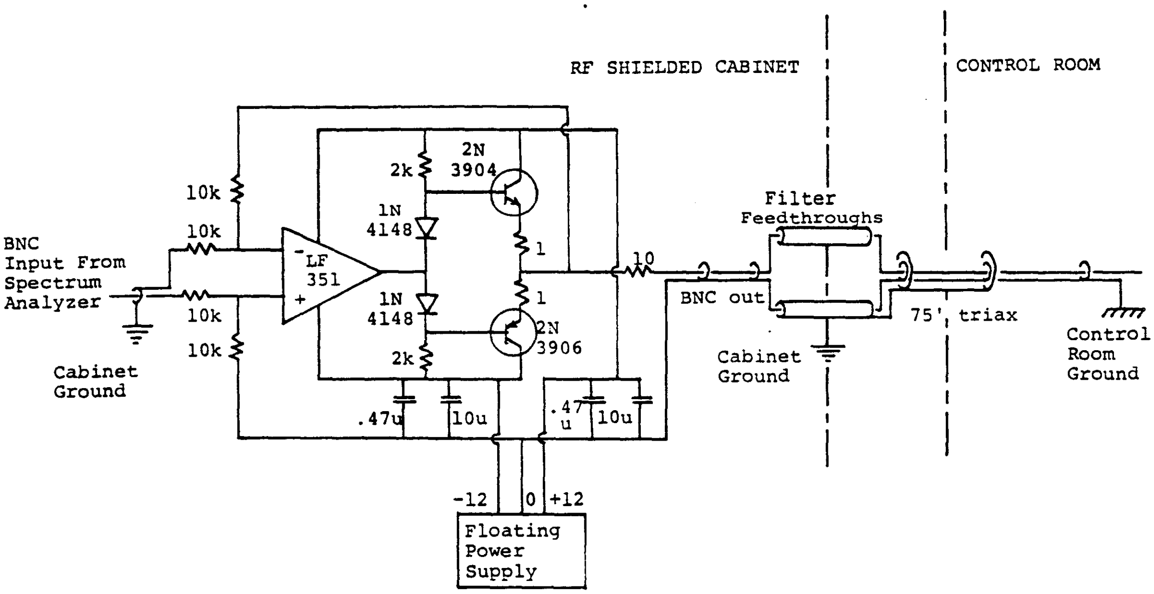

Fig 9.8.1 SIGNAL AMPLIFIER AND TRANSMISSION LINE

through a boxcar integrator set up as a simple low-pass filter with a 0.1 ms time constant, typically. The smoothed signal is displayed on a scope and also goes into our computer via a 12.8 kHz 10-bit digitizer. The boxcar integrator also compensates the DC offset of the spectrum analyzer and amplifier so as to make efficient use of the digitizer's ±5 Volt input range. The electronics is calibrated from the spectrum analyzer through to the computer, 4.60 dB/Volt.

[9.9] Lower Hybrid System

A single 150 kW Varian klystron is used to power the 0.8 GHz lower hybrid RF system on Versator. An array of 4 adjacent fundamental mode waveguides, commonly called a 4 waveguide grill, is used as an antenna. The waveguides are fed through power splitters with independent phase controls for each line.

Fig 9.9.1 shows the antenna, together with the waves in the 4 waveguides for the case of +90° relative waveguide phasing (waveguide 2 is 90° in phase ahead of waveguide 1, and so on). The field pattern at the face of the antenna is shown for 4 successive time points a quarter period apart; it is seen that the field pattern appears to move across the face of the antenna from right to left. In this way, the phased array of waveguides is able to couple power to slow waves (phase velocity less than the speed of light) travelling

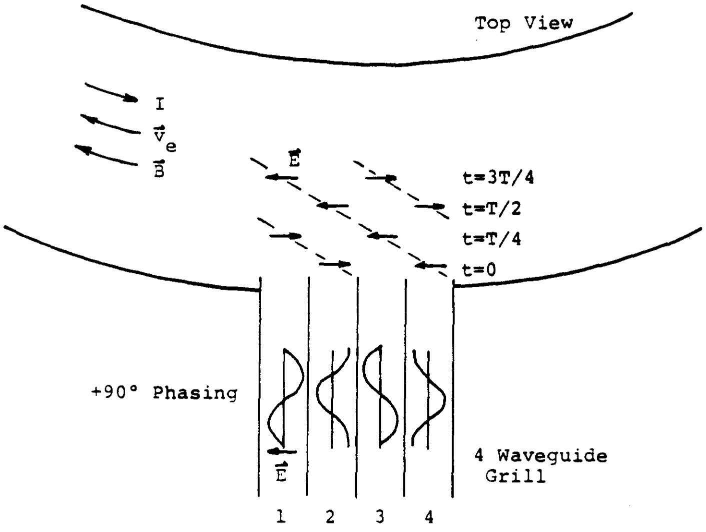

Fig 9.9.1 LAUNCHING LOWER HYBRID WAVES

A top view of the tokamak and the lower hybrid launching antenna is shown. The waves in each waveguide are shown for the case of +90° relative waveguide phasing. The field pattern at the antenna face is shown at quarter period (T/4) intervals. Also shown are the directions of the plasma current $\vec{I}$, the electron drift $\vec{v}_e$ and the toroidal magnetic field $\vec{B}$.

preferentially in the electron drift direction. The toroidal component of the wavevector of the launched waves is to some extent determined by the wavenumber of the field pattern moving across the antenna face, but in practice a broad spectrum of waves is launched. (In fact for the case shown, 30% of the power is coupled to waves travelling from

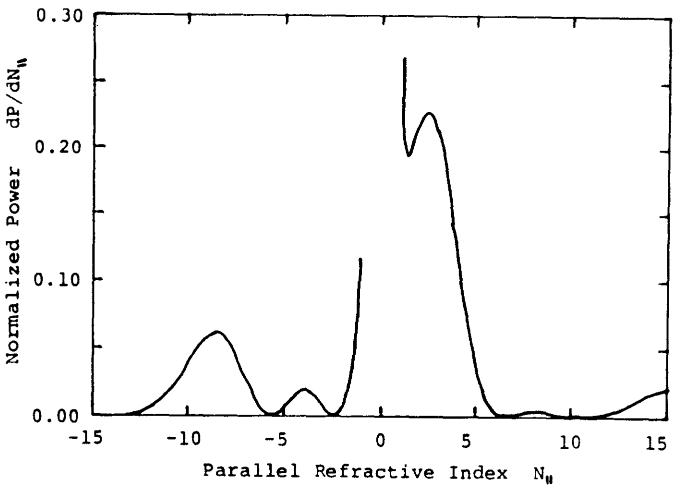

Fig 9.9.2 LAUNCHED SPECTRUM FOR +90° PHASING

This spectrum is computed as described in Section [13.2].

left to right. The computed spectrum of waves launched may be seen in Fig 9.9.2.) The +90° phasing, because it launches waves preferentially in the electron drift direction, is associated with current drive; the -90° phasing is not. (The 180° phasing, with a symmetric wave spectrum and higher wavenumbers is associated with electron heating.) It is conventional to speak in terms of the wave refractive index $\vec{N} = c\,\vec{k} / \omega$, where $\vec{k}$ and ω are the wavenumber and (angular) frequency of the lower hybrid wave. The subscripts $_\parallel$ and $_\perp$ (as in $N_\parallel$ or $\vec{k}_\perp$) are used to denote the components parallel and perpendicular to the (predominantly toroidal) magnetic field.

[9.10] Other Diagnostics

The primary (utility) diagnostics are the plasma current, loop voltage, density interferometer and in/out position monitor. In addition, the second harmonic cyclotron emission ($2\omega_{ce}$) diagnostic provides valuable information on plasma emission.

The plasma current is measured by a Rogowski coil encircling the plasma cross-section as shown in Fig 9.10.1. The voltage across this coil is proportional to the time derivative of the encircled current; the signal is integrated to yield the plasma current. Figure 9.10.1 also shows the toroidal loops used to measure the loop voltage (the 4 loops at the corners of the vacuum vessel cross-section are in series).

Fig 9.10.1 PLASMA CURRENT AND LOOP VOLTAGE COIL WINDINGS

The return conductor of the Rogowski coil is fed back through the middle of the coil.

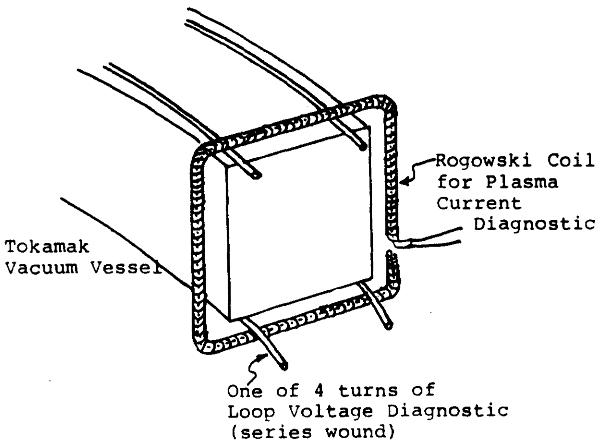

The density is measured by a 80 GHz interferometer. An O mode beam is launched from the bottom of the machine; the transmitted beam is received at the top. The phase shift of the transmitted beam is measured modulo 2π at a 100 kHz sampling rate. This phase shift is proportional to the electron density averaged over the line of propagation. The calibration constant for our instrument is $2.26 \times 10^{12} cm^{-3}$ (line average) per 2π phase shift. (A phase shift of 2π is commonly known as a fringe.)

The in/out position monitor consists of two sets of coils, each oriented to measure the poloidal magnetic field, one on the inside of the machine and one on the outside. The difference of the two signals upon integration yields a signal proportional to the displacement of the plasma current column from the geometric center.

Our second harmonic cyclotron emission ($2\omega_{ce}$) detector consists of a horn antenna feeding a 71 GHz heterodyne receiver [McDermott.84]. This radiation comes primarily from electrons with substantial perpendicular energies, and provides information on tail electrons. Its usefulness for the microwave scattering experiments stems from the fact that the $2\omega_{ce}$ signal correlates quite well with the plasma emission seen by the receiver of the scattering system, thus providing an indirect monitor of the 139 GHz plasma emission.

Section [10] EXPERIMENTAL PROCEDURE

- -

[10.1] Outline

[10.2] Setting Up Equipment

Three systems are required to be operational for this experiment -- the tokamak, the 0.8 GHz RF System, and the 139 GHz scattering system; all require some setting up.

Setting up the tokamak involves (1) keeping the machine clean between runs (2) turning on various power supplies and diagnostics immediately before a run and (3) tuning the machine during a run. Two strategies are in use on Versator for keeping the machine clean: discharge cleaning and titanium gettering. The latter introduces changing plasma and wall conditions on a 1 - 2 hour timescale, and requires continual retuning in order to maintain plasma conditions. In particular, gradual increase of the ohmic heating drive is necessary during a run. With discharge cleaning prior to a run, on the other hand, we were able to maintain consistent quality shots for several hours with minimal retuning and no increase in the ohmic heating drive. We naturally preferred to rely on discharge cleaning (4 second discharge out of a 12 second cycle; the pump-out time is approximately 3 seconds) to keep the machine clean. It is also necessary to monitor the vacuum system's liquid nitrogen cold trap, to prevent backstreaming of water, hydrocarbons and other impurities if and when the cold trap runs dry.

A number of power supplies and diagnostics need to be turned on prior to a run. These include power supplies for the main field, the vertical field, the ohmic heating system, the breakdown oscillator, the filament, the sequencer, the interlock and control system, and the water cooling system. Utility diagnostics include a 80 GHz (4 mm) interferometer, a second harmonic cyclotron emission ($2\omega_{ce}$) detector, a hard X-ray crystal detector, plus various wire loops for monitoring currents, plasma position, and plasma loop voltage. It is standard practice to test fire the various magnetic field systems before a run. The computer must also be set up for data acquisition.

Tuning the machine in order to get suitable plasmas may take from one to several hours. (Versator runs one shot every 120 seconds, typically.) The main tuning knobs are the vertical field system controls and the gas puffer controls. Some features of good shots are density and current flat-tops, centered position, reproducibility, low level of $2\omega_{ce}$

emission (more on this later), low level of hard X-rays, and absence of disruptions. Attaining such shots is an art, often difficult.

The RF system requires periodic waveguide conditioning, preferably, but not necessarily, before each run. The purpose of this is to clean the waveguide walls and improve the waveguides' power handling capability. This is done by sending short pulses of power (typically 1 ms every second) through the system into vacuum, increasing the power levels to keep up with what the waveguides will handle. The gas pressure and waveguide reflected powers are monitored in order to watch for plasma breakdowns in the waveguide. 0° relative phasing between waveguides is used for conditioning because it couples well to vacuum. Other than conditioning, setting up the RF system requires going through a turn-on and warm-up procedure, and setting the waveguide phasing appropriately (usually +90° for current-drive experiments). It is also necessary to have the radial position of the 4-waveguide grill suitably adjusted for good coupling of power to the plasma. In practice this position is not too critical, and once set needs no adjustment.

Setting up the scattering system is straightforward. The EIO power supplies are turned on slowly and the EIO power is checked. The electronics and spectrum analyzer are turned on; the spectrum analyzer is locked to an 0.8 GHz signal taken from the RF system. Mixer and preamplifier are turned on; their batteries are replaced if necessary.

[10.3] Planning Datapoints

An experiment may be thought of as measurement of scattered power over a set of datapoints, where a datapoint is specified by (1) the plasma conditions, especially the magnetic field and density (2) the RF system parameters, namely the RF power and the waveguide phasing, and (3) the parameters characterizing the detected wave, namely parallel wavenumber $N_{\parallel}$, perpendicular orientation and the spatial location. In one experiment usually only one of these parameters is varied. The plasma conditions and RF system parameters are chosen and may be set more or less directly, but the situation regarding the specification of the scattered wave is more complicated. We prefer to specify waves in terms of $N_{\parallel}$, both because to 0th order $N_{\parallel}$ is conserved during propagation and also because this is the variable in which computed spectra [Brambilla.76] are expressed. However, the scattering angle is related to $N_{\parallel}$, so that a given $N_{\parallel}$ will correspond to different scattering angles at different locations in the plasma. The second complication is needing to back-calculate the mirror positions necessary for a chosen spatial location of the scattering volume. For these reasons a computer program (described more fully in Appendix [21]) is used determine the mirror positions for a given $N_{\parallel}$ and spatial location.

The program uses the cold plasma electromagnetic dispersion relation to determine the scattering angle, and then does the coordinate geometry calculation to determine the mirror positions. The program also draws a sketch of the scattering geometry and computes some quantities required for data analysis. In this manner the mirror positions for each desired datapoint are determined at the beginning of a run. Of course, some experiments (frequency scan, power scan, comparison of waveguide phasings) require only a single scattering geometry.

[10.4] Running the Experiment

Once things are set up and the machine is tuned, data collection may begin. The tokamak is run on a continuous cycle, typically 120 seconds, except for breaks. The usual cause of breaks is needing to change the mirror positions for a new datapoint; this takes about 5 minutes. Some datapoint changes do not require changing mirror positions (such as changing the spectrum analyzer frequency or the waveguide phasing) and may be accomplished between shots without disrupting the cycle; where possible this is preferable, as breaks affect shot reproducibility. After a 5 minute break, it typically takes 1 or 2 shots to return to normal. Other causes of breaks are less predictable -- a fault of some sort, a need to check something, or a break required by some other concurrent experiment -- but by no means infrequent.

Most shots taken are for data, ie with the aim of measuring scattered power. These shots are judged good or bad immediately; good shots are used for analysis, bad ones are ignored. Shots may be judged bad for a variety of reasons:

(1) wrong density

(2) poor plasma position

(3) misfire of some system

(4) high $2\omega_{ce}$ emission

The last merits some elaboration. As mentioned in section [9.6], the scattering system detects plasma emission in addition to scattered signal. This background plasma emission may be seen independently of scattered signal by blocking off the incident scattering beam. The emission correlates well with the $2\omega_{ce}$ emission and is thought to be 4-5th harmonic cyclotron emission from tail electrons. Since the scattered signal sensitivity is limited by the plasma emission, high emission may make the scattered power measurement meaningless, especially if the emission jumps up when the RF turns on. Fortunately it is generally possible to run with emission levels low compared to scattered signal levels. Unfortunately, large tail populations and high emission levels are good for current drive and lower-hybrid wave absorption, so that our measurements are limited to regimes where current-drive effects are not at their strongest.

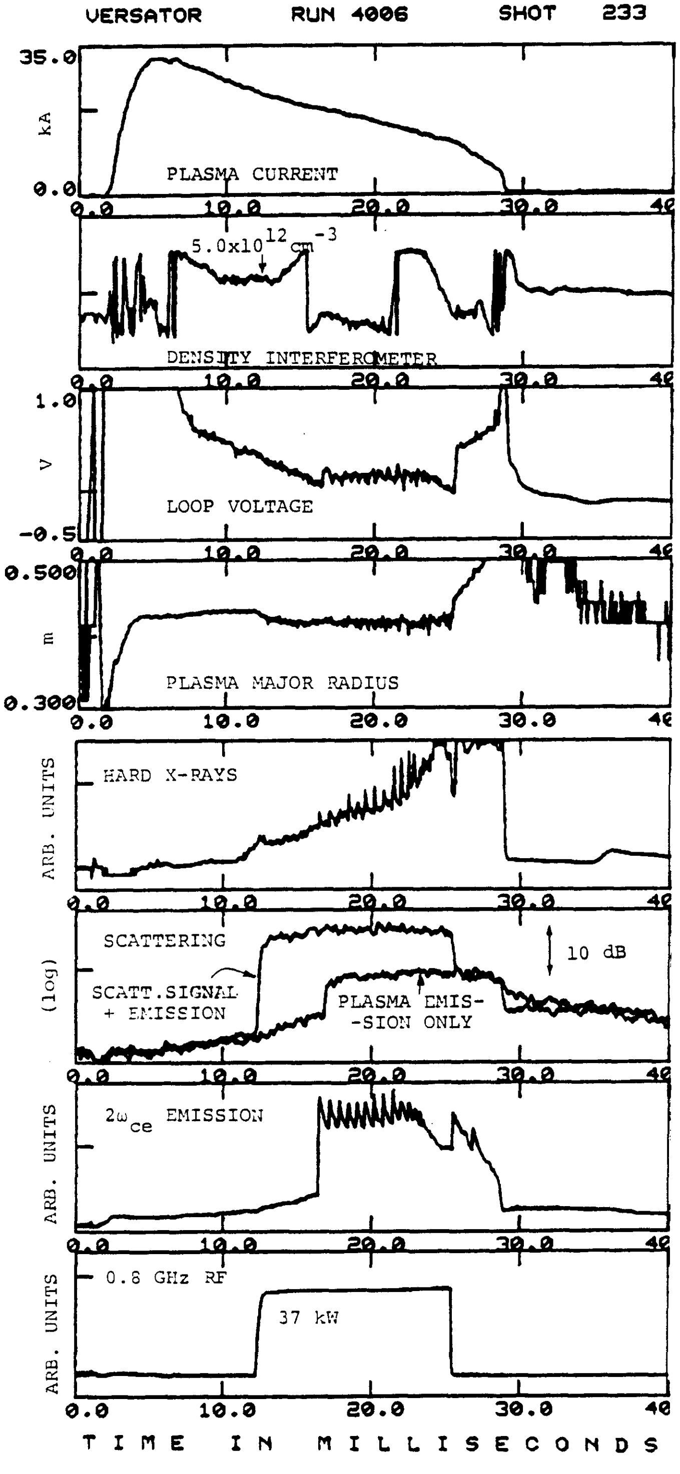

Fig 10.4.1 TYPICAL LOW DENSITY SHOT (+90° phasing)

A typical shot is shown in Fig 10.4.1. As shown by the plasma current trace, the plasma discharge has an initial turn-on phase of about 3 ms followed by a quiescent phase of about 22 ms during which the plasma current decays slowly. The density trace is from a so-called fringe counting circuit, and shows the fractional part of the fringe (one fringe is a phase shift of 2π in the interferometer beam); for our interferometer the (linear) calibration factor is $2.26\times10^{12}\mathrm{cm}^{-3}$ line-average per fringe. The loop voltage and in/out position coils (for the plasma major radius) were described in section [9.9]. The hard X-ray trace comes from a portable detector consisting of a NaI crystal coupled to a photomultiplier tube, and measures bremsstrahlung radiation at the limiter. (The stainless steel limiter defines the plasma boundary and is subject to substantial particle bombardment.)

The traces of particular interest to our experiment are the three at the bottom. The scattered signal is shown on a log scale; the signal is clearly seen during the RF pulse. Also shown on the same frame is the signal seen with the incident scattering beam blocked (by Aluminum foil -- see Fig 10.4.2), so that the

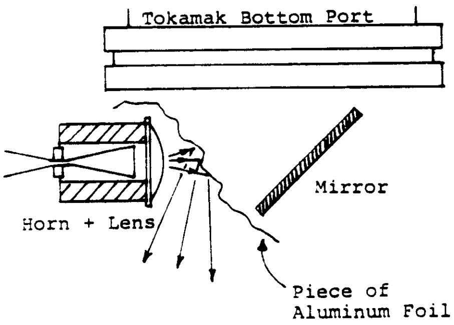

Fig 10.4.2 USE OF ALUMINUM FOIL TO DEFLECT INCIDENT BEAM

receiver sees noise and plasma emission, but no scattered signal. This shows that (1) there is significant plasma emission (2) the emission correlates well with the $2\omega_{ce}$ emission (3) the scattered signal is detectable above the level of the emission and (4) the system is free from RF pickup problems. It is worth pointing out that the usual procedure is to measure the scattered power during the first millisecond after RF turn-on and subtract the emission measured during the last millisecond before RF turn-on. During this first millisecond the plasma emission may be rising, but not so as to introduce serious error. Where the $2\omega_{ce}$ and 139 GHz emissions jump is usually later in the RF pulse, say after 2 or 3 ms.

Typically, we take 2 or 3 good data shots at each datapoint and then move on to the next datapoint. In cases where a break is not necessary between datapoints, datapoints may be changed each shot. Besides data shots, two other kinds of shots are occasionally taken. The first are baseline shots, shots with no plasma (with or without the fields does not matter) that are used to measure the noise level of the receiver. This is necessary since our system is calibrated for the scattered power measured in units of noise power. The second kind of shots are 'Aluminum foil' shots, where the incident beam is blocked off by a piece of Aluminum foil (see Fig 10.4.2). This serves to check that our system remains 'clean' and free from RF pickup, and also to monitor the plasma emission and ensure that our measurements are meaningful. Care is taken with the placement of the Aluminum foil so as not to reflect the beam power back to the EIO, but rather to deflect it downwards and away from the tokamak. Another precaution is to check the spectrum analyzer frequency every once in a while; it occasionally drifts a little.

[10.5] Shutting Down

Very little is involved in shutting down besides turning equipment off. As a matter of good practice, the settings for the scattering system and the 0.8 GHz RF system are usually recorded. The EIO power, the spectrum analyzer frequency and the mirror positions are checked, too.

Section [11] Analysis

The purpose of the analysis is to take the measured signal and compute the lower hybrid wave power, since this is the quantity of interest.

Consider a plasma illuminated with a Poynting flux S_I of (O mode) radiation at frequency ω_I. The electrons are accelerated in the electric field and consequently re-radiate. For a spectrum $n(\vec{k},\omega)$ of electron density fluctuations, the scattered fields and power are straightforward to compute. Scattered radiation with wavevector $\vec{k}_S$ arises from waves with wavevector $\vec{k}_W = \pm(\vec{k}_S - \vec{k}_I)$ where $\vec{k}_I$ is the wavevector of the incident beam. Those electrons in the regions of higher electron density contribute scattered fields in phase, which are only incompletely cancelled by the fields from the fewer electrons in the regions of low density, giving rise to net coherent scattered radiation. (The relationship between the various wavevectors was indicated in Fig 8.1.) The scattered radiation is also frequency shifted by the frequency of the scattering wave. The calculation is performed in Appendix [17]; the result obtained there is

$$\psi(\omega) = S_I\left(\frac{r_o}{R_R}\right)^2 \frac{J}{(2\pi)^6}\,\frac{\left\langle |n^2(\vec{k}_\perp,\omega-\omega_I)| \right\rangle}{T} \qquad \begin{array}{r} 11.01 \\ (17.1.32) \end{array}$$

where $\psi(\omega)$ is power per unit area per unit frequency at frequency ω, r_o is the classical electron radius, R_R is the distance between scattering volume and receiving antenna, J is a geometric factor computed in Appendix [17.2], $n^2(\vec{k}_\perp, \omega-\omega_I)$ is a quantity related to the Fourier transformed wave amplitude squared (defined in Eqn 17.1.28), and T is the time over which the receiver measures power. The receiver sees power P_S

$$P_S = A_R\, C_L \int_{B_R} \psi(\omega)\; d\omega \tag{11.02}$$

where A_R is the effective area of the receiving antenna, B_R is the receiver bandwidth (determined by the spectrum analyzer), and C_L is the transmission loss of the receiving waveguide. In practice we measure $\hat{P}_S$, the ratio of the scattered power to the noise power. Here noise power refers to the instrumental noise of the microwave receiver, referred to the input. This noise is primarily associated with the mixer and preamp.

The density amplitude of the lower hybrid wave can also be used to calculate the lower hybrid wave power. Cold plasma electromagnetic theory is used to relate the density amplitude to the electric field amplitude, from which the Poynting flux is calculated. The calculation is performed in Appendix [18]; the power flow S_e in direction $\hat{e}$ is

$$S_e = \frac{2\varepsilon_0 c}{(2\pi)^5}\left[\left(\frac{cB}{n_e F_2}\right)^2 F_3\right] \int_0^{2\pi} \frac{\cos\alpha\; d\alpha}{2\pi} \int_0^{\infty} \frac{\omega d\omega}{2\pi c} \times$$

$$\times \int_{-\infty}^{\infty} dN_\parallel \frac{k_\perp dk_\perp}{dk_\parallel} \frac{\langle |n^2(\vec{k}_\perp, \omega)| \rangle}{T} \tag*{11.03 (18.2.08)}$$

where is the frequency of the lower-hybrid waves, c, B, n_e, ε_0, $k_\parallel$, $k_\perp$ have their standard meanings, and F_2 and F_3 are dimensionless quantities depending on plasma and wave parameters (Eqns 18.1.13 and 18.1.17). The angle is the angle between $\vec{k}_\perp$ and $\hat{e}$. Ideally one would measure scattered power for many values of α, ω, and $N_\parallel$, and then use Eqn 11.03 to calculate the total power. In practice this is not feasible, and compromises are necessary. The frequency spectrum of the lower-hybrid waves in the plasma has been measured -- the measured bandwidth of 300 kHz is used to perform the ω integral. The α integral is performed by using the neutral assumption that waves propagating radially inwards have the same amplitude for all α, and waves propagating radially outwards have zero amplitude. (In practice this semi-isotropic assumption is found to be poor; this will be the subject of further discussion in Sections [12] and [14]). The $N_\parallel$ integral is left undone; we are content to calculate lower hybrid wave power per unit $N_\parallel$.

We eliminate the lower hybrid wave amplitude from the equations for the scattered power and the lower hybrid wave power, and use (1) the transmission system calibration of Appendix [19.4] to eliminate S_I A_R C_L in favor of measurable quantities and (2) the mixer calibration of Appendix [19.2] for the noise power. Thus the master equation is obtained

$$\hat{I}(N_{\parallel}) = \frac{2(2\pi)^{3/2}}{P_L} \left[\frac{\omega^2 \varepsilon_0}{c} \cdot F_3 \left(\frac{cB}{n_e F_2}\right)^2 \cdot \frac{N_{\perp}\, dN_{\perp}}{dN_{\parallel}}\right] \left[\frac{1}{J}\left(\frac{R_R R_X}{(R_R+R_X)\, r_0}\right)^2\right] \times$$

$$\times \left[\frac{B_R B_W}{\sqrt{B_R^2+B_W^2}}\right]\left[\frac{kT_R}{P_C}\right] \hat{P}_S \qquad 11.04$$

where $\hat{I}(N_{\parallel})$ is the lower-hybrid wave power per unit $N_{\parallel}$ per unit area per unit launched power, and most other quantities have been mentioned above. $kT_R B_R$ is the noise power in the receiver bandwidth B_R, the wave bandwidth B_W=300 kHz, P_L is the launched 0.8 GHz lower-hybrid power and P_C is the 139 GHz CW transmitted power from the calibration measurement of Appendix [19.4]. R_X is the distance from the transmitting antenna to the scattering volume. This equation is of the form

$$\hat{I}(N_{\parallel}) = C\, \hat{P}_S \qquad 11.05$$

where the product CP_L can be computed from known plasma parameters and scattering geometry, and P_L is measured. CP_L is calculated by programs SCATBACL and SBATPREP2 (described in Appendix [21]) while planning an experiment.

The actual data analysis is done using an interactive program 2MM4016. This program calculates the scattered power from the measured signal and multiplies by C to get $\hat{I}(N_{\parallel})$. The computation of the scattered power involves converting the log signal to 'real' units, and subtracting the emission and noise (measured just before the 0.8 GHz system is turned on.) Details on 2MM4016 may be found in Appendix [21.4].

The significance of the quantity $\hat{I}(N_{\parallel})$ is that, to the extent that the model assumptions are valid,

$$A_W \int dN_{\parallel} \hat{I}(N_{\parallel}) = 1 \qquad 11.06$$

where A_W is the cross-sectional area of the lower hybrid beam measured normal to $\hat{r}$.

Data are presented in terms of $\hat{I}(N_{\parallel})$, except for experiments such as the power scan where the scattering geometry is the same for all datapoints.

Section [12] EXPERIMENTAL RESULTS

[12.1] Introduction

A number of experiments have been performed, measuring the variation of lower hybrid wave power with different parameters. The radial scans and $N_{\parallel}$ spectra (sub-sections [12.2] and [12.3]) constitute the core of this thesis. Sub-section [12.4] covers an experiment that tests the isotropy of lower hybrid power flow, by varying the orientation of the detected wavevector. Absorption of wave power was investigated indirectly by comparing cases with +90° and -90° phasing of the lower hybrid antenna; this is the subject of [12.5]. Lastly, sub-section [12.6] describes three other experiments: frequency spectrum, poloidal scan and power scan. The experiments are summarized in Table 12.1.1.

The current drive density limit observed on Versator at 0.8 GHz is $6 - 7 \times 10^{12} \mathrm{cm}^{-3}$ [Luckhardt.82]. Almost all experiments were performed at low density ($4.5 - 5 \times 10^{12} \mathrm{cm}^{-3}$ line average, in the current drive regime) and with +90°

Table 12.1.1 LIST OF EXPERIMENTS

Experiment	Conditions	Run#	Figure
Radial Scan	Low Density $N_{\parallel}=3$	4003	12.2.1
Radial Scan	Low Density $N_{\parallel}=5$	4003	12.2.2
Radial Scan	High Density $N_{\parallel}=3$	4004	12.2.3
Radial Scan	High Density $N_{\parallel}=5$	4004	12.2.4
$N_{\parallel}$ Spectrum	Low Density r/a=0.85	4006	12.3.1
$N_{\parallel}$ Spectrum	Low Density r/a=0.0	4006	12.3.2
$N_{\parallel}$ Spectrum	High Density r/a=0.85	4015	12.3.3
$N_{\parallel}$ Spectrum	High Density r/a=0.0	4015	12.3.4
$N_{\parallel}$ Spectrum	180° Phasing r/a=0.85	4018	12.3.5
$N_{\parallel}$ Spectrum	180° Phasing r/a=0.0	4018	12.3.6
Orientation Scan	r/a=0.5 $N_{\parallel}=3.1$ Low Density	4122	12.4.1
Absorption Test +-90° Comparison	r/a=0.0 $N_{\parallel}=3,5$ Low Density	4030, 4103	Table 12.5.1
Frequency Spectrum	r/a=0.5 $N_{\parallel}=3$ Low Density	4204	12.6.1
Power Scan	r/a=0.5 $N_{\parallel}=3$ Low Density	4125	12.6.2
Poloidal Scan	r/a=0.82 $N_{\parallel}=3.2$ Low Density	4124	12.6.3

phasing of the 0.8 GHz lower hybrid antenna (this is the current drive phasing). A set of radial scans and $N_{\parallel}$ spectra was measured at a density ($8 \times 10^{12} cm^{-3}$ line average) above the density limit. Exceptions to the +90° phasing are a pair of $N_{\parallel}$ spectra measured for 180° phasing, and the -90° phasing used in the absorption test.

Other parameters also assumed some 'standard' values over the course of the experiments. Plasmas were run with toroidal field of 1.2 T and plasma currents of 25 kA typically. Scattering volumes were centered on the horizontal midplane for all experiments except the poloidal scan (sub-section [12.5]). The scattering geometry was oriented to look for waves propagating horizontally (specifically with $\vec{k}_{\perp}$ within 1.2° of the horizontal); this is illustrated in Fig 12.1.1. The obvious exception to this is the orientation scan of sub-section [12.4].

[12.2] Radial Scans

Radial scans were conducted at two values of $N_{\parallel}$, nominally 3 and 5. The parameters are 'nominal' because of the finite size of the scattering volume; any scattering volume will detect waves over a spread in spatial locations and $N_{\parallel}$ values. Radial scans were performed with +90° waveguide phasing at densities both above and below the current drive density limit, as discussed above.

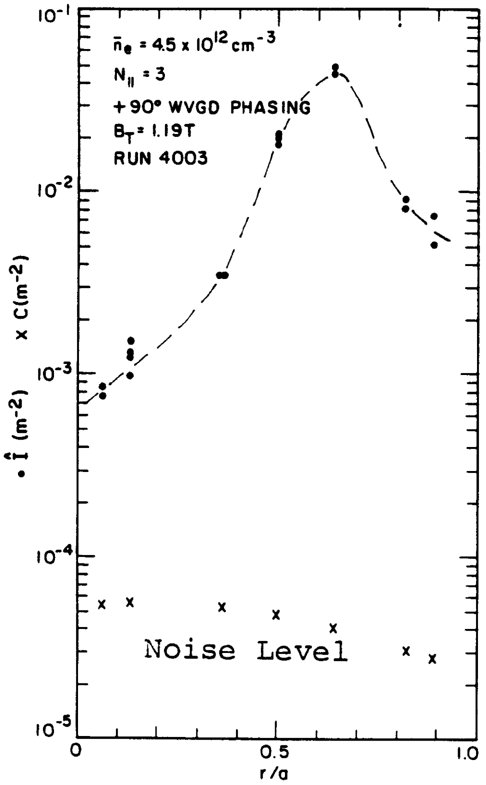

Fig 12.2.1 RADIAL SCAN $N_{\parallel}=3$, Low Density, $+90^{\circ}$ Phasing

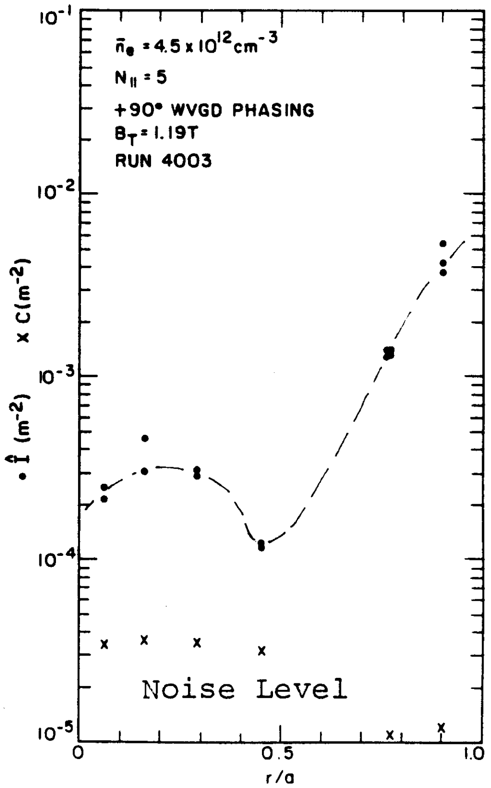

Fig 12.2.2 RADIAL SCAN $N_{\parallel}=5$, Low Density, $+90^{\circ}$ Phasing

The graphs show $\hat{I}(N_{\parallel})$, which is a measure of the normalized lower hybrid power flow, and C, a scaling factor numerically equal to the noise level of the system, versus normalized minor radius r/a.

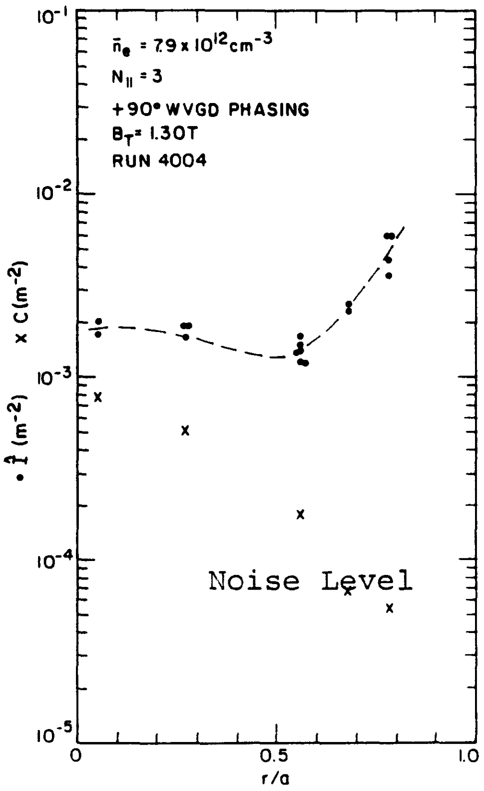

Fig 12.2.3 RADIAL SCAN $N_{\parallel}=3$, High Density, +90° Phasing

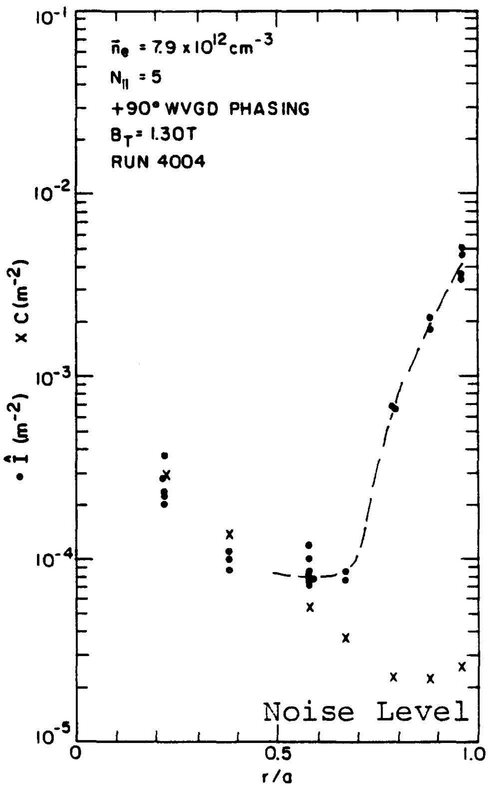

Fig 12.2.4 RADIAL SCAN $N_{\parallel}=5$, High Density, +90° Phasing

The graphs show $\hat{I}(N_{\parallel})$, which is a measure of the normalized lower hybrid power flow, and C, a scaling factor numerically equal to the noise level of the system, versus normalized minor radius r/a.

Fig 12.2.1 shows the low-density radial profile for $N_\parallel = 3$. Before discussing the data, a couple of general remarks are in order. First, the quantity plotted is the derived quantity $\hat{I}(N_\parallel)$, a measure of the lower-hybrid wave power discussed in section [11], versus r/a, the normalized minor radius. Also shown for reference is the quantity C used to convert scattered power to lower hybrid wave power via Eqn 11.05.

$$\hat{I}(N_\parallel) = C\,\hat{P}_S \qquad \begin{array}{r} 12.2.01 \\ (11.05) \end{array}$$

When $\hat{P}_S = 1$ (scattered power equals noise power), $\hat{I}(N_\parallel) = C$, so that the location of C on the plot may be used to judge the noise level of the system. Second, one notices a shot-to-shot variation in the signal levels by a factor of 1.5 to 2. This variation is always present, and is essentially independent of signal level or any experimental parameter. The variation does increase for smaller spectrum analyzer bandwidths, however, and is thought to be principally due to spectrum analyzer noise. The mean of several shots should be a reliable indicator of the true signal level; also, a factor of 2 is not serious when $\hat{I}(N_\parallel)$ varies by factors of 10 or more between different datapoints in an experiment.

Returning to Fig 12.2.1, we see a strong peak at r/a = 0.65, with the power level decaying by about 2 orders of magnitude from there to the plasma center. The peak in the power is thought to be the 1st pass resonance cone of rays with positive $N_{\parallel}$ travelling the short way around the tokamak (45°) from the lower hybrid waveguide grill to the scattering plane, both because of ray-tracing calculations (sections [13] and [14]) and because of the highly directional power flow (Fig 12.4.1, discussed below). We observe that even at the center, the signal is 10 dB above the noise level, and conclude that power does reach the center of the plasma. Saying how much reaches the center is however quite another matter. The measured quantity is really the directional power flow per unit area, and beam broadening and loss of directivity (due to refraction and wave scattering) would cause the measured signal to drop going from edge to center, even if all the wave power did penetrate to the center of the plasma. Consider that a resonance cone might have an area (normal to $\hat{r}$) of about 300 cm^2 (this is the area of the face of the lower hybrid antenna), and a magnetic surface at $r = 5$ cm has a surface area of around 8000 cm^2, so that beam broadening alone could account for a drop by a factor of 25 - 30 in $\hat{I}(N_{\parallel})$. Therefore we are unable to conclude from the radial profile whether or not the bulk of the power reaches the center. (A separate experiment was performed specifically to address the question of absorption during current drive; it is discussed below in [12.5].)

For comparison, Fig 12.2.2 shows a radial profile from the same run, but for $N_{\parallel} = 5$. The power level is generally lower, as expected from our knowledge of the computed launched spectrum (shown in Fig 9.9.2), and the peak is missing. $\hat{I}(N_{\parallel})$ does drop by an order of magnitude from edge to center.

Figs 12.2.3 and 12.2.4 show radial profiles for the high density case, at $N_{\parallel} = 3$ and 5 respectively. Neither graph has the peak of Fig 12.2.1 (It is perhaps worth mentioning that the experiment of Fig 12.2.1 was repeated, and reproduced extremely well.) It would appear that the lower $N_{\parallel}$ penetrates further into the plasma, at $N_{\parallel} = 5$ the signal drops rapidly to the point where signal equals noise. Consistent with the observation for the low density case, the power level for $N_{\parallel} = 5$ is lower than for $N_{\parallel} = 3$.

[12.3] $N_{\parallel}$ Spectra

Fig 12.3.1 shows an $N_{\parallel}$ spectrum for the low density case at a location near the outside edge. Except for a couple of shots at one datapoint, the fit to an exponential is excellent. The computed launched spectrum is also shown for comparison (this has been scaled by a constant factor to match the data). The agreement is quite good. Fig 12.3.2 shows the spectrum measured at the center of the plasma. As expected, we see less power than at the edge. The spectrum at the center is noticeably flatter, too. This would appear hard to reconcile with the previous statement that lower $N_{\parallel}$ penetrates farther into the plasma. However a look at the

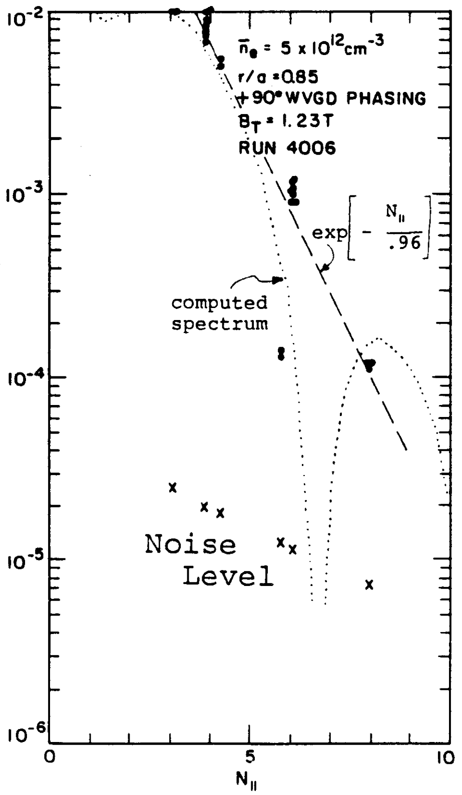

Fig 12.3.1 $N_{\parallel}$ SPECTRUM r/a=0.85, Low Density, +90° Phasing

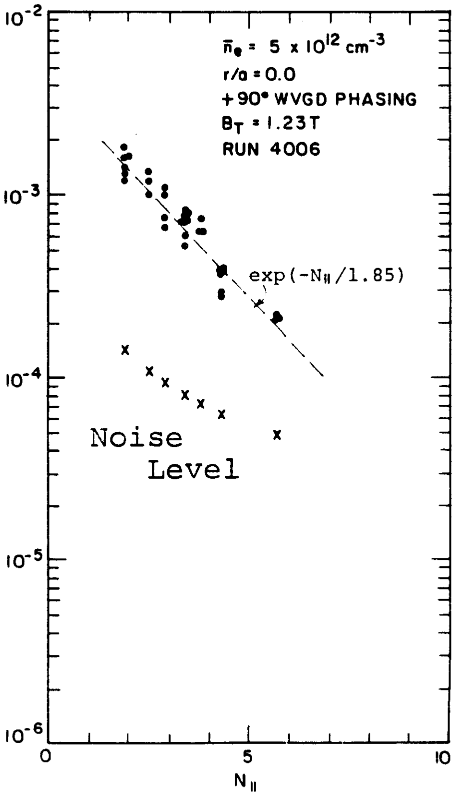

Fig 12.3.2 $N_{\parallel}$ SPECTRUM r/a=0.0, Low Density, +90° Phasing

The graphs show $\hat{I}(N_{\parallel})$, which is a measure of the normalized lower hybrid power flow, and C, a scaling factor numerically equal to the noise level of the system, versus $N_{\parallel}$. In Fig 12.3.1 the exponential fit (- - -) and the computed spectrum (....) are also shown.

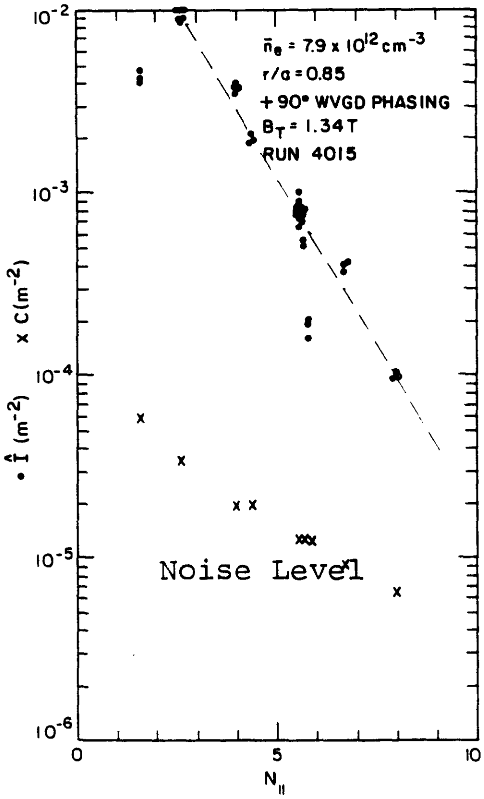

Fig 12.3.3 $N_{\parallel}$ SPECTRUM r/a=0.85, High Density, +90° Phasing

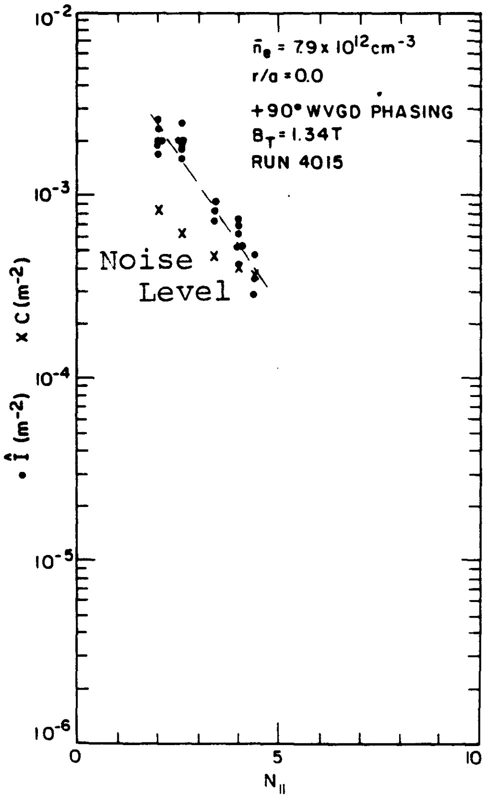

Fig 12.3.4 $N_{\parallel}$ SPECTRUM r/a=0.0, High Density, +90° Phasing

The graphs show $\hat{I}(N_{\parallel})$, which is a measure of the normalized lower hybrid power flow, and C, a scaling factor numerically equal to the noise level of the system, versus $N_{\parallel}$.

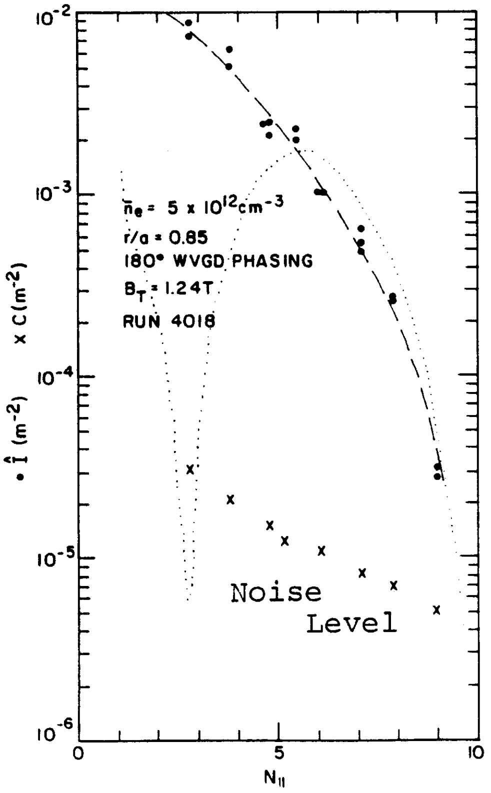

Fig 12.3.5 $N_{\parallel}$ SPECTRUM r/a=0.85, Low Density, 180° Phasing

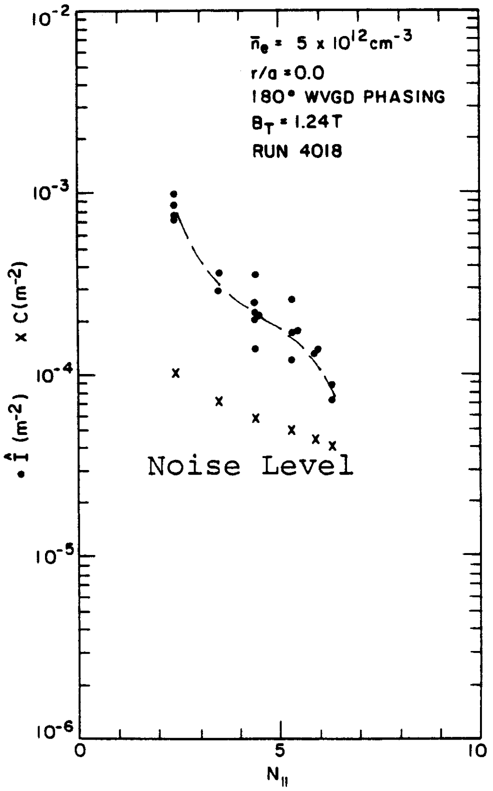

Fig 12.3.6 $N_{\parallel}$ SPECTRUM r/a=0.0, Low Density, 180° Phasing

The graphs show $\hat{I}(N_{\parallel})$, which is a measure of the normalized lower hybrid power flow, and C, a scaling factor numerically equal to the noise level of the system, versus $N_{\parallel}$. In Fig 12.3.5 the computed spectrum (....) is also shown.

radial profiles Fig 12.2.1 and 12.2.2 shows that the shapes of the two radial profiles are quite different, indicating that comparison of edge and center $N_{\parallel}$ spectra is not a good indicator of how far the various waves penetrate into the plasma.

Figs 12.3.3 and 12.3.4 show likewise the $N_{\parallel}$ spectra for the high density case, for $r/a = 0.85$ and $r/a = 0$ respectively. The spectra look remarkably similar to the low-density spectra.

Figs 12.3.5 and 12.3.6 show $N_{\parallel}$ spectra from a pair of experiments which in a sense failed. In the light of the reasonably good fit between experiment and theory for the spectrum of Fig 12.3.1, an attempt was made to verify the computed $N_{\parallel}$ spectrum for the case of 180° relative waveguide phasing; this spectrum should have a peak around $N_{\parallel} = 6$. Fig 12.3.5 shows the experimental result near the edge, with the computed spectrum also marked in. Fig 12.3.6 shows the spectrum at the center. The failure of these experiments makes one wonder about the validity of the $N_{\parallel}$ spectra measured for the +90° case (Figs 12.3.1 through 12.3.4). It is natural to speculate whether the experiment is in some way biased towards small $N_{\parallel}$ or small scattering angles. This is the subject of further discussion in Section [14]. The other point to be noted about the $N_{\parallel}$ spectra is that by the definition of $I(N_{\parallel})$,

$$A_W \int dN_{\parallel} \hat{I}(N_{\parallel}) = 1 \qquad \begin{array}{r} 12.3.1 \\ (11.06) \end{array}$$

yet even using 1 m^2 (the area of a magnetic surface) for A_W, the discrepancy between Eqn 12.3.1 and Fig 12.3.1 is over one and a half orders of magnitude.

[12.4] Orientation Scan

The orientation scan, shown in Fig 12.4.1, is perhaps the most exciting result to emerge in our experiments. Here a set of scattering volumes was taken with the same spatial location and scattering angle, but with varying $\vec{k}_\perp$ orientation. The wave power is seen to be highly directional, dropping by an order of magnitude in less than 10°. There is also a noticeable offset in the peak, about 4° from horizontal. Other orientation scans at different poloidal locations also showed the steep drop, though not cleanly on both sides.

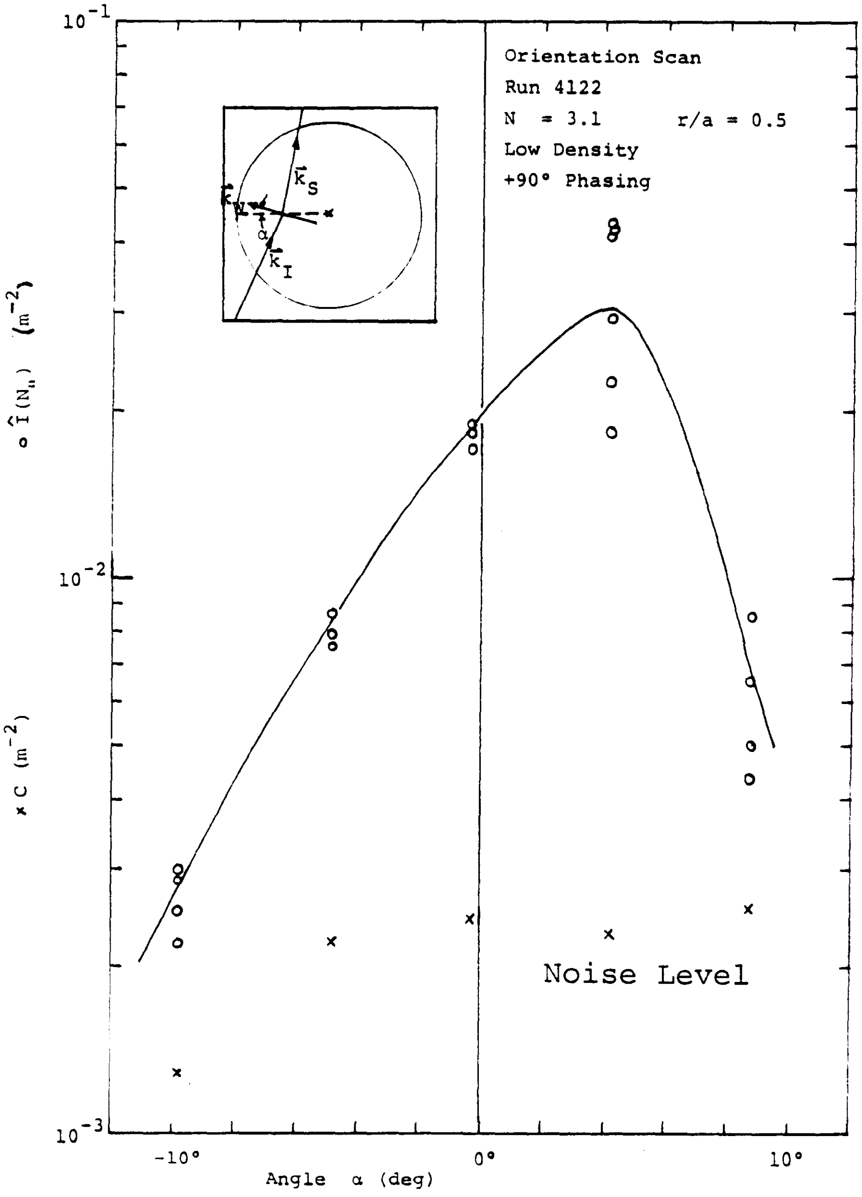

Fig 12.4.1 ORIENTATION SCAN

r/a=0.5 $N_\parallel$=3.1 Low Density and +90° Phasing. A set of scattering volumes was chosen at the same spatial location, with the same scattering angle, but oriented differently in the scattering plane. [The inset shows the scattering geometry for a positive angle α.] The graph shows $\hat{I}(N_\parallel)$, which is a measure of the normalized lower hybrid power flow, versus α, the angle between $k_\perp$ of the detected wave and the horizontal.

[12.5] Absorption Test

A special experiment was performed to look for wave absorption during current drive. The idea is that waveguide phasings of +90° and -90° launch identical spectra, but in opposite directions. Waves with positive $N_{\parallel}$ should be absorbed during current drive, so that one may compare scattered signals from shots with +90° and 90° phasings, and so infer something about wave absorption. The measurements were performed at the plasma center, so as to get away from the strong resonance cone near the edge. The basic assumption in this experiment is that due to scattering and refraction, the wave power is diffuse and toroidally symmetric by the time it reaches the center. (This assumption is neither clearly good nor clearly bad.) Table 12.5.1 shows the results gathered over three runs with two different values of $N_{\parallel}$; we see that the signal from -90° shots is consistently higher than from +90° shots --

---

Table 12.5.1 COMPARISON BETWEEN +90° AND -90° PHASING ON SCATTERED POWER P_S AT PLASMA CENTER. <Expectation Values> and standard deviations are indicated.

RUN	$\hat{P}_S$ (-90°)	$\langle\hat{P}_S(-90°)\rangle$	$\hat{P}_S$ (+90°)	$\langle\hat{P}_S(+90°)\rangle$	$\frac{\langle\hat{P}_S(-90°)\rangle}{\langle\hat{P}_S(+90°)\rangle}$
4030 $N_{\parallel}=3$	8.73± 0.88 10 shots	8.73±0.28	6.21± 0.72 11 shots	6.21±0.22	1.40±0.07
4103 $N_{\parallel}=3$	7.97± 2.51 9 shots	7.97±0.84	5.87± 0.81 7 shots	5.87±0.31	1.36±0.16
4103 $N_{\parallel}=5$	3.54± 1.40 13 shots	3.54±0.39	1.95± 0.71 11 shots	1.95±0.21	1.82±0.28

although not by much (40%). If our assumption is valid, this is evidence for wave absorption during current drive. Also, the wave absorption is not strong first pass absorption (if it were, the difference between -90° and +90° would have been greater).

[12.6] Other Experiments

Several other basic experiments were performed. In Fig 12.6.1 a frequency spectrum is shown; this spectrum was measured with the receiver set to a 30 kHz bandwidth. The figure also shows two fitted spectra; one a Gaussian and the other a peaked spectrum characteristic of weak scattering. The FWHM of the Gaussian spectrum is 400 kHz, not the same as the value (300 kHz, from an older experiment) used for the data analysis, but the systematic error introduced is inconsequential.

A power scan was performed, as shown in Fig 12.6.2, to verify linear dependence between scattered power and launched power (although parametric decay at high power levels may affect the dependence). The log-log fit over two orders of magnitude is excellent; unfortunately the slope differs from unity by nearly 20%. The excellence of fit suggests that the problem lies in calibration of either the scattering system or the RF system. A repeat calibration of the scattering system returned a value of 4.90 dB/Volt instead of the old value 4.60 dB/Volt; this is not enough to

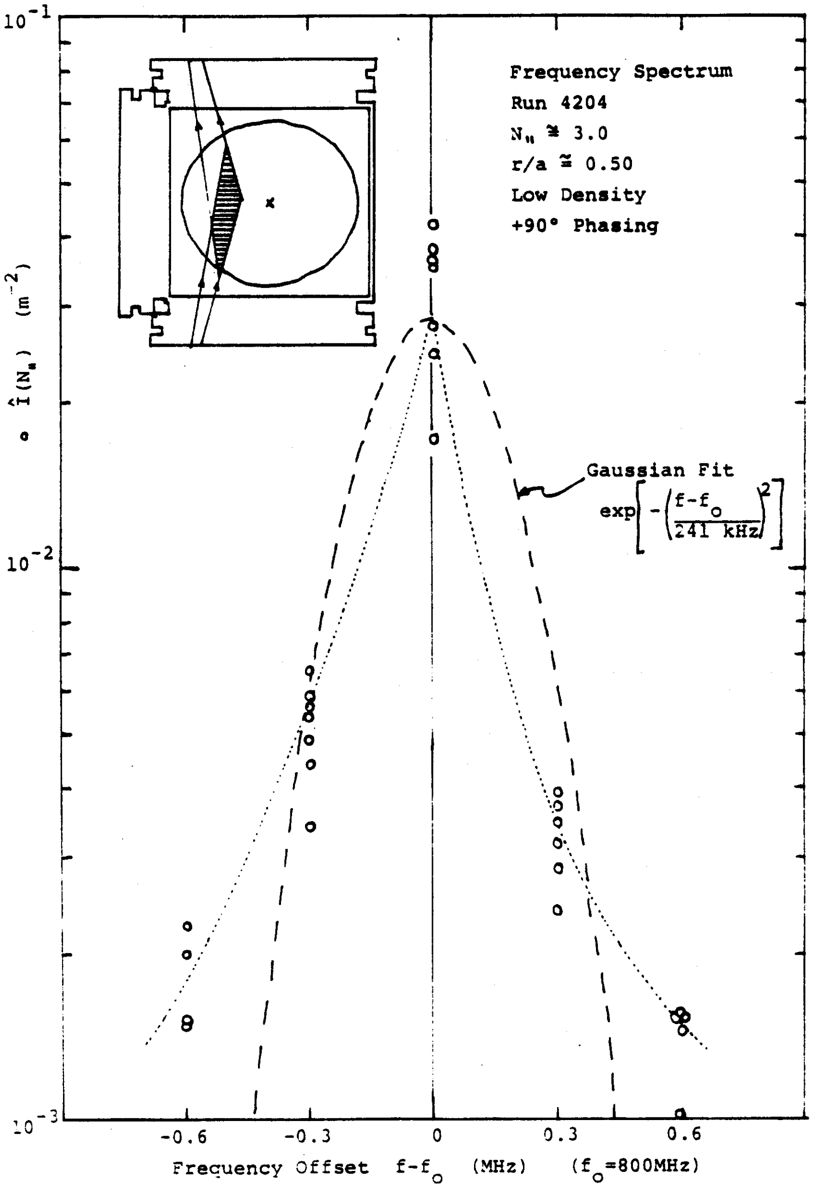

Fig 12.6.1 FREQUENCY SPECTRUM

$r/a=0.5$ $N_\parallel=3.0$ Low Density and +90° Phasing. The graph shows $\hat{I}(N_\parallel)$, which is a measure of the normalized power flow, versus the frequency difference between detected wave and pump wave. Measurements were made with a 30 kHz bandwidth. The inset shows the scattering geometry used. A fitted Gaussian is shown (- - -) as well as a more peaked fit (....).

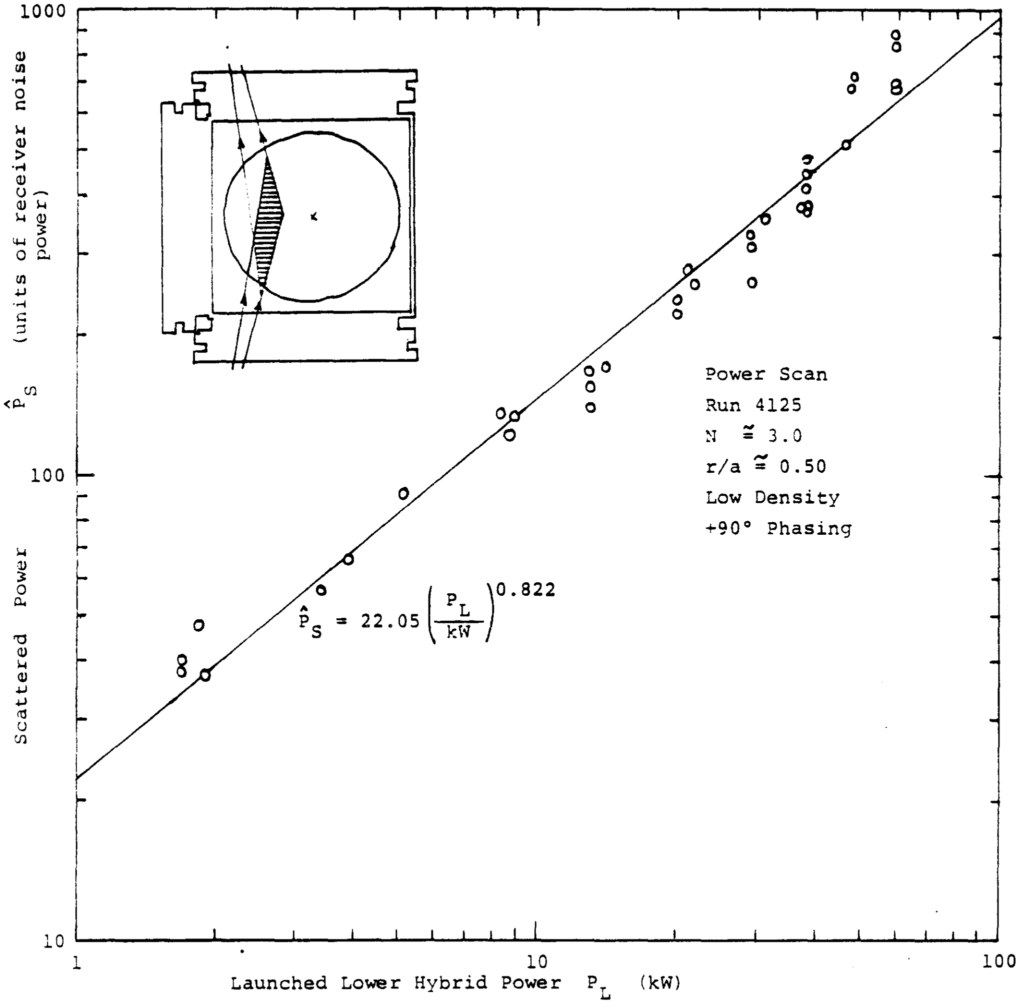

Fig 12.6.2 POWER SCAN

r/a=0.5 $N_{\parallel}$=3.0 Low Density and +90° Phasing. The normalized scattered power is shown as a function of the launched lower hybrid power P_L. The inset shows the scattering geometry used.

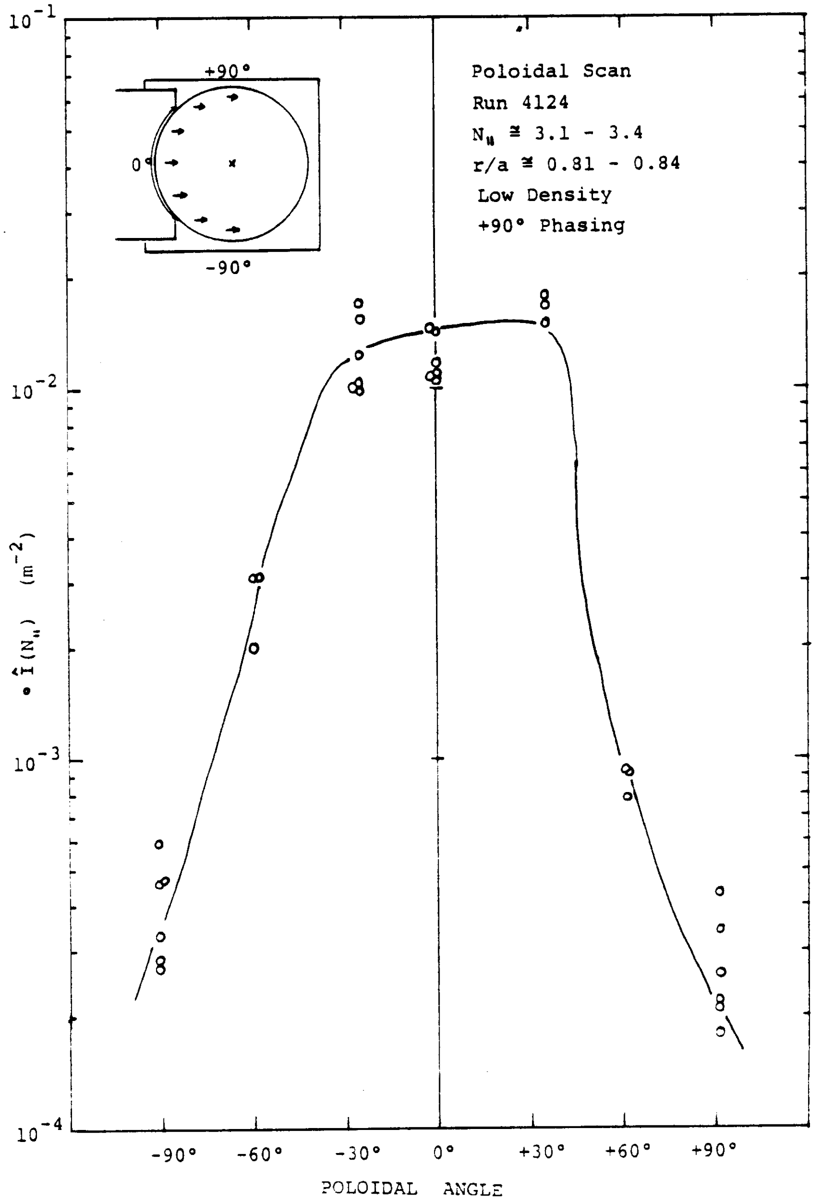

Fig 12.6.3 POLOIDAL SCAN

$r/a=0.81-0.84$ $N_{\parallel}=3.1-3.4$ Low Density and +90° Phasing. A set of scattering volumes was chosen with the same scattering angle and orientation, at the same distance from the plasma center, but at different poloidal angles. [The inset shows the detected wavevectors for the 7 scattering volumes used.] The graph shows $\hat{I}(N_{\parallel})$, which is a measure of the normalized lower hybrid power flow, versus poloidal angle.

account for the discrepancy in the power scan, so at the present time the RF system calibration is still suspect.

Results from a poloidal scan are presented in Fig 12.6.3. As shown in the inset, several scattering volumes were taken around the plasma periphery (r/a = 0.85), all oriented to look for waves with horizontal wavevectors. The flat peaked graph is entirely reasonable in view of the fact that the waveguide grill is in contact with the plasma over the poloidal angles $-46° < \theta < 46°$ (this is shown in the inset of Fig 12.6.3).

Section [13] THEORETICAL MODELLING

[13.1] Outline

In order to relate the experimental results to theory, it is necessary to compute from available theories quantities that may be related to experiment. This section describes a numerical study of the lower-hybrid wave power distribution in a poloidal cross-section of the tokamak (the scattering plane). The computation, details of the model, and results are discussed; comparison between experiment and theory is covered in the following section. The idea is that the lower hybrid power flow can be thought of as a composite of rays; each ray can be followed independently to determine the power flow. Sub-section [13.2] discusses the computation of the initial spectrum of launched waves, followed in sub-section [13.3] by a discussion of the ray tracing. Results are presented in [13.4], followed by some miscellaneous computation details in [13.5]. Program listings are too voluminous to permit inclusion in this thesis: listings and more computation details are provided in a separate document [Rohatgi.85b].

[13.2] Launched Wave Spectrum

A code due to M Brambilla [Brambilla.76, Knowlton.85] is used to compute the wave spectrum launched by the lower hybrid 4 waveguide antenna. This spectrum is calculated assuming a finite waveguide grill mouth in contact with an overdense plasma ($\omega_{pe}^2/\omega^2=10$ at the grill mouth) with a linear density gradient, chosen arbitrarily to be (central density)/24cm. The launch geometry is shown in Fig 13.2.1. Poloidal magnetic field and grill mouth curvature are ignored. Vacuum is assumed inside the waveguides. Fields are matched using 4 evanescent waveguide modes in addition to the launched waves. Plasma waves are computed over the range $-15 < N_{\|} < 15$ (no lower hybrid waves exist in $-1 < N_{\|} < 1$); the wave powers are normalized so that the total launched power equals 1. The computed spectrum for the case of +90° relative waveguide phasing was presented previously in Fig 9.9.2. The phase of the launched waves is also computed, for subsequent use during ray tracing.

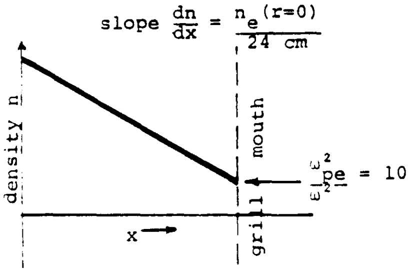

Fig 13.2.1 GEOMETRY FOR BRAMBILLA SPECTRUM COMPUTATION

The density decreases linearly towards the mouth of the 4 waveguide grill.

[13.3] Ray Tracing

Ray tracing is used to follow a large number of rays, keeping track of what the rays 'look like' when they pass through the scattering plane. Paul Bonoli's ray tracing code ZIPRAY [Bonoli.82] was suitably modified and used. The geometry is shown in Fig 13.3.1.

Waves are launched at the grill mouth, which is assumed to lie along a magnetic surface. k_θ is initially taken to be 0; k_r is determined from $N_\parallel$ and the dispersion relation. The initial power of the various waves is chosen to fit the (previously) computed spectrum. During ray tracing, collisional damping and electron and ion Landau damping are taken into account; parametric decay and scattering from low-frequency fluctuations are not. Most rays are followed till they damp (more on this in [13.5]).

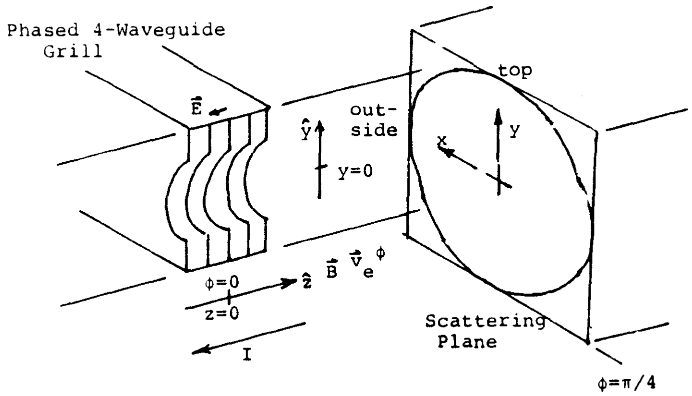

Fig 13.3.1 GEOMETRY FOR RAY TRACING

The ray tracing code assumes the density and temperature profiles within the plasma

$$n_e = (n_{e0} - n_{ea}) \cdot \frac{e^{\xi_n} - e^{\xi_n (r_m/a)^2}}{e^{\xi_n} - 1} + n_{ea} \tag{13.3.1}$$

$$T_{\substack{e\\i}} = (T_0 - T_a) \cdot \frac{e^{-\xi (r_m/a)^2} - e^{-\xi}}{1 - e^{-\xi}} + T_a \tag{13.3.2}$$

and outside the plasma

$$n_e = n_{ea} \frac{e^{-r_m/1.5\mathrm{cm}} - e^{-b/1.5\mathrm{cm}}}{e^{-a/1.5\mathrm{cm}} - e^{-b/1.5\mathrm{cm}}} \tag{13.3.3}$$

$$T_{\substack{e\\i}} = \frac{T_a (b - r_m) + T_b (r_m - a)}{b - a} \tag{13.3.4}$$

where r_m is the magnetic surface radius, a is the plasma minor radius, and b is the wall radius. Other parameters of the plasma model, including the profile factors ξ, are shown in Table 13.3.1. The magnetic geometry incorporates flux shifts, following Shafranov[.67] in the small displacement approximation. For the parameters of Table 13.3.1 the magnetic axis is displaced by about a/8, and this approximation is not good near the plasma edge. Also, the model assumes a circular vacuum vessel, whereas the Versator cross-section is square.

Following ray tracing, a number of analyses can be performed on the computed dataset. These form the subject of the next sub-section.

Table 13.3.1 PLASMA PARAMETERS USED IN RAY TRACING CODE

Quantity	Symbol	Value
Toroidal Field	B_T	1.2 T
Plasma Current	I_p	25 kA
Electron Temperature		
Center	T_{e0}	300 eV
Edge	T_{ea}	10 eV
Wall	T_{eb}	5 eV
Profile Factor	ξ_e	3.5
Ion Temperature		
Center	T_{i0}	150 eV
Edge	T_{ia}	10 eV
Wall	T_{ib}	5 eV
Profile Factor	ξ_i	3.5
Density		
Center	n_{e0}	6.78×10^{12} or 1.19×10^{13} cm^{-3}
Edge	n_{ea}	$0.10 \times n_{e0}$
Wall	n_{eb}	0.0
Profile Factor	ξ_n	-0.571
Major Radius	R	40.5 cm
Minor Radius	a	13.0 cm
Wall Radius	b	15.0 cm
Impurity Atomic Number	Z_{imp}	6
Effective Atomic Number	Z_{eff}	1.5

[13.4] Results

Four cases were run: low density (6.78×10^{12} cm^{-3} peak) with waveguide relative phasings of +90° (the current drive phasing), -90° and 180°, and high density (1.19×10^{13} cm^{-3} peak) at +90°. (These densities correspond closely to the 'low' and 'high' densities of the experiments.) Variations from case to case, while noticeable, were not dramatic. The results presented in this sub-section are restricted to the low-density +90° case, for which Fig 9.9.2 shows the launched spectrum. As indicated above, most rays (84%) terminated normally via damping, but not before making several toroidal passes. The ratio of total power flow across the scattering plane to the total launched power, in some sense the Q of the tokamak, was typically about 5.

Fig 13.4.1 shows a power map in the scattering plane for the low-density +90° case; the inset shows the launched spectrum. The power map may be characterized as splotchy; while wave power does penetrate to the center, it does not do so evenly, despite making a number of toroidal passes. (A mechanism such as scattering of lower hybrid waves from low frequency fluctuations could greatly smooth the power map.) To identify the rays in the brighter regions, we turn to Figs 13.4.2 and 13.4.3 which show, for positive and negative $N_{\parallel}$ rays respectively, puncture plots separated out by toroidal pass number. We see that the bright crescent towards the outside is caused as expected by the 1st pass

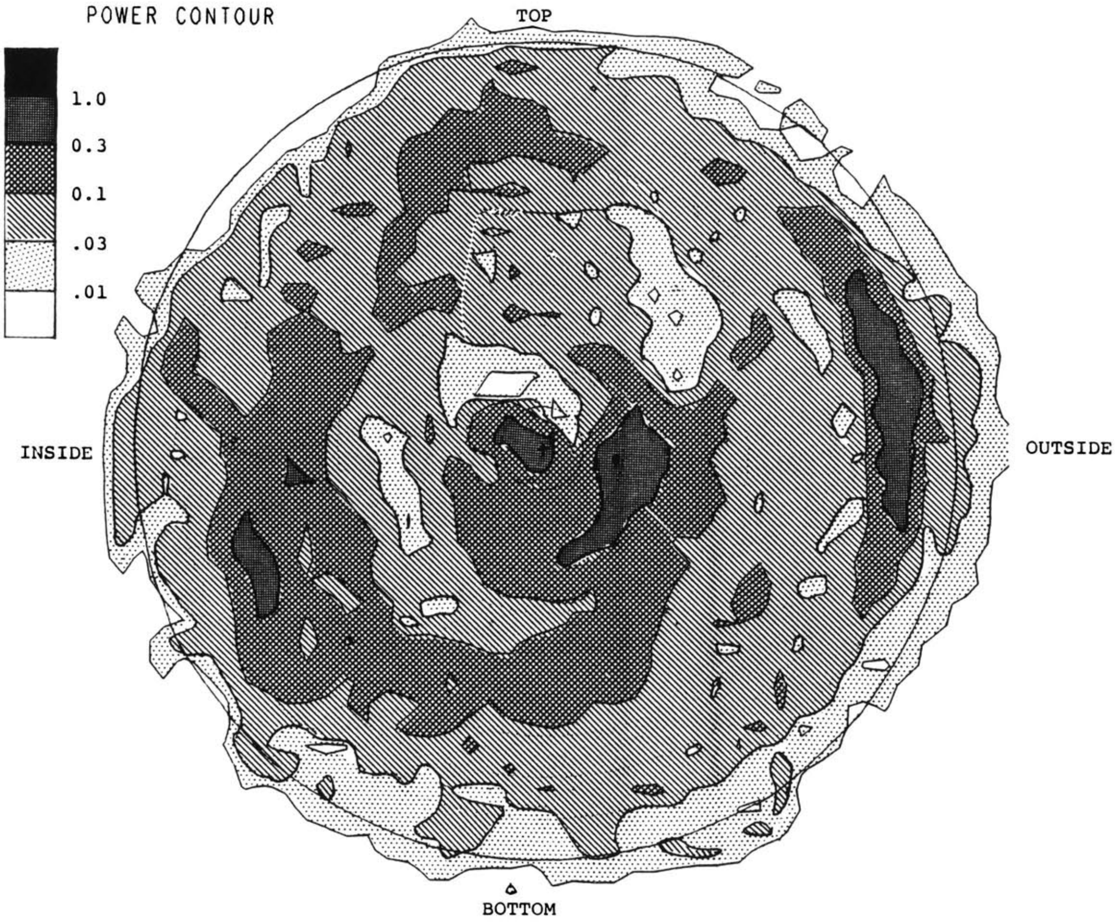

Fig 13.4.1 POWER MAP IN SCATTERING PLANE

Contour plot of computed power density in scattering plane. Contour levels are separated logarithmically as indicated. The peak power density has been arbitrarily scaled to 1.10.

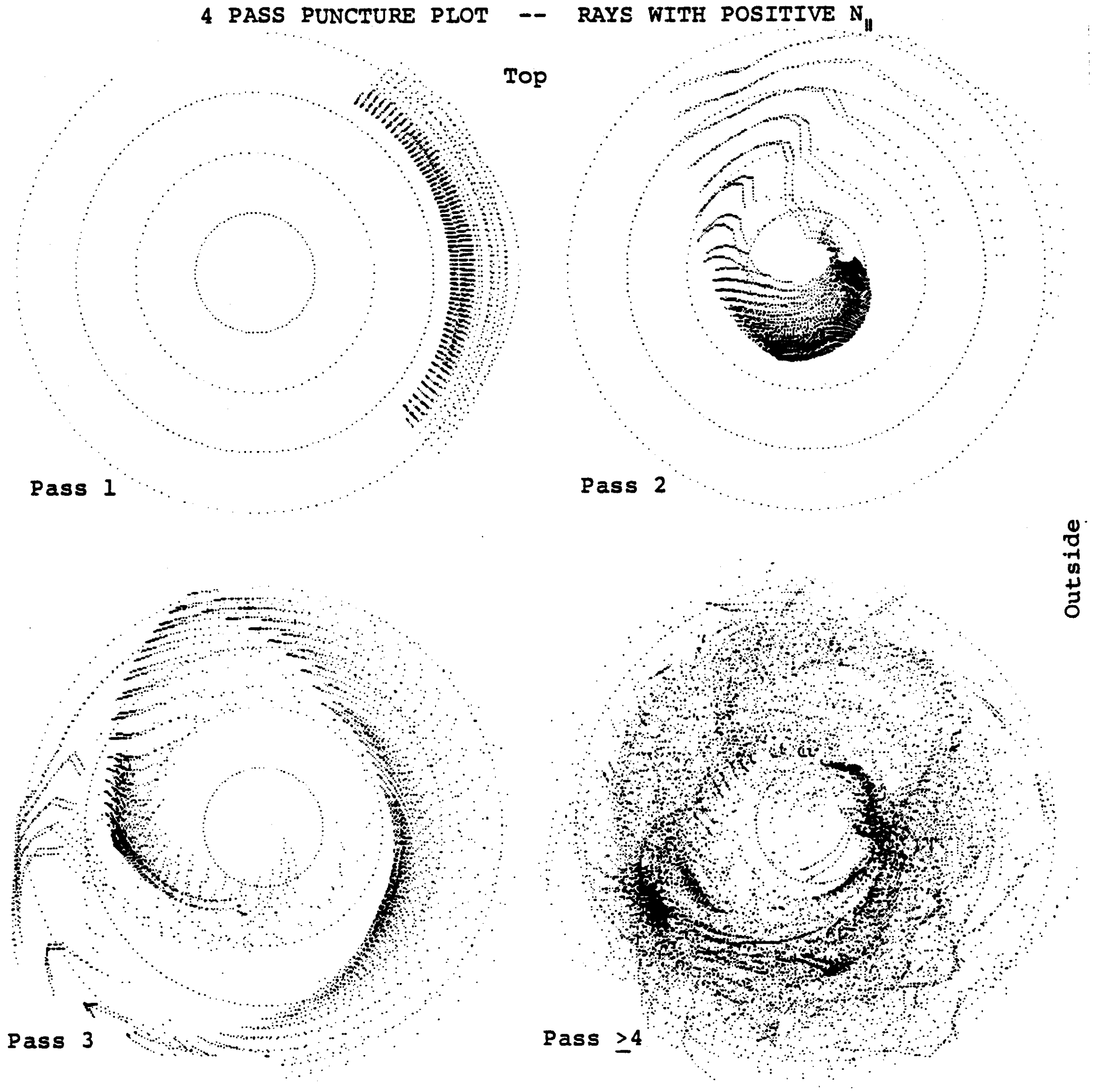

Fig 13.4.2
PUNCTURE PLOT FOR +ve $N_{\parallel}$ RAYS, SEPARATED BY PASSES

One dot corresponds to one ray.

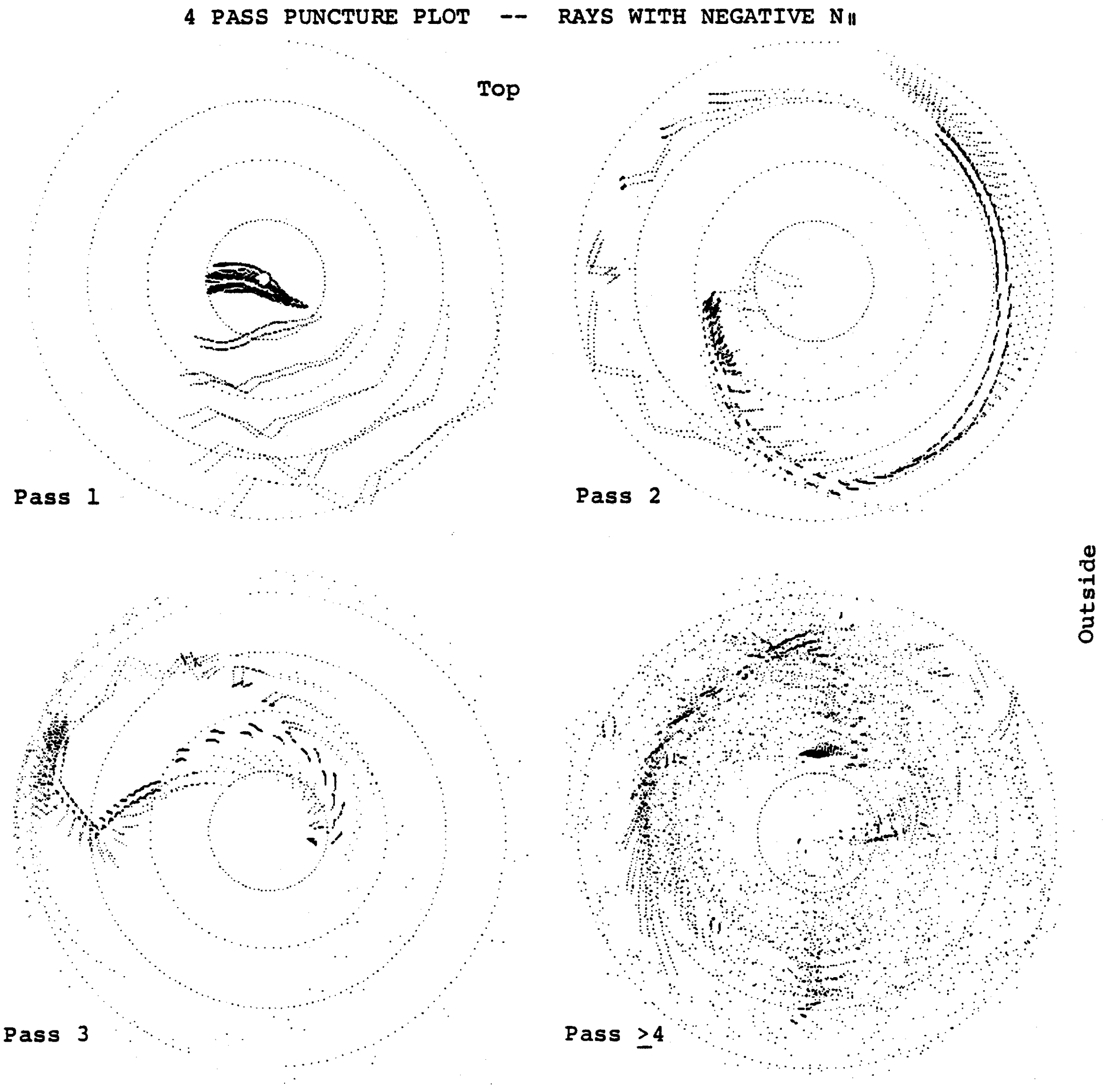

Fig 13.4.3
PUNCTURE PLOT FOR -ve $N_{\parallel}$ RAYS, SEPARATED BY PASSES

One dot corresponds to one ray.

positive $N_{\parallel}$ rays, together with some contribution from the 2nd pass negative $N_{\parallel}$ rays. The bright region at the plasma center is due to 1st pass negative $N_{\parallel}$ rays and 2nd pass positive $N_{\parallel}$ rays. To further study the rays near the center we look at Fig 13.4.4 which shows the local $N_{\parallel}$ spectrum and a spectral/orientation diagram. The latter diagram shows the rays in the chosen spatial region (2cm square, 2cm from the center) on a diagram of $N_{\parallel}$ vs orientation. The orientation of a ray is the direction of the poloidal component of $\vec{k}$, with 0° as outward and 90° as upward. Orientation is important for a scattering experiment, since a scattering experiment is orientation-specific. Notice, though, that the lower-hybrid wave is a backward wave and so the poloidal component of the group velocity is exactly opposite to this. The spectral/orientation diagram in 13.4.4 shows the positive $N_{\parallel}$ rays mostly propagating in the 180° - 240° directions. (The area of the rectangles on a spectral/orientation diagram is proportional to the ray power, and is normalized so that the strongest ray on any diagram is a fixed size.) One may wonder what happened to the first pass negative $N_{\parallel}$ rays that should show up at the center; they do, but in a spatial location adjacent to that of Fig 13.4.4. Fig 13.4.5 shows the $N_{\parallel}$ spectrum and spectral/orientation diagram near the outside, where both the 1st pass positive $N_{\parallel}$ and 2nd pass negative $N_{\parallel}$ rays are visible; the positive $N_{\parallel}$ rays appear to have orientation narrowly centered about 0°. A closer look at the

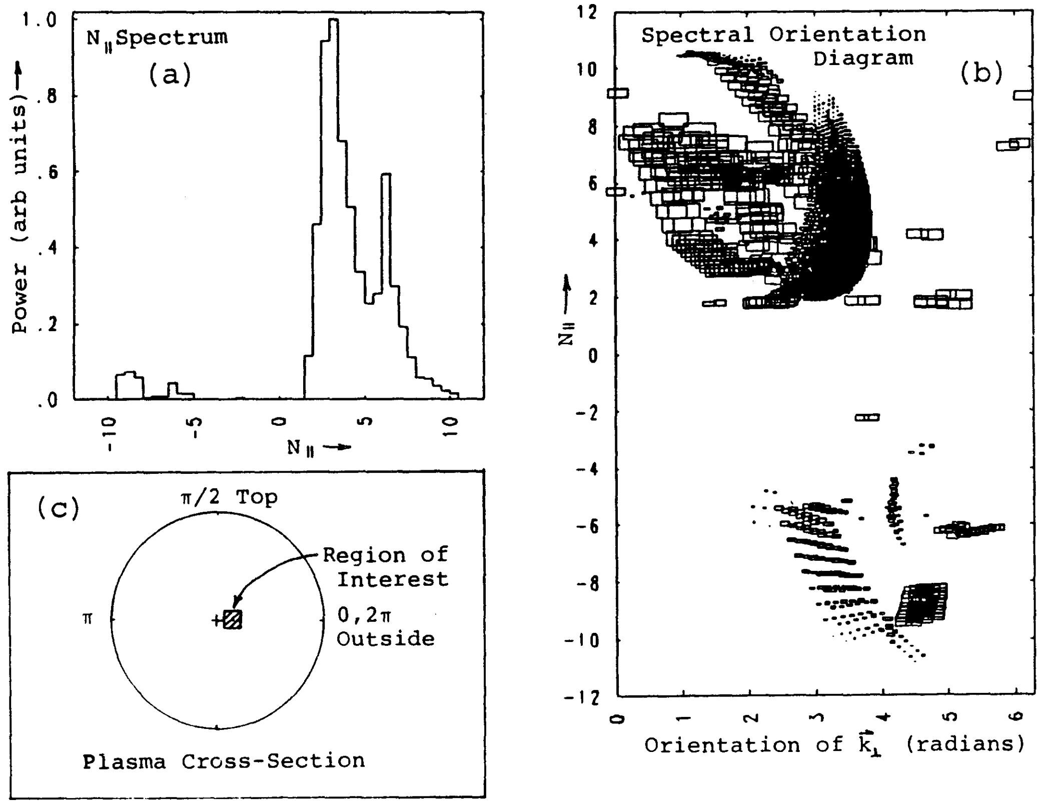

Fig 13.4.4
$N_{\parallel}$ SPECTRUM AND SPECTRAL ORIENTATION DIAGRAM NEAR CENTER

Rays passing through the region of interest (shown in (c)) are plotted on two diagrams. (a) shows the $N_{\parallel}$ spectrum. (b) is a spectral orientation diagram, where a rectangle is plotted for each ray at a coordinate determined by the $N_{\parallel}$ and orientation of the ray. The area of the rectangle is proportional to the power in the ray. The relation of the orientation angle to spatial direction is also indicated in (c).

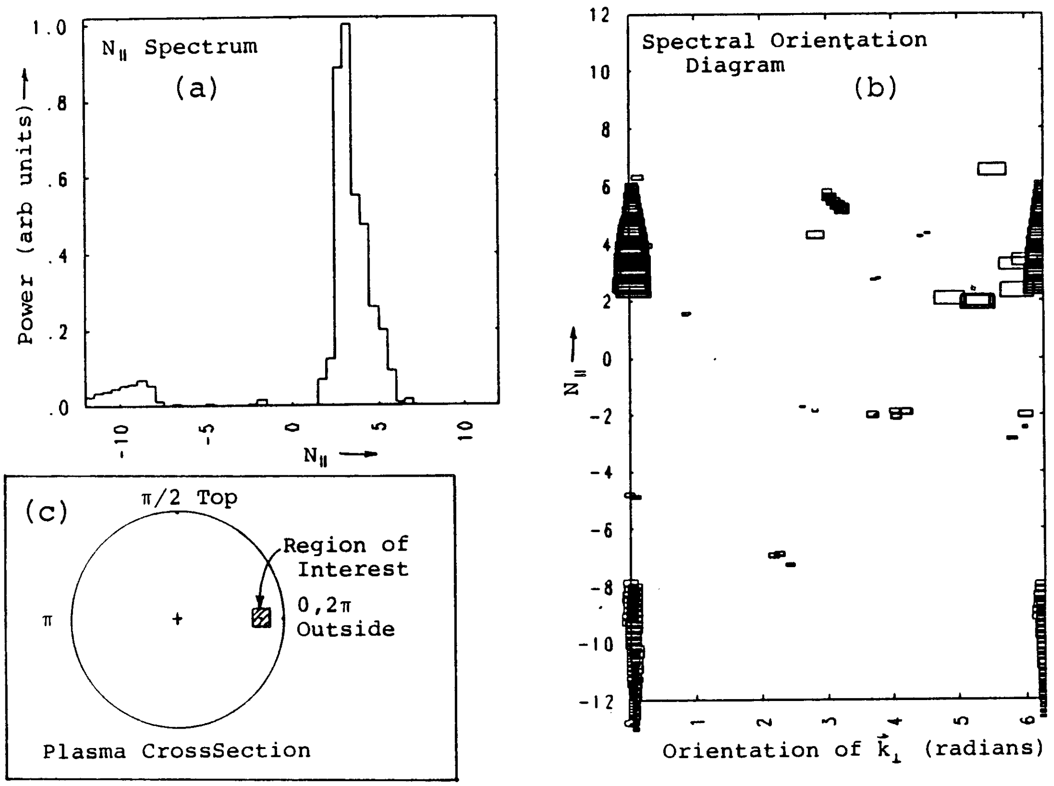

Fig 13.4.5
$N_{\parallel}$ SPECTRUM AND SPECTRAL ORIENTATION DIAGRAM NEAR EDGE

Rays passing through the region of interest (shown in (c)) are plotted on two diagrams. (a) shows the $N_{\parallel}$ spectrum. (b) is a spectral orientation diagram, where a rectangle is plotted for each ray at a coordinate determined by the $N_{\parallel}$ and orientation of the ray. The area of the rectangle is proportional to the power in the ray. The relation of the orientation angle to spatial direction is also indicated in (c).

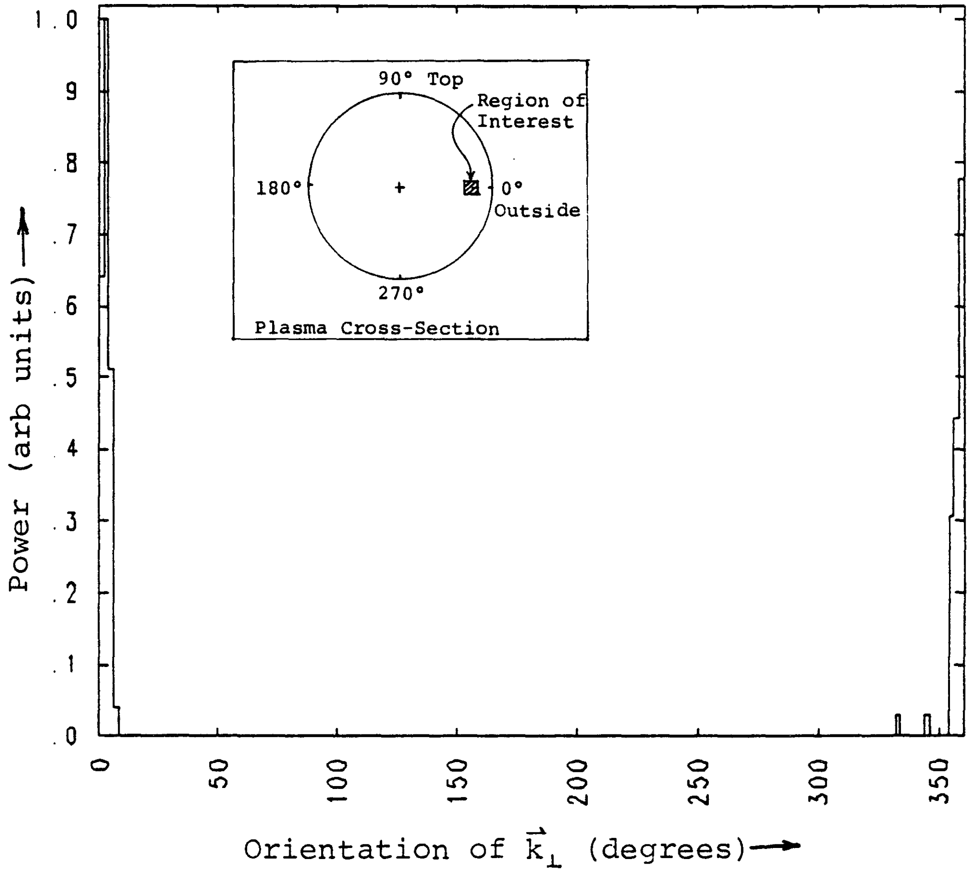

Fig 13.4.6 ORIENTATION SPECTRUM NEAR EDGE

Plot of power vs orientation angle for the rays passing through the region of interest (shown in the inset). The plot is restricted to rays with $N_\parallel$ between 2.5 and 3.5.

orientation spectrum, in Fig 13.4.6, shows a 10 dB full-width of 10°, peaked at +3°. Noticing from Fig 13.4.2 that the 1st pass rays are shifted upwards (as expected for rays following the field lines), this means that the poloidal component of $\vec{k}$ remains essentially radial. This is corroborated by orientation spectra further from the midplane.

One question of interest is how loss of coherence depends on $N_{\parallel}$. To address this question, a quantity related to the wave coherence called the cell size is defined

$$\Delta = \left| \frac{\partial f}{\partial N_{\parallel}} \cdot \frac{\partial f}{\partial y} \cdot \frac{\partial f}{\partial z} \right|^{-1} \tag{13.4.1}$$

where f is the wave phase and y and z are the launching ray coordinates as shown in Fig 13.3.1. (The phase f is corrected to lowest order for the phase difference $\vec{k} \cdot \Delta\vec{r}$ that should exist between coherent waves.) This quantity is of interest for a scattering experiment since scattered electric fields add for coherent waves, but scattered powers add for incoherent waves. (Incoherent waves have a broader $\vec{k}$ spectrum.) The number of waves (in the launching coordinate space) retaining coherence at the scattering plane is directly proportional to the cell size.

Rays were grouped according to their $N_{\parallel}$ (0 to 3, 3 to 6, etc) and the evolution of cell size from pass to pass was studied. The results are shown in Fig 13.4.7. It would

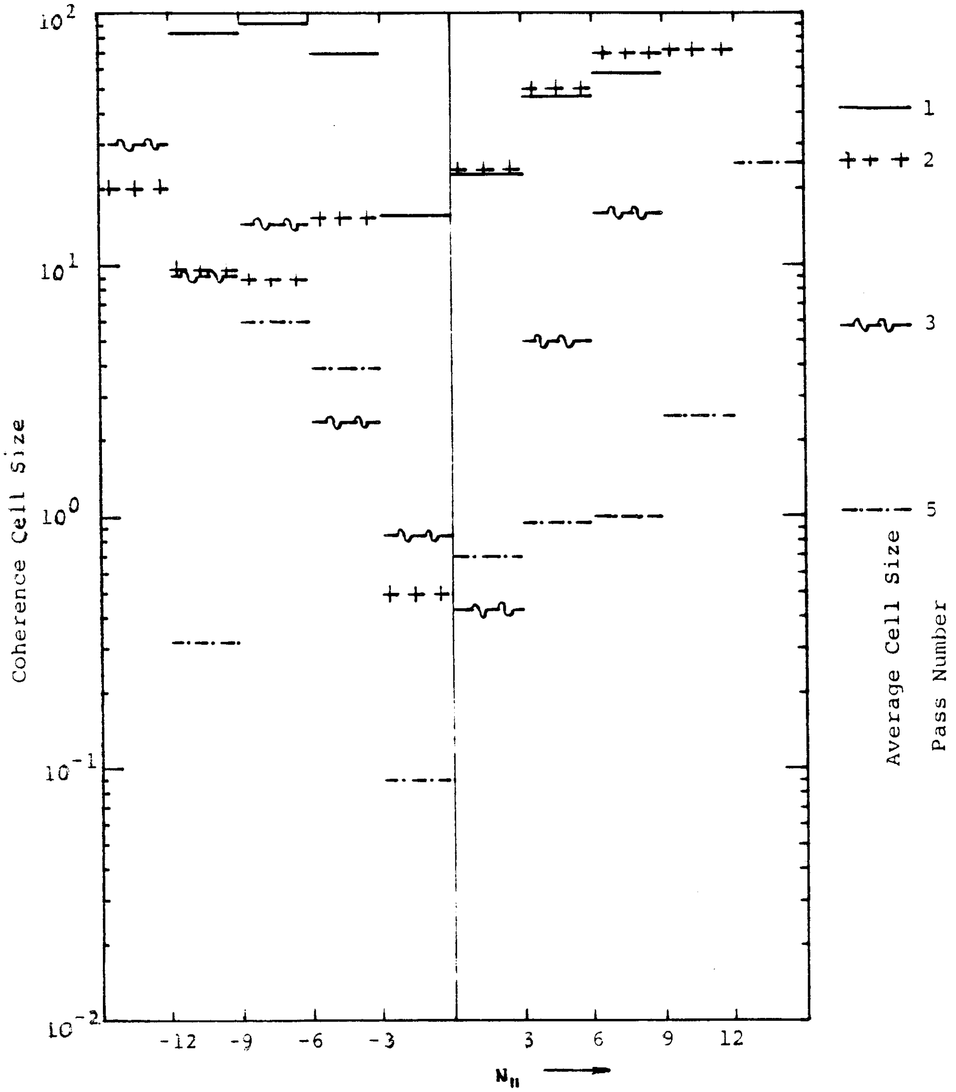

Fig 13.4.7 EVOLUTION OF COHERENCE

For each pass, rays are grouped according to their $N_\parallel$ and the coherence cell size is plotted versus $N_\parallel$. The correspondence between symbol and pass number is shown in the key at the right, which also shows the average cell size for all rays.

appear that lower $N_{\parallel}$ rays are consistently less coherent than higher $N_{\parallel}$, perhaps because longer wavelength waves are more affected by spatial gradients of density and magnetic field.

Fig 13.4.8 shows a radial profile of power for $|N_{\parallel}|$ between 2.5 and 3.5, and orientation within 10° of horizontal.

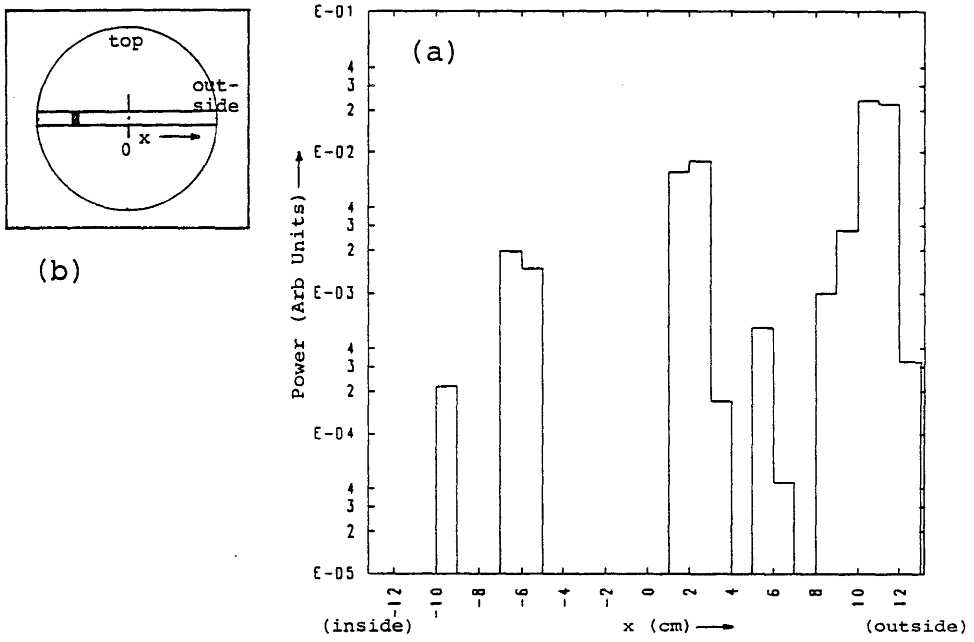

Fig 13.4.8 RADIAL POWER PROFILE

The power density is plotted in (a) across the horizontal chord shown in (b). The plot is restricted to rays with $|N_{\parallel}|$ between 2.5 and 3.5, and with $\vec{k}_{\perp}$ orientations within 10° of the horizontal.

[13.5] Computation Details

The computation proceeds in 5 stages. The output files of each stage serve as the input files of the next stage. The first stage is the computation of the launched wave spectrum (sub-section [13.3]). In the second stage, ray tracing is used to follow a large number of rays and record each passage of each ray across the scattering plane. A 3-D spread of rays is launched, with 2 dimensions for the spatial location and the 3rd dimension for $N_{\|}$. The starting power and phase of each ray are suitably chosen taking into account the ray's spatial location and $N_{\|}$. The rays are traced one by one; each time a ray crosses the scattering plane (45° toroidally from the waveguide grill) an output record is written containing the ray's spatial location, wavevector, power and phase, some starting coordinate tags to identify the ray, and the toroidal pass number. A ray is followed until either (1) it damps to 1% of its initial power, (2) it exceeds 8000 integration steps or (3) it undergoes 20 radial reflections. In practice 84% of the rays terminate due to damping, with most of the rest executing 20 radial reflections. In order to obtain smooth graphs, it is necessary to have several thousand rays. Computation time, however, runs at about 100 rays per minute on a Cray-1. Consequently, the approach taken is to follow about 300 rays directly, and use linear interpolation to expand the ray set. Also, the $N_{\|}$ range is broken into several intervals containing significant power; each interval is run separately. This avoids wasting computer time on $N_{\parallel}$ intervals containing little power. Thus the 3rd stage of the computation is the interpolation to a 'complete' ray set, and the 4th stage is the merge of the output files from the different $N_{\parallel}$ intervals.

The fifth and last stage of computation consists of data analysis and graphics. The graphics program has capabilities for generating radial power profiles, contour maps, $N_{\parallel}$ spectra, plots of wavevector orientation and puncture plots (one dot for each ray crossing the scattering plane). Many of the plots may be done with either $N_{\parallel}$ or $N_{\perp}$ selectivity. Some statistical analysis may also be performed.

Section [14] COMPARISON BETWEEN THEORY AND EXPERIMENT

Results from experiments and from theoretical modelling have been presented in the previous two sections. By and large the gross features are consistent. Both demonstrate the presence of a strong resonance cone at the edge, limited in both the r and θ directions, and less power further in. The power map of Fig 13.4.1 shows a predicted bright region at the center which was determined to be first pass negative $N_{||}$ rays and second pass positive $N_{||}$ rays. The negative $N_{||}$ rays are not seen because their orientation (Fig 14.01) does not match that of the scattering volumes used; the positive $N_{||}$ rays may well be what is seen to reach the center -- the measured amplitude being lower than at the edge at least partly because the available power has a wider orientation spread. The computed radial profile (Fig 13.4.8) is in partial agreement with experiment (Fig 12.2.1): the resonance cone is farther in in the experiment ($r/a=0.65$ as against $r/a=0.8$), and less power is measured at the center. The sharper features of the computed profile are at least partly due to (1) it being a more fine-grained picture (1 cm by 2 cm cell size; much smaller than a scattering volume). Perhaps the most dramatic agreement between theory and experiment is the orientation scan. The experiment (Fig 12.4.1) showed a very narrow spread with a small offset from horizontal; both of these features were matched extremely well by the computation (Fig 13.4.6).

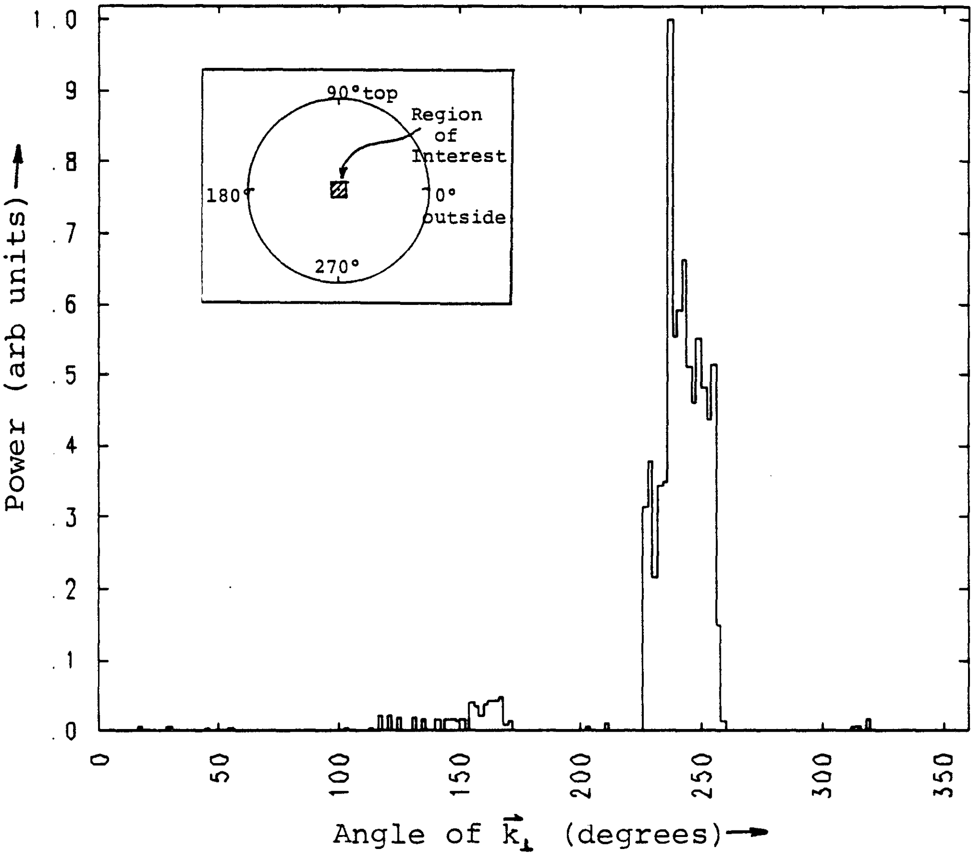

Fig 14.01 ORIENTATION SPECTRUM NEAR CENTER

Plot of power vs orientation angle for the rays passing through the region of interest (shown in the inset).

Another point of agreement between experiment and theory lies in the frequency spectrum of the lower hybrid waves. Andrews and Perkins [Andrews.83] have calculated the spectral broadening of lower hybrid waves in a tokamak due to scattering from low frequency fluctuations, using a radiative transport equation incorporating frequency diffusion. They obtain a formula

$$\Delta\omega \simeq \frac{N_\parallel}{2}\cdot\frac{c}{a}\cdot\frac{\omega_{pe}(r=0)}{\omega_{ce}}\cdot\frac{2T_i(r=a)}{m_e c^2} \times \begin{cases} \sqrt{\tau} & \text{for } \tau \ll 1 \\ \tau & \text{for } \tau \gtrsim 1 \end{cases} \qquad 14.01$$

for the half-width (HWHM) $\Delta\omega$, where $N_\parallel$, c, m_e, ω_{pe}, ω_{ce} and T_i have their usual meanings, a is the tokamak minor radius and τ is the optical depth given by

$$\tau \simeq \frac{2}{N_\parallel}\cdot\frac{\omega_{pe}^2(r=0)}{\omega^2}\left[\frac{m_e c^2}{2T_i}\right]^{\frac{1}{2}}\cdot\frac{c}{\sqrt{\omega_{ce}\omega_{ci}}} \qquad 14.02$$

Using the parameters in Table 14.1, we obtain a value of 110 kHz for the half-width, or 220 kHz FWHM. This agrees

Table 14.1 PLASMA PARAMETERS USED FOR CALCULATING FREQUENCY BROADENING DUE TO SCATTERING OF LOWER HYBRID WAVES FROM LOW FREQUENCY FLUCTUATIONS

Quantity	Symbol	Value
Minor Radius	a	13 cm
Central Density	n_{e0}	$5 \times 10^{12}\,\mathrm{cm}^{-3}$
Edge Ion Temperature	T_{ia}	10 eV
Toroidal Field	B_T	1 T
Wave Frequency	f	0.8 GHz
Parallel Refractive Index	$N_\parallel$	3

as well as one might expect with the experimental value of 400 kHz, considering that (1) edge ion temperature in Versator is not well known, and (2) assumptions in the theory regarding edge conditions and fluctuation level may or may not be valid for Versator plasmas.

We also notice from Figs 13.4.4 and 13.4.5 that the computed $N_{\parallel}$ spectrum at the edge falls off more steeply with increasing $N_{\parallel}$ than the spectrum at the center, which is the same result as obtained in the experiment (Figs 12.3.1 and 12.3.2). However these computed spectra include rays with all possible orientations. Fig 14.02 shows the computed

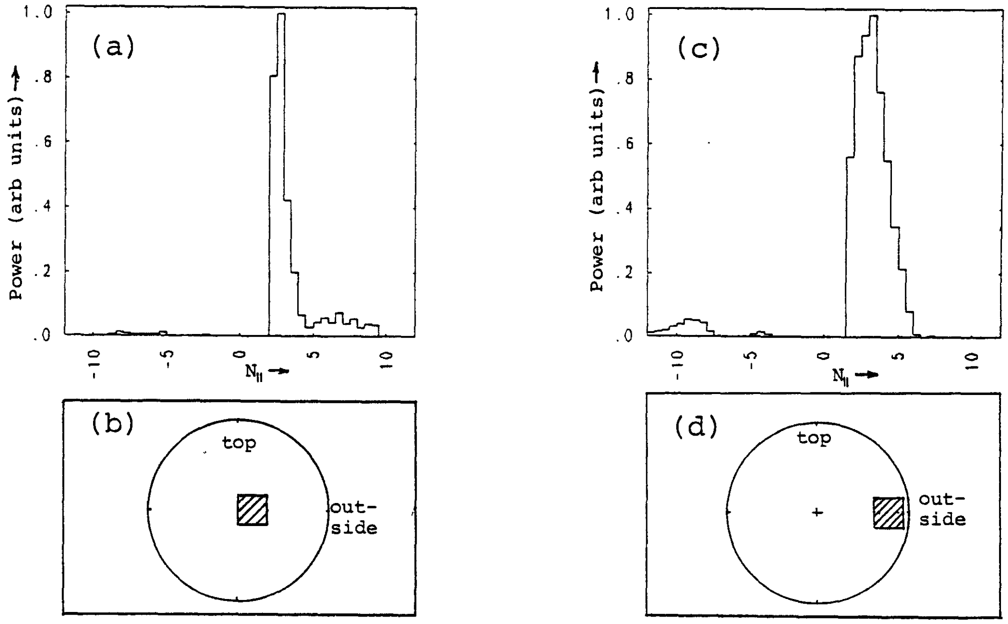

Fig 14.02 COMPARISON OF $N_{\parallel}$ SPECTRA AT CENTER AND EDGE, WITH RESTRICTED ORIENTATIONS

(a) and (c) show the $N_{\parallel}$ spectra of the rays passing through the regions of interest shown in (b) and (d). The plots are restricted to rays with $k_{\perp}$ orientations within 5° of the horizontal.

spectra including only rays with orientations within 5° of the horizontal. It is apparent that the shape of the center spectrum is somewhat altered, and agreement between experiment and theory on this point is tenuous at best.

There are also two notable discrepancies between theory and experiment. First, the measured signals are low by at least one and a half orders of magnitude. Recall that $\hat{I}(N_{\parallel})$ must satisfy Eqn 11.06

$$\boxed{A_W \int \hat{I}(N_{\parallel})\,dN_{\parallel} = 1 \qquad \begin{matrix}14.03\\(11.06)\end{matrix}}$$

As Table 14.2 shows, the beam area may be between 0.03 m^2 (the area of the waveguide grill mouth) and 1.0 m^2 (the area of a magnetic surface). Inspection of Fig 12.3.1 shows that the integral in Eqn 14.03 may evaluate to between 0.03 m^{-2} and 0.1 m^{-2}, depending on how one extrapolates the graph for small $N_{\parallel}$. Thus the product of the two terms is between 10^{-3} and 10^{-1}, not 1. A number of points deserve mention here. First, the lower estimated value is more reasonable for both terms. Second, the right hand side of Eqn 14.03 is not strictly 1. Not all the 0.8 GHz power goes into the

Table 14.2 ESTIMATE OF TERMS IN Eqn 14.03

	A_W	$\int \hat{I}(N_{\parallel})\,dN_{\parallel}$	Product
Min	$3 \times 10^{-2} m^2$	$1 \times 10^{-2} m^{-2}$	3×10^{-4}
Max	$1 \times 10^{0} m^2$	$3 \times 10^{-2} m^{-2}$	3×10^{-2}

detected resonance cone. Imperfect coupling between waveguide and plasma, waveguide transmission losses, and the fact that about 30% of the power is launched in waves with negative $N_{\|}$ are all reasons that the right hand side should be more like 0.5 than 1. Third, the calculation of $\hat{I}(N_{\|})$ required assumptions about the distribution of power flow as a function of orientation. To calculate $\hat{I}(N_{\|})$ (see Section 11) we assumed the power flow to be isotropic for all inward directions, however experiment clearly shows that the orientation distribution is sharply peaked (Fig 12.4.1). The two issues here are (1) is our measured value at the peak of the orientation distribution ? and (2) how wide is the orientation distribution ? The width of the orientation distribution is less than 10°, whereas our isotropic assumption has an effective width of 90°. On the other hand, judging from the offset of the peak in Fig 12.4.1, our measured value may be down a factor of 2 or 3 from the peak value. In sum, however, the true value of $\hat{I}(N_{\|})$ is likely to be lower (by perhaps a factor of 3) than our calculation. There is most definitely a discrepancy between measured signal levels and theory; the best estimate is perhaps 2.5 orders of magnitude.

Assuming for the time being that there is no fundamental mistake in the experiment or analysis, there are a number of possible explanations for the low signal levels; none, however, are particularly convincing. (1) The receiving antenna may not be properly positioned to see the scattered radiation. It is possible that, despite the CW alignment, the scattered radiation is shifted toroidally away from the receiving horn. Some toroidal deflection is anticipated due to the wave's $k_{\parallel}$, however, as shown in Appendix [17.2], $k_{\parallel}$ (typically 0.7 cm^{-1}) is smaller than the resolution $\Delta k_{\parallel}$ (half-width of 0.9 cm^{-1}), so that this cannot account for much signal reduction. Other causes of toroidally shifted scattered power could be a mis-aligned mirror pivot or a tilt of the scattering plane out of the vertical. The $k_{\parallel}$ resolution above corresponds to an angular half-width of 2 and a scattered beam spot size of 3 cm (full-width), so it is hard to see how toroidal misalignment could account for more than one order of magnitude signal reduction. (2) The scattered power may be low due to loss of incident beam power, either due to plasma instability or relativistic cyclotron absorption [Mazzucato.84]. We have, however, used the 2 mm system as an interferometer in similar plasmas, and while the transmitted signal may drop to about 30% of the vacuum value (probably due to refraction), we have never observed worse transmission than this. Loss of beam power is unlikely to be a severe problem. (3) Since scattering is stronger from coherent waves, loss of coherence would appear to be a likely reason for reduced scattered power. Unfortunately Parseval's relation

$$\int \tilde{n}_e^2(\vec{r})\,d\vec{r} = \int \tilde{n}_e^2(\vec{k})\frac{d\vec{k}}{(2\pi)^3} \qquad 14.04$$

shows that loss of coherence redistributes scattered power in $\vec{k}$-space, but does not reduce the integrated measured power. (4) We may not be looking in the right place for the lower hybrid waves. Lower hybrid waves at a spatial point exist with two degrees of freedom: magnitude of the $\vec{k}$-vector and the orientation of $\vec{k}_\perp$, whereas our spectral scan is one-dimensional ($N_\parallel$ from ~3 to ~8, with a single orientation for each $N_\parallel$). Given the narrow measured orientation width and our restricted scan, we may just have missed the strongest waves. But we have been quite generous in our assumptions of $\vec{k}$-space width of the power flow, assuming it to be semi-isotropic in orientation. In order to raise our estimate of total power flow, we would therefore require that substantially more power exists at orientations other than we measured, and this is not likely since the first pass resonance cone appears to have been found satisfactorily. (5) Possibly turbulence destroys the lower hybrid wave structure to the point where much of the power exists at large $k_\parallel$ or $k_\perp$, and so escapes detection, but this is not consistent with the narrow orientation width measured. In summary, while some of the shortfall in scattered power may be explainable, this issue is as yet unresolved.

The second unresolved discrepancy concerns the $N_\parallel$ spectrum for the case of 180° waveguide phasing. The measured edge spectrum for +90° agrees quite well with the computed launched spectrum, but the 180° case is way off (Fig 12.3.5). Briefly, the possiblities are (1) launched spectrum different from calculated, (2) spectrum strongly downshifted on the first pass, (3) systematic experimental bias towards low $N_{\parallel}$. The first possibility could be due to waveguide phasing errors or unequal drive in the 4 waveguides. The waveguide phasing has been checked, also calculation [Luckhardt.85] has shown the launched spectrum to be relatively insensitive to small errors in waveguide phasing. Forward and reflected waveguide powers are monitored; we are not aware of any serious problems. The second possibility, namely strong downshift, is simply not supported by ray-tracing results. And the third possibility, systematic bias towards low $N_{\parallel}$, for whatever reason (broadening due to loss of coherence, for example, or a geometric effect due to the smaller scattering angle and larger scattering volume), cannot explain why there is good agreement for the +90° case.

Section [15] CONCLUSION

A series of experiments has been performed to study the propagation of lower hybrid waves in the current drive regime. Radial profiles and $N_{\parallel}$ spectra have been measured at densities both above and below the current drive density limit. Frequency spectra and orientation spectra have been measured. A power scan has been performed. A spatial scan in the poloidal direction has also been made. A specific phase comparison experiment was performed to look for wave absorption during current drive. In addition, theoretical modelling using a ray tracing code has been done.

We have succeeded in detecting a resonance cone towards the plasma edge, limited in spatial extent both in the radial and poloidal directions. The $\vec{k}_{\perp}$ orientation spectrum was found to be very narrow (less than 10°) and offset from horizontal by about 4°, both of which features were reproduced very well in the computation. Power is found to reach the center of the plasma, though broadening both spatially and in k space makes it difficult to tell how much. (Ray tracing suggests that the central power density is quite high.) Consistently lower power is seen at the center for the +90° waveguide phasing (the current drive case) than for -90°, which may be interpreted as evidence of wave absorption during current drive. $N_{\parallel}$ spectra for the +90° case are exponentially decreasing and fit the computed

Brambilla spectrum quite well. Measured spectra at the center are noticeably flatter than at the edge, although in the outer regions of the plasma the higher $N_{\parallel}$ do not penetrate as well. Unfortunately the $N_{\parallel}$ spectra for the case of 180° waveguide phasing differ markedly from the computed spectrum. The other significant source of disagreement between theory and experiment lies in the absolute level of measured power; the experimental power level is short by about 2 to 3 orders of magnitude, for reasons not well understood. The measured frequency spectrum is consistent with the broadening calculated by Andrews and Perkins due to scattering of lower hybrid waves by density fluctuations.

Regarding this last issue, we note that agreement between ray tracing computation and experiment is reasonable, even though the ray tracing code ignores scattering from low frequency fluctuations. Also the orientation spectrum is very narrow. Thus we conclude that scattering in $\vec{k}$-space is unimportant at these (relatively low) densities.

Comparison of available data between the low and high density cases shows no dramatic differences (neither does the ray tracing computation.) Differences in wave propagation characteristics are therefore unlikely to be the cause of the observed current drive density limit.

The two limitations of our setup that most seriously limited the scope of the measurements were (1) marginal spatial resolution, and (2) incomplete access for scattering geometries.

Regarding potential usefulness of microwave scattering experiments, two comments may be made. Our results indicate that very little symmetry exists in the wave power distribution. Since there are 4 parameters to any measurement (2 spatial degrees of freedom in the poloidal plane and 2 components of $\vec{k}$ in the same plane), any reasonably complete scan over all 4 parameters in order to produce a power map would require a very large set of measurements, even for a single set of plasma parameters. Further there is the frequency spread of the lower hybrid wave power, and also the fact that a power map in one plane may not be indicative of other toroidal locations in the tokamak, so that global power mapping seems if not prohibitive at least very expensive. The second comment is that the microwave scattering experiment measures intensity, or power per unit area, and beam area is not easily measurable.

On the other hand, microwave scattering is a unique tool for probing waves inside the plasma, and a number of interesting and useful measurements can be made. It is hoped that the present work is perceived as a small but useful step in that direction.

REFERENCES

- -

F Alladio et al, in Proc of 9th Intl Conf on Plasma Physics and Controlled Nuclear Fusion Research, Baltimore MD, 1982 (Intl Atomic Energy Agency, Vienna, 1982), paper IAEA-CN-41/I-4.

P L Andrews and F W Perkins, Phys Fluids, 26 (9) 2546 (1983).

G Bekefi, "Radiation Processes in Plasmas", (Wiley, New York, 1966).

S Bernabei et al, Phys Rev Lett, 49 (17) 1255 (1982).

P Bonoli and E Ott, Phys Fluids, 25 (2) 359 (1982).

M Brambilla, Nucl Fusion, 16 (1) 47 (1976).

K-I Chen, private communication (1985).

"CRC Handbook of Chemistry and Physics", (CRC Press, West Palm Beach, FL) 59th edition, pp. E-356,357.

N J Fisch, Phys Rev Lett, 41 (13) 873 (1978).

A S Fisher, PhD thesis, Dept of Physics, MIT (1983).

A R von Hippel, ed., "Dielectric Materials and Applications" (MIT, Cambridge MA) 1st edition, p. 311.

G Ichtchenko et al, Euratom-CEA Report EUR-CEA-FC-1193 (July 1983).

F C Jobes et al, Phys Rev Lett, 52 (12) 1005 (1984).

F C Jobes et al, Phys Rev Lett, 55 (12) 1295 (1985).

C F F Karney et al, Princeton Plasma Physics Lab Report PPPL-2152 (Oct 1984).

S F Knowlton, private communication (1985-b).

S C Luckhardt et al, in Proc of Fourth Topical Conf on RF Heating in Plasma, Austin TX, 1981 (Univ of Texas, Austin TX, 1981) paper B6.

S C Luckhardt et al, Phys Rev Lett, 48 (3) 152 (1982).

S C Luckhardt, private communication (1985).

M J Mayberry et al, in "Radiofrequency Plasma Heating", AIP

Conference Proceedings No. 129, pp 162-165 (1985).

E Mazzucato et al, Bull Am Phys Soc, 29 (8) 1334 (1984).

F S McDermott, PhD thesis, Dept of Physics, MIT (1984).

R Motley et al, in Proc of Tenth Intl Conf on Plasma Physics and Controlled Nuclear Fusion Research, London, 1984 (Intl Atomic Energy Agency, Vienna, 1984), paper IAEA-CN-44/F-II-2.

M Porkolab et al, Phys Rev Lett, 53 (5) 450 (1984-a).

M Porkolab, IEEE Trans Plasma Sci, PS-12 (2) 107 (1984-b).

B Richards et al, Comments Plasma Phys and Controlled Fusion 3 (5) 117 (1978).

B Richards, PhD thesis, Dept of Physics, MIT (1981).

R Rohatgi et al, in "Radiofrequency Plasma Heating", AIP Conference Proceedings No. 129, pp. 174-177 (1985a).

R Rohatgi and P Bonoli, "Numerical Simulation of Lower Hybrid Wave Propagation", Versator internal report, (1985b).

V D Shafranov, in "Reviews of Plasma Physics", ed. M A Leontovich (Consultants Bureau, New York) vol 2, pp. 103-151 (1967).

R E Slusher and C M Surko, Phys Fluids, 23 (3) 472 (1980).

R E Slusher et al, Phys Fluids, 25 (3) 457 (1982).

T H Stix, "The Theory of Plasma Waves", (McGraw-Hill, New York, 1962).

D Stone, PhD thesis, Dept of Physics, MIT (1979).

Y Takase et al, Phys Fluids, 28 (3) 983 (1985-a).

Y Takase et al, in "Radiofrequency Plasma Heating", AIP Conference Proceedings No. 129, pp 186-189 (1985-b).

R L Watterson et al, Phys Fluids, 28 (8) 2622 (1985).

S Weinreb and A R Kerr, IEEE J Solid State Ccts, SC-8 (1) 58 (1973).

T Yamamoto et al, Phys Rev Lett, 45 (9) 716 (1980).

Appendix [17] SCATTERING CALCULATION

The scattering formula derived here relates the scattered power to the density amplitude of the waves responsible for the scattering. The scattering geometry is taken into account. The calculation is similar to that of Bekefi[.66] or Slusher[.80].

[17.1] Main Scattering Calculation

We are interested in a plane electromagnetic wave of frequency $\omega_I >> \omega_{pe}, \omega_{ce}$ incident on a plasma in the O-mode

$$\vec{E} = \vec{E}_o \; f(\vec{r}) \; \cos(\vec{k}_I \cdot \vec{r} - \omega_I t) \qquad 17.1.01$$

where all quantities are real. $\vec{E}_o$ is a constant and $f(\vec{r})$ accounts for the radiation pattern of the transmitting horn. $f(\vec{r})$ is defined so as to have a maximum value of 1 on $|\vec{r}| = R_X$, where R_X is the distance between the transmitting horn and the scattering volume. (The $1/r^2$ variation over the relatively small scattering volume is ignored.) $e^{j(\omega_I t - \vec{k}_I \cdot \vec{r})}$ is more convenient to work with, so write

$$\vec{E}_o f(\vec{r}) \cos(\vec{k}_I \cdot \vec{r} - \omega_I t) = \tfrac{1}{2}\vec{E}_o f(\vec{r}) \; e^{j(\omega_I t - \vec{k}_I \cdot \vec{r})} + \tfrac{1}{2}\vec{E}_o f(\vec{r}) \; e^{-j(\omega_I t - \vec{k}_I \cdot \vec{r})} \qquad 17.1.02$$

Then for the time being consider an incident wave

$$\vec{E}' = \vec{E}_o\ f(\vec{r})\ e^{j(\omega_I t - \vec{k}_I\cdot\vec{r})} \tag{17.1.03}$$

At high frequency the electrons may be treated as single particles and the ions may be ignored. The electrons are accelerated and consequently radiate. The radiation fields may be computed from the Lienard-Wiechert formulae. In the non-relativistic limit, a single electron at $\vec{r}$ generates fields at $\vec{R} = R\,\hat{R}$ in the far field given by

$$\vec{E}'_{S1}(\vec{R},t) = \frac{r_o}{R}\, e^{j(\omega_I t - \vec{k}_I\cdot\vec{r})}\ \hat{R}\times(\hat{R}\times\vec{E}_o)\ f(\vec{r}) \tag{17.1.04}$$

$$\vec{H}'_{S1}(\vec{R},t) = \varepsilon_0 c\ \hat{R}\times\vec{E}'_{S1} \tag{17.1.05}$$

where

$$r_o = \frac{e^2}{4\pi\varepsilon_0 m_e c^2} = 2.82\ \text{fm} \tag{17.1.06}$$

is the classical electron radius and

$$\tau = t - \frac{|\vec{R}-\vec{r}(\tau)|}{c} \tag{17.1.07}$$

is the retarded time. Writing

$$|\vec{R}-\vec{r}(\tau)| \simeq R - \hat{R}\cdot\vec{r}(\tau) \tag{17.1.08}$$

which is good for $k_I \cdot r^2 << R$ and

$$\vec{r}(\tau) \simeq \vec{r}(t-\frac{R}{c}) \tag{17.1.09}$$

which is good for $(v/c)\cdot k_I \cdot r << 1$, we can simplify

$$\omega_I\tau-\vec{k}_I\cdot\vec{r}(\tau) \approx \omega_I t_1 + \vec{k}\cdot\vec{r}(t_1) \tag{17.1.10}$$

where we have defined

$$t_1 = t - \frac{R}{c} \tag{17.1.11}$$

$$\vec{k} = \frac{\omega_S}{c}\hat{R} - \vec{k}_I \tag{17.1.12}$$

(ω_S is the frequency of the scattered wave.) Then

$$\vec{E}'_{S1}(\vec{R},t) = \frac{r_o}{R}\, e^{j(\omega_I t_1-\vec{k}_I\cdot\vec{r}(t_1))}\ \hat{R}\times(\hat{R}\times\hat{E}_o)\ f(\vec{r}) \tag{17.1.13}$$

Because of the receiving antenna's radiation pattern, the radiated fields from the various electrons do not couple equally into the antenna; rather, there is a weight function $g(\vec{r})$ (exactly analogous to $f(\vec{r})$). Then the total scattered electric field coupled into the receiver may be found by summing over electrons

$$\vec{E}'_S(\vec{R},t) = \frac{r_0}{R}\ \hat{R}\times(\hat{R}\times\vec{E}_o)\int d\vec{r}\ \tilde{n}_e(\vec{r},t_1)f(\vec{r})g(\vec{r})e^{j(\omega_I t_1-\vec{k}\cdot\vec{r})} \tag{17.1.14}$$

For our Fourier transform convention

$$A(\vec{r}) = \int\frac{d\vec{k}}{(2\pi)^3}\ A(\vec{k})\ e^{-j\vec{k}\ r} \tag{17.1.15}$$

the convolution formula is readily obtained

$$\int d\vec{r}\ A(\vec{r})B(\vec{r})\ e^{j\vec{k}\cdot\vec{r}} = \frac{d\vec{k}_1}{(2\pi)^3}\ A(\vec{k}_1)B(\vec{k}-\vec{k}_1) \tag{17.1.16}$$

which may be applied to Eqn 17.1.14 to

get

$$\vec{E}'_S(R,t) = \frac{r_o}{R}\hat{R}x(\hat{R}x\vec{E}_o)\int\frac{d\vec{k}_1}{(2\pi)^3}n_e(\vec{k}_1,t_1)C(\vec{k}-\vec{k}_1)e^{j\omega_I t_1} \qquad 17.1.17$$

and the time Fourier transform

$$\vec{E}'_S(\vec{R},\omega) = \frac{r_o}{R}\hat{R}x(\hat{R}x\vec{E}_o)\int\frac{d\vec{k}_1}{(2\pi)^3}\, n_e(\vec{k}_1,\omega-\omega_I)C(\vec{k}-\vec{k}_1) \qquad 17.1.18$$

where

$$\vec{C}(\vec{K}) = \int d\vec{r}\; e^{j\vec{K}\cdot\vec{r}}\; f(\vec{r})\; g(\vec{r}) \qquad 17.1.19$$

But this calculation is for the component of the incident electric field written in Eqn 17.1.03. For the total electric field of Eqn 17.1.02, we obtain

$$\vec{E}_S(\vec{R},\omega) = \frac{r_o}{2R}\hat{R}x(\hat{R}x\vec{E}_o)\int\frac{d\vec{k}_1}{(2\pi)^3}\Big[n_e(\vec{k}_1,\omega-\omega_I)C(\vec{k}-\vec{k}_1)$$
$$+\, n_e(\vec{k}_1,\omega+\omega_I)C(-\vec{k}-\vec{k}_1)\Big] \qquad 17.1.20$$

$$\vec{H}_S(\vec{R},\omega) = -\frac{\varepsilon_0 c}{2}\hat{R}x\vec{E}_o\int\frac{d\vec{k}_2}{(2\pi)^3}\Big[n_e(\vec{k}_2,\omega-\omega_I)C(\vec{k}-\vec{k}_2)$$
$$+\, n_e(\vec{k}_2,\omega+\omega_I)C(-\vec{k}-\vec{k}_2) \qquad 17.1.21$$

Define a spectral intensity $\psi(\omega)$ by

$$P = A_R\int_0^\infty\frac{d\omega}{2\pi}\,\psi(\omega) \qquad 17.1.22$$

where P is the total power seen by a receiver of effective area A_R. We have for $\psi(\omega)$

$$\psi(\omega) = \frac{2}{T}\,\mathrm{Re}\,\vec{E}(\omega)\times\vec{H}^{*}(\omega) \tag{17.1.23}$$

where T is the time interval over which the receiver measures power; the scattered fields are assumed to be zero outside this interval. Putting 17.1.20-21 into 17.1.23,

$$\psi(\omega) = \mathrm{Re}\frac{\varepsilon_0 c}{2T}\left|R\times E_0\right|^2\int\frac{d\vec{k}_1}{(2\pi)^3}\int\frac{d\vec{k}_2}{(2\pi)^3}\left\langle\left|n_e(\vec{k}_1,\omega-\omega_I)\,n_e^{*}(\vec{k}_2,\omega-\omega_I)\right|\right\rangle$$

$$\times\ C(\vec{k}-\vec{k}_1)\,C^{*}(\vec{k}-\vec{k}_2) \tag{17.1.24}$$

where the cross-terms and $\omega+\omega_I$ terms have been dropped because 1) $n_e(k,\tilde{\omega})$ is non-zero only over a narrow bandwidth at $\tilde{\omega} \ll \omega_I$; 2) $\omega_I > 0$; 3) only $\omega > 0$ is of interest (see Eqn 17.1.22). Now the expectation value in <brackets> is non-zero only if 1) $\vec{k}_1 = \vec{k}_2$ and 2) $\vec{k}_1$ satisfies the dispersion relation, which we shall denote by

$$k_{\parallel} = H(k_{\perp}) \tag{17.1.25}$$

in terms of the components of $\vec{k}$

$$\vec{k} = k_{\parallel}\hat{z} + \vec{k}_{\perp} \tag{17.1.26}$$

$$\vec{k}_1 = k_{1\parallel}\hat{z} + \vec{k}_{1\perp} \tag{17.1.27}$$

Then we may write

$$\left\langle\left|n_e(\vec{k}_1,\omega-\omega_I)\,n_e^{*}(\vec{k}_2,\omega-\omega_I)\right|\right\rangle = \left\langle\left|n^2(\vec{k}_{1\perp},\omega-\omega_I)\right|\right\rangle\,\delta(\vec{k}_2-\vec{k}_1)$$

$$\times\ \delta(k_{1\parallel}-H(k_{1\perp})) \tag{17.1.28}$$

The dimensions of the bracketed term on the RHS are $L^{-4}T^{2}$. Introduce the incident Poynting flux

$$S_I = \frac{1}{2}\varepsilon_0 c\, E_o^2 \tag{17.1.29}$$

and use for our geometry

$$\left|\hat{R}\times\vec{E}_o\right|^2 = E_o^2 \tag{17.1.30}$$

to obtain

$$\psi(\omega) = \mathrm{Re}\,\frac{S_I}{T}\left(\frac{r_o}{R}\right)^2 \frac{1}{(2\pi)^6}\int dk_{1\parallel}\, d\vec{k}_{1\perp} \langle |n^2(\vec{k}_{1\perp},\omega-\omega_I)|\rangle C^2(\vec{k}-\vec{k}_1)$$
$$\times\ \delta(k_{1\parallel}-H(k_{1\perp})) \tag{17.1.31}$$

We shall see that C is relatively broad in the $k_\parallel$ direction and relatively narrow in the $\vec{k}_\perp$ directions. Using $k_{1\parallel} \cong k_\parallel = 0$ and $\tilde{n}_e(\vec{k}_{1\perp}) \cong \tilde{n}_e(\vec{k}_\perp)$ we obtain finally

$$\psi(\omega) = S_I\left(\frac{r_o}{R}\right)^2 \frac{J}{(2\pi)^6}\,\frac{\langle |n^2(\vec{k}_\perp,\omega-\omega_I)|\rangle}{T} \tag{17.1.32}$$

where

$$J = \int d\vec{k}_{1\perp}\; C^2(\vec{k}_\perp-\vec{k}_{1\perp}) \tag{17.1.33}$$

is computed below.

[17.2] $\vec{k}$-Resolution of the Scattering Volume

In this section we will compute the Fourier transform $C(\vec{K})$ of the overlap of the incident and scattered beams' radiation patterns. It is clear from Eqn 17.1.31 how this quantity relates to the $\vec{k}$-resolution of the scattering geometry. The integral J (Eqn 17.1.33) will also be calculated.

Define non-orthogonal coordinates (Fig 17.2.1) in the scattering plane x_I and x_S along the incident and scattered beams respectively, with scattering angle θ_S. Assuming Gaussian beams, we can write the gain functions $f(\vec{r})$ and $g(\vec{r})$ for the transmitting and receiving horns respectively:

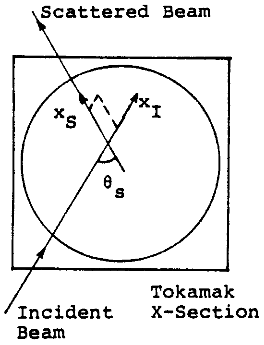

Fig 17.2.1 NON-ORTHOGONAL COORDINATES IN SCATTERING PLANE

$$f(\vec{r}) = \exp[-(zb)^2]\ \exp[-(x_S d)^2] \qquad 17.2.01$$

$$g(\vec{r}) = \exp[-(za)^2]\ \exp[-(x_I c)^2] \qquad 17.2.02$$

where

$$a = \frac{\sqrt{\ln 2}}{R_R \theta_{RE}} \qquad c = \frac{\sqrt{\ln 2}\ \sin\theta_S}{R_R\ \theta_{RH}}$$

$$b = \frac{\sqrt{\ln 2}}{R_X \theta_{XE}} \qquad d = \frac{\sqrt{\ln 2}\ \sin\theta_S}{R_X\ \theta_{XH}} \qquad 17.2.03\text{-}06$$

R_R is the distance from the nominal center of the scattering volume to the receiving antenna, θ_{RE} and θ_{RH} are the 3 dB angular half-widths of the receiving antenna, and the suffix $_X$ denotes the same quantities for the transmitting antenna. Measured values (Appendix [19.3]) are used.

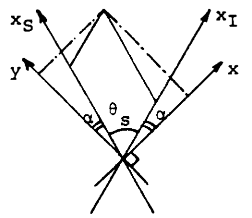

Fig 17.2.2 INTRODUCTION OF ORTHOGONAL CO-ORDINATES IN SCATTERING PLANE

Define orthogonal coordinates x,y, as

shown in Fig 17.2.2, with

$$\alpha = \frac{\pi}{4} - \frac{\theta_S}{2} \qquad 17.2.07$$

The transformation matrix is

$$\begin{pmatrix} x_I \\ x_S \end{pmatrix} = \frac{1}{\sin\,\theta_S} \begin{pmatrix} \cos\,\alpha & -\sin\,\alpha \\ -\sin\,\alpha & \cos\,\alpha \end{pmatrix} \begin{pmatrix} x \\ y \end{pmatrix} \qquad 17.2.08$$

With introduction of orthogonal coordinates, evaluation of $C(\vec{K})$ (Eqn 17.1.19) is straightforward; we get

$$C(\vec{K}) = \frac{\pi^{3/2}}{ABCX} \exp\left[-\frac{K_z^2}{4A^2} - \frac{K_x^2}{4B^2X^2} - \frac{K_y^2}{4C_{,}^2X^2} - \frac{K_xK_yD}{4B^2C_{,}^2X^2} \right] \qquad 17.2.09$$

where

$$A = \left[\ln 2 \left(\frac{1}{R_X^2\theta_{XE}^2} + \frac{1}{R_R^2\theta_{RE}^2} \right) \right]^{1/2} \qquad 17.2.10$$

$$B = \left[\ln 2 \left(\frac{\cos^2\alpha}{R_R^2\theta_{RH}^2} + \frac{\sin^2\alpha}{R_X^2\theta_{XH}^2} \right) \right]^{1/2} \qquad 17.2.11$$

$$C_{,} = \left[\ln 2 \left(\frac{\sin^2\alpha}{R_R^2\theta_{RH}^2} + \frac{\cos^2\alpha}{R_X^2\theta_{XH}^2} \right) \right]^{1/2} \qquad 17.2.12$$

$$D = \ln 2 \left(\frac{1}{R_X^2\theta_{XH}^2} + \frac{1}{R_R^2\theta_{RH}^2} \right) \cos\,\theta_S \qquad 17.2.13$$

$$X = \sqrt{1 - D^2/(4B^2C^2)} \qquad 17.2.14$$

This function has elliptical contours in the poloidal plane.

Calculate the k-resolution terms

$$\Delta k_{\parallel} = \frac{1}{C^2(\vec{K}=\vec{0})} \int dK_{\parallel}\; C^2(\vec{K}_{\perp}=0) \;=\; \sqrt{2\pi}\, A \qquad 17.2.15$$

$$\Delta k_{\perp} = \frac{1}{C^2(\vec{K}=\vec{0})} \int d\vec{K}_{\perp}\; C^2(K_{\parallel}=0) \;=\; 2\pi B C_{,} X \qquad 17.2.16$$

and then J (Eqn 17.1.33)

$$J = \frac{8\pi^6}{(\Delta k_\parallel)^2 \Delta k_\perp} \qquad 17.2.17$$

To get a feel for these quantities, we put in typical parameters for our experiment: $R_R = R_X = 0.4$ m, $\theta_S = 20°$ and beams' FWHM ˜ 4.5°. We obtain a parallel resolution $\Delta k_\parallel = 1.87 \text{ cm}^{-1}$ (FWHM) which is large compared to $k_\parallel$ for lower-hybrid waves in our experiment, typically $\doteq 0.7 \text{ cm}^{-1}$. This means that we need not worry about locating the receiving antenna at the correct $k_\parallel$ orientation. As long as the system is aligned ($k_\parallel = 0$), the lower hybrid waves will be detected.

In the poloidal plane Δk varies between 0.33 cm^{-1} and 1.85 cm^{-1} (the extreme values lie along $\hat{x} \pm \hat{y}$), which is consistently smaller than $k_\perp \cong 10 \text{ cm}^{-1}$ of the waves we seek to detect. This means that the receiver really is looking at a narrow spread of wavenumbers $k_\perp$. Further we note that for scattering angles $\theta_S < 90°$, which is usually the case, the $k_\perp$ spread (see Fig 17.2.3) is mostly in wavenumber and not in orientation.

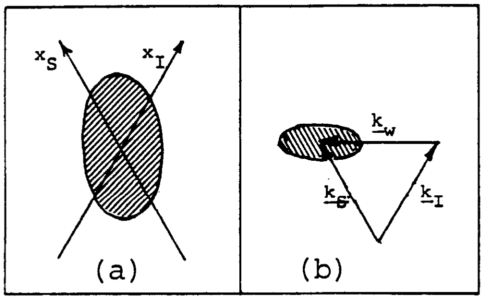

(a) (b)

Fig 17.2.3 $\vec{k}$-RESOLUTION OF SCATTERING VOLUME

The spatial extent of a typical scattering volume is shown in (a). (b) shows the corresponding spread in $\vec{k}_W$.

Appendix [18] LOWER HYBRID WAVE CALCULATION

The quantity of interest in our experiment is the lower hybrid wave power. In Appendix [17] the scattered power was related to the density amplitude of the lower hybrid waves. In this section, the density amplitude will be related to the lower hybrid wave power.

[18.1] Single Wave Analysis
[18.2] Total Wave Power

[18.1] Single Wave Analysis

The starting point for this calculation is the set of equations comprising Maxwell's equations and the collisionless cold plasma fluid equations linearized for a wave with $\exp(j\omega t - j\vec{k}\cdot\vec{r})$ dependence

$$j\omega n_1 - j\vec{k}\cdot n_0\vec{v}_1 = 0 \tag{18.1.01}$$

$$jm\omega\vec{v}_1 = n_0 q\,(\vec{E}_1 + \vec{v}_1\times\vec{B}) \tag{18.1.02}$$

Use a slab model plasma with magnetic field $\vec{B} = B\,\hat{z}$ and wavevector $\vec{k}$ with component $k_y = 0$. The cold plasma electromagnetic tensor relation is obtained

$$\begin{pmatrix} S-N_\parallel^2 & jD & N_\parallel N_\perp \\ -jD & S-N_\parallel^2-N_\perp^2 & 0 \\ N_\parallel N_\perp & 0 & P-N_\perp^2 \end{pmatrix} \begin{pmatrix} E_x \\ E_y \\ E_z \end{pmatrix} = \vec{0} \tag{18.1.03}$$

where $N_\parallel$, $N_\perp$ are components of the refractive index $\vec{N} = c\,\vec{k}\,/\,\omega$. P, S and D are in the standard notation of

Stix[.62]. In the lower hybrid regime

$$\omega_{ci}^2 << \omega_{pi}^2 \gtrsim \omega^2 << \omega_{pe}^2, \omega_{ce}^2 \tag{18.1.04}$$

they may be approximated

$$P \simeq -\omega_{pe}^2/\omega^2 \tag{18.1.05}$$

$$S \simeq 1 + \omega_{pe}^2/\omega_{ce}^2 - \omega_{pi}^2/\omega^2 \tag{18.1.06}$$

$$D \simeq \omega_{pe}^2/\omega\omega_{ce} \tag{18.1.07}$$

The dispersion relation is obtained by setting the determinant of the matrix in Eqn 18.1.03 to zero

$$aN_\perp^4 - bN_\perp^2 + c = 0 \tag{18.1.08}$$

where

$$a = S \tag{18.1.09}$$

$$b = -(P+S)N_\parallel^2 + PS + S^2 - D^2 \tag{18.1.10}$$

$$c = P(S^2-D^2) - 2PSN_\parallel^2 + PN_\parallel^4 \tag{18.1.11}$$

This equation can be solved for $N_\perp$ given $N_\parallel$, ω and the local plasma parameters. Once $N_\perp$ is known, we can solve the fluid equations to obtain

$$n_{1e} = \frac{in_o}{cB} E_x F_2 \tag{18.1.12}$$

$$F_2 = \frac{\omega}{\omega_{ce}} \cdot \frac{N_\perp^2 - P}{N_\perp} - \frac{\omega_{ce}}{\omega} \cdot \frac{N_\perp N_\parallel^2}{N_\perp^2 - P} \tag{18.1.13}$$

To compute the wave power, we need the components of $\vec{E}$ and $\vec{B}$ in terms of E_x. The components of $\vec{E}$ are easily obtained from Eqn 18.1.03 and those of $\vec{B}$ from

$$\vec{B}_1 = \frac{1}{c}\vec{N}\times\vec{E}_1 \qquad 18.1.14$$

Then for a single wave we obtain the Poynting flux

$$\vec{S} = \frac{2}{\mu_0}\mathrm{Re}\ \vec{E}\times\vec{B}^* + 2\varepsilon_0\omega\sum_{ij}E_i\cdot\frac{\partial K_{ij}}{\partial\vec{k}}\cdot E_j^* \qquad 18.1.15$$

$$= -\hat{x}\ 2\varepsilon_0 c\left|E_x^2\right|F_3 + \hat{z}S_z \qquad 18.1.16$$

$$F_3 = -\frac{D^2}{N_\perp^3} - \frac{PN_\perp N_\parallel^2}{(N_\perp^2-P)^2} \qquad 18.1.17$$

This power flux has been computed for a cold non-drifting plasma, for which the 2nd term in Eqn 18.1.15 does not contribute. The thermal and electron drift corrections have been estimated. For typical Versator parameters the dominant correction is the drift contribution to the $\vec{E}\times\vec{B}$ term, <10%. All other corrections are at the <1% level.

[18.2] Total Wave Power

For a spectrum of waves, the component of the Poynting flux in the $\hat{e}$ direction, measured over a time T is

$$S_e = \frac{\hat{e}}{T}\int\frac{1}{\mu_0}\vec{E}(\vec{r},t)\times\vec{B}(\vec{r},t)\ dt \qquad 18.2.01$$

Introducing the Fourier transforms, we have

$$S_e = \frac{2}{\mu_0 T}\mathrm{Re}\frac{\hat{e}\cdot}{(2\pi)^3}\int_0^\infty\frac{d\omega}{2\pi}\int\frac{d\vec{k}_1 d\vec{k}}{(2\pi)^3}\left\langle\vec{E}(\vec{k},\omega)\times\vec{B}^*(\vec{k},\omega)\right\rangle e^{j(\vec{k}-\vec{k}_1)\cdot\vec{r}} \qquad 18.2.02$$

Use the following

(1) $\hat{e} = -\hat{r}$, we are intrested in radial power flow

(2) let α be the angle between $-\hat{r}$ and $\vec{k}_\perp$

(3) the expectation value in <brackets> is non-zero only for $\vec{k} = \vec{k}_1$

(4) as in Appendix [18.1], $\vec{E} \times \vec{B}^* = -\frac{\vec{k}_\perp}{k}|E_x|^2 F_3$

to obtain

$$S_e = \frac{2\varepsilon_0 c}{T}\,\frac{F_3\cos\alpha}{(2\pi)^3}\,\mathrm{Re}\int_0^{2\pi}\frac{d\omega}{2\pi}\int\frac{d\vec{k}}{(2\pi)^3}d\vec{k}_1\left\langle|E_x(\vec{k}\;\;,\omega)|^2\right\rangle\delta(\vec{k}-\vec{k}_1) \qquad 18.2.03$$

Now only waves satisfying the dispersion relation exist, so that we can write

$$\left\langle|E_x(k,\omega)|^2\right\rangle = \left\langle|E_x^2(\vec{k}_\perp,\omega)|\right\rangle\delta(k_\parallel - H(\vec{k}_\perp)) \qquad 18.2.04$$

where the quantity on the RHS is exactly analogous to $\left\langle|n_x^2(\vec{k}_\perp,\omega)|\right\rangle$ defined in Eqn 17.1.28. In fact

$$\left\langle|E_x^2(\vec{k}_\perp,\omega)|\right\rangle = \left(\frac{c\;B}{n_0F_2}\right)^2\left\langle|n_e^2(\vec{k}_\perp,\omega)|\right\rangle \qquad 18.2.05$$

Then

$$S_e = \frac{2\varepsilon_0\,c}{(2\pi)^3}\,\frac{c\;B}{n_0F_2}^{\,2}F_3\int_0^\infty\frac{d\omega}{2\pi}\int\frac{d\vec{k}}{(2\pi)^3}\cos\alpha\,\frac{\left\langle|n_e^2(\vec{k}_\perp,\omega)|\right\rangle}{T} \qquad 18.2.06$$

$\frac{1}{T}\left\langle|n_e^2(\vec{k}_\perp,\omega)|\right\rangle$ may be related to the scattering intensity $\psi(\omega)$ via Eqn 17.1.32. Write $d\vec{k}_\perp = k_\perp\,dk_\perp\,d\alpha$ and use

$$dk_\perp = (dk_\perp/dk_\parallel)\frac{\omega}{c}\,dN_\parallel \qquad 18.2.07$$

to obtain

$$S_e = \frac{2\varepsilon_0 c}{(2\pi)^5}\left[\left(\frac{c\ B}{n_0 F_2}\right)^2 F_3\right]\int_0^{2\pi}\frac{\cos\alpha\ d\alpha}{2\pi}\int_0^{\infty}\frac{\omega d\omega}{2\pi c} \times \int_{-\infty}^{\infty} dN_{\parallel}\, k_{\perp}\frac{dk_{\perp}}{dk_{\parallel}}\,\frac{\left\langle\left|n_e^2(\vec{k}_{\perp},\omega)\right|\right\rangle}{T} \qquad 18.2.08$$

Ideally one would measure the scattered power, and thus $\frac{1}{T}\left\langle\left|n_e^2(\vec{k}_{\perp},\omega)\right|\right\rangle$ for many values of ω, α, and $N_{\parallel}$, and then use Eqn 18.2.08 to calculate the total power. In practice this is not feasible, and if an estimate of total power flux is desired, some modelling may be necessary.

Appendix [19] MICROWAVE MEASUREMENTS

[19.1] Outline

In this appendix four different microwave measurements are presented, all of which are necessary for calibration of our experiment. The measurement of mixer noise temperature and conversion loss is presented in [19.2]. Antenna radiation pattern measurements are presented in [19.3]. The CW calibration of the transmission system is discussed in [19.4]. And lastly, in [19.5] the preamplifier gain maeasurement is discussed.

[19.1] Outline
[19.2] Mixer Measurements
[19.3] Antenna Patterns
[19.4] Transmission System
[19.5] Preamplifier Gain

[19.2] Mixer Measurements

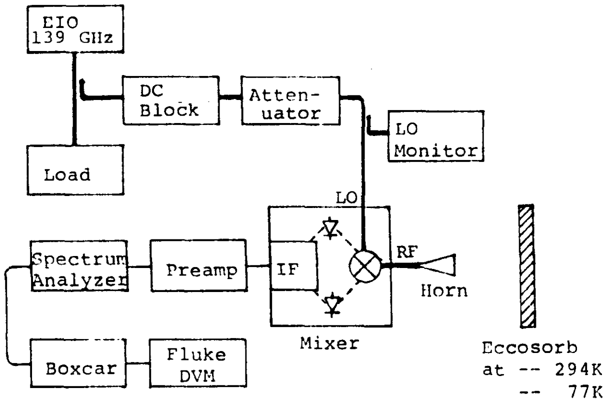

Fig 19.2.1 MIXER TEST SETUP

The mixer was calibrated using the hot and cold load technique. The setup is shown in Fig 19.2.1. A tap off the EIO was used to provide the local oscillator power (measured by a biased Schottky diode detector

[Alpha/TRG F965D]) to the Alpha/TRG F9100 mixer. A blackbody noise source for the RF input was simulated by mounting a gain standard horn on the RF input and putting a piece of Eccosorb foam in front of it. A piece of Eccosorb foam dipped in liquid nitrogen served as a 77 K noise source [Weinreb.73]; it stayed cold long enough to measure the noise power. Another piece of the same material served as a room temperature noise source. The noise power output of the mixer was amplified by its attached MITEQ preamplifier (gain 36 dB, see [19.5] below) and detected by a spectrum analyzer. The measured noise power P in a bandwidth B is given by

$$P = \frac{G}{L} k(T_R+2T_N) B \qquad 19.2.1$$

where T_R is the receiver noise temperature, T_N is the temperature of the RF input signal (blackbody noise), L is the conversion loss, G is the preamplifier gain and k is Boltzmann's constant. The factor of 2 arises because the receiver detects both IF sidebands (at +/- 0.8 GHz). By making power measurements at two different temperatures, we have two equations in two unknowns (namely T_R and L) which are easily solved. (Notice that T_R may be thus determined even if G is not known.) In practice T_R is much higher than room temperature, so that the change in noise power between 77 K and room temperature is quite small. However, very precise measurement of P turns out not to be necessary if the difference in power can be reasonably measured. In fact

$$T_R = \frac{2P_1(T_{N2}-T_{N1})}{P_2-P_1} - 2T_{N1} \qquad 19.2.2$$

where subscripts 1,2 denote the measurements at two different noise source temperatures.

With our setup P_1 was measured directly off the spectrum analyzer scope display, and the difference $P_2 - P_1$ was measured by looking at the scope's vertical signal out with a digital voltmeter, with the help of a boxcar integrator in between to filter the signal and compensate its DC level. The experimental results for noise temperature and conversion loss as a function of LO power are shown in Figs 19.2.2 and 19.2.3 respectively. A noise temperature of 6600 K is obtained with less than 2 mW of LO drive.

Similar results were obtained in another experiment where the noise power was measured with broadband diode detectors (Hewlett Packard 423A) instead of a spectrum analyzer. A third experiment using a spectrum analyzer and a different preamplifier (Watkins Johnson 269) was performed to measure mixer characteristics at an IF of 2.45 GHz. Results obtained were substantially worse than at 0.8 GHz; these are also shown Figs 19.2.2 and 19.2.3. As a result it was not possible to use this mixer to detect lower-hybrid waves launched by our 2.45 GHz S-Band system. Also, a number of auxiliary measurements were performed to calibrate our directional couplers, attenuators, and 139 GHz diode

Fig 19.2.2 MIXER NOISE TEMPERATURE

Noise temperature is shown as a function of L.O. power for both 0.8 GHz and 2.45 GHz intermediate frequencies.

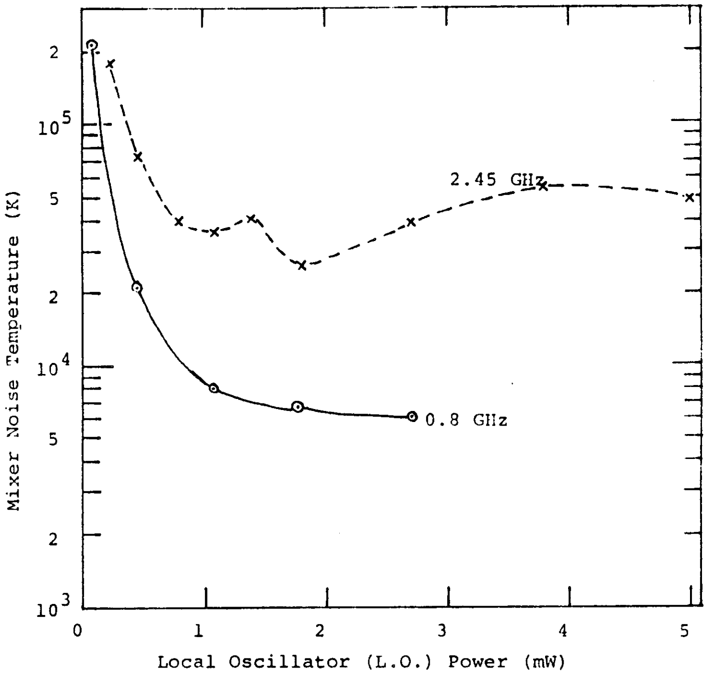

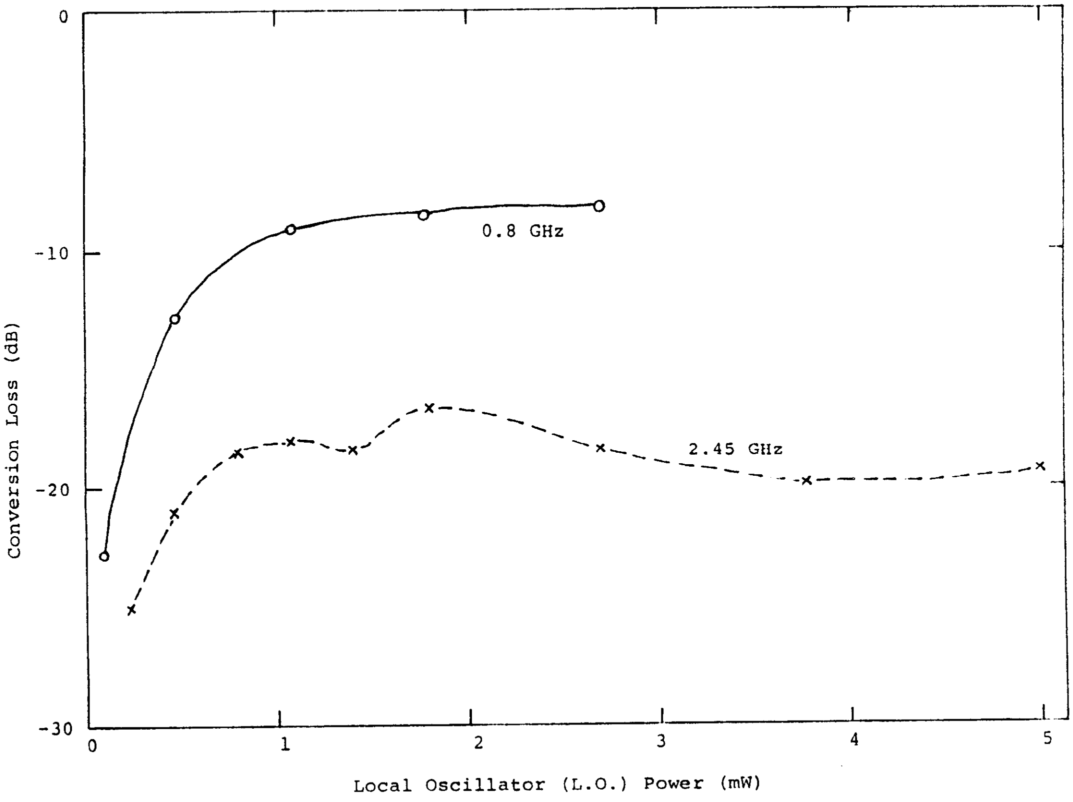

Fig 19.2.3 MIXER CONVERSION LOSS

Conversion loss is shown as a function of L.O. power for both 0.8 GHz and 2.45 GHz intermediate frequencies.

detectors. A Hughes thermistor (Model 45777H) for a Hewlett Packard 432A power meter was used as a reference for these measurements.

[19.3] Antenna Patterns

The setup used to measure antenna radiation patterns is shown in Fig 19.3.1. The EIO power was beamed out horizontally from the test antenna. The beam pattern was determined directly by measuring power across a vertical plane approximately normal to the direction of propagation at a distance of about one meter. The receiver used was an open-ended waveguide with a diode detector, which is suitable for this purpose because of its broad radiation pattern. To improve coupling of plane wave power into the receiver, the edges of the open-ended waveguide were

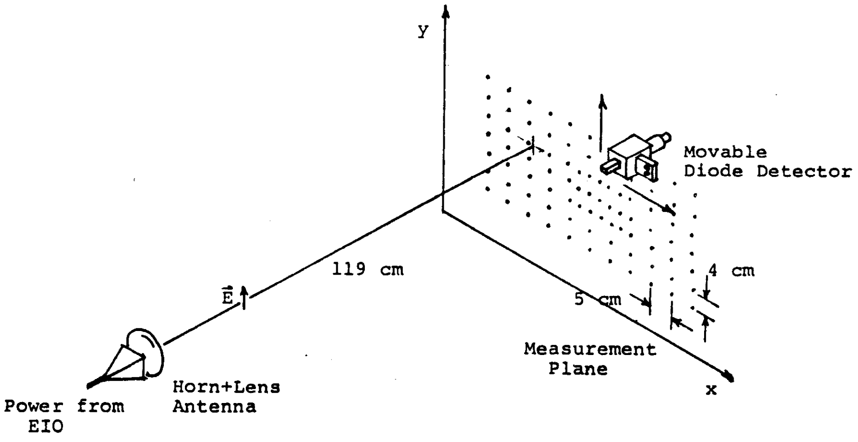

Fig 19.3.1 SETUP FOR ANTENNA PATTERN MEASUREMENT

The dots in the measurement plane correspond to the points at which measurement was made.

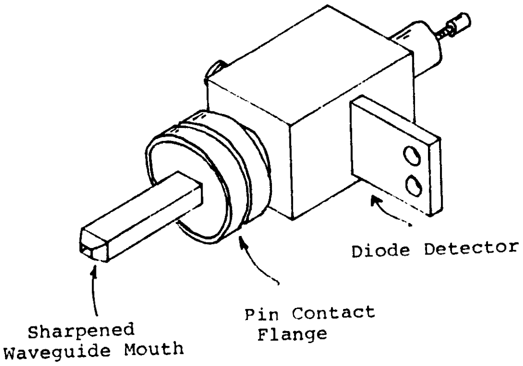

Fig 19.3.2
DETAIL OF DETECTOR

sharpened. The detail is shown in Fig 19.3.2. The dynamic range of this setup was about 25 dB. Measurements were made on a rectangular lattice with point-to-point spacing varying between 2 and 4 cm. Contours were plotted with the aid of an unsophisticated computer program. Results of a sample measurement are shown in Fig 19.3.3. From this measurement, the 3 dB FWHM of the horn and lens configuration was found to be approximately 5° in both planes.

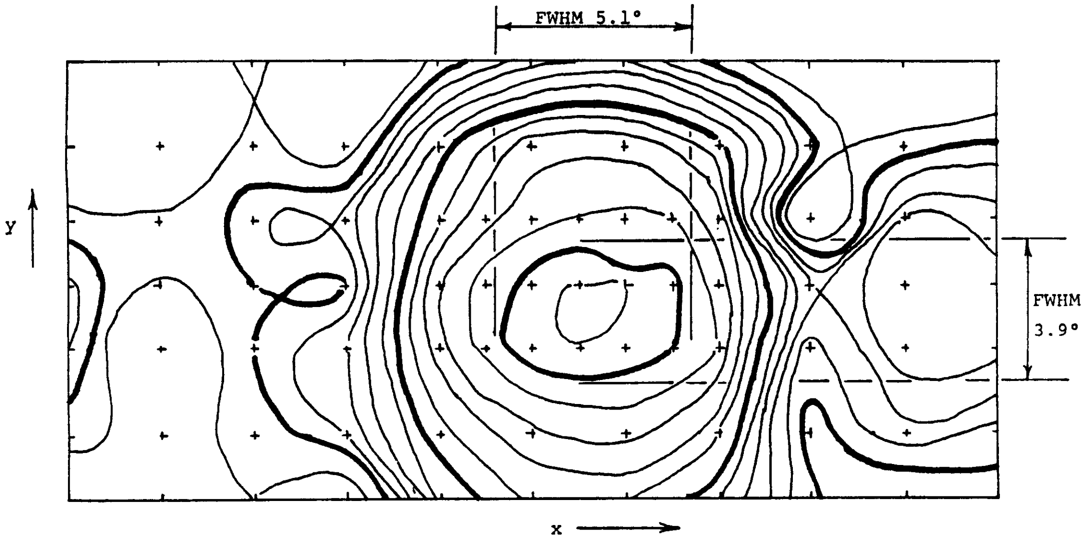

Fig 19.3.3 SAMPLE HORN PATTERN

Radiation pattern for setup of Fig 19.3.1. Contour lines are plotted at 2 dB intervals, with darker lines every 10 dB.

[19.4] Transmission System

To analyze the measured scattered power, we need to know (1) the transmission loss C_L in the receiving line, (2) the Poynting flux S_I in the incident beam (at the scattering volume) and (3) the effective area A_R of the receiving antenna. When the system is aligned, a single measurement of the maximum CW power as shown in Fig 19.4.1 yields the quantity $P_C = S_R A_R C_L$, where S_R is the Poynting flux at the receiving antenna. Defining R_X and R_R as the distances from the scattering volume to the transmitting antenna and to the receiving antenna respectively, we can write

$$S_R = S_I \, \frac{R_X}{R_X+R_R}^{2} \qquad 19.4.1$$

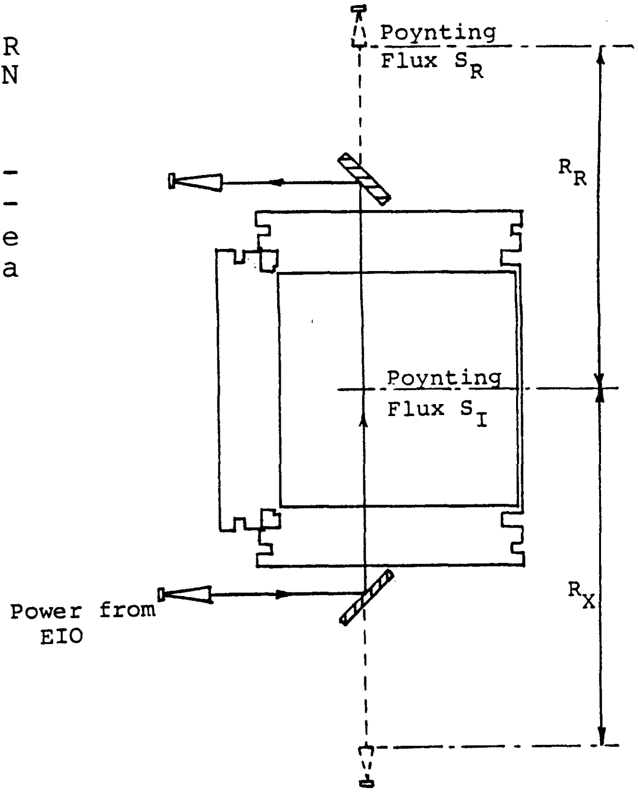

Fig 19.4.1 GEOMETRY FOR CW POWER TRANSMISSION MEASUREMENT

S_I and S_R are the Poynting flux at the scattering volume and at the receiving antenna respectively.

so that $S_I \, A_R \, C_L$, which is the required quantity, is easily determined. In one such calibration experiment, P_C was found to be 19.3 mW, measured with a calibrated directional coupler and a calibrated diode detector. An assumption involved in this technique is that plasma refraction does not significantly change the Poynting flux. Our estimate is that beam broadening due to refraction causes the Poynting flux to drop by less than 20%, a relatively small systematic error in this experiment.

[19.5] Preamplifier Gain

The preamplifier gain was measured using a low-power 0.8 GHz source from the RF system and a calibrated spectrum analyzer. The gain was measured to be 36 dB. Owing to the battery supply used, the sensitivity of the gain to the supply voltage was also checked. The gain dropped 4 dB upon lowering the supply voltage from 15 V to 11 V, and 10 dB from 15 V to 8 V. The gain change was negligible between 15 V and about 13.5 V.

Appendix [20] HIGH VOLTAGE FILTER FEEDTHROUGHS

This appendix describes the development of high voltage filter feedthroughs for the EIO power lines. These devices are easy to make and perform very well.

RF-tight high voltage feedthroughs (10 kV) are necessary to provide high voltage power to the EIO inside the experiment's shielded cabinet. The option of including the power supplies within the shielded volume is impracticable in view of the size of the power supplies; they occupy two full-size racks. RF at 0.8 GHz must be kept out, either by attenuation or by filtering. [At the time this issue was tackled, the possibility of doing an experiment with 2.45 GHz lower-hybrid waves was also a consideration.]

Several options are available. The old scheme [Richards.81] consists of a wire with series inductors and ferrite chokes running down the center of a copper tube [Fig 20.1]. The interspace is filled with a cement + graphite dust mixture.

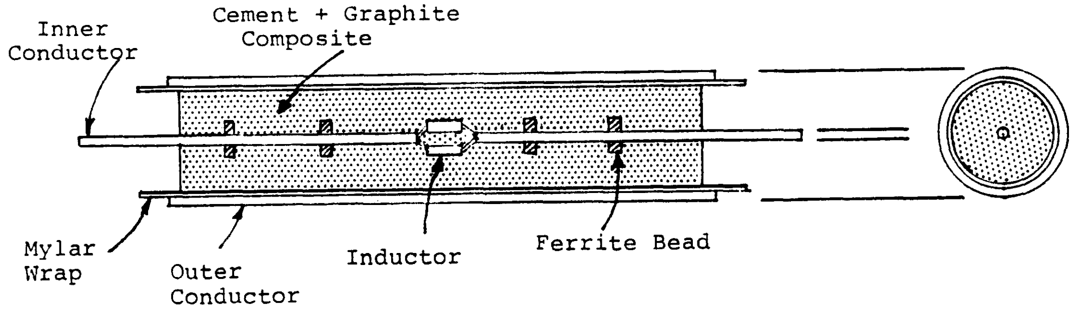

Fig 20.1 RICHARDS' FILTER/ABSORBER FEEDTHROUGH

A few layers of mylar provide insulation. The principle is that the inductors, ferrite beads and graphite all help in attenuating the TEM RF waves. These devices suffered a few problems: (1) the small inductors are not really suitable for the 1.0 A drawn by the filament (2) the devices were not easy to reproduce (3) at least one was found to be leaking RF (possibly one that had been replaced earlier due to a high voltage fault); this was the direct motivation for tackling this problem.

Another scheme is to use a commercial microwave absorbing material that is rated for high voltage to fill a co-axial line (Fig 20.2). Attempts were made using EMAiron 7190 and 8190 (magnetically loaded materials made by Dielectric Communications' Electronautics Division), but the materials failed miserably to meet their high voltage specifications.

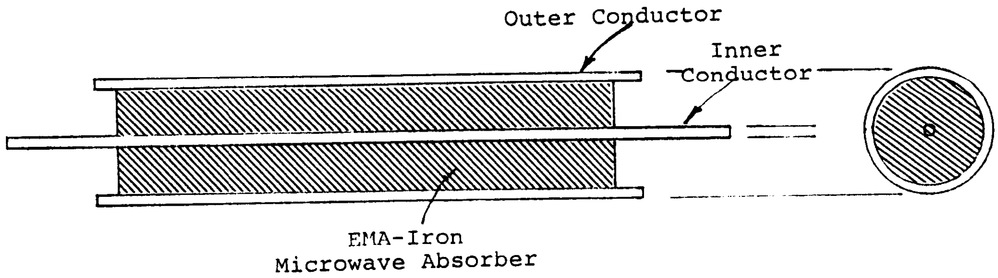

Fig 20.2 ABSORBER-FILLED FEEDTHROUGH

The third scheme is to use a lumped component LC filter implemented as shown in Fig 20.3. The C's are co-axial sections with very small spacing between inner and outer conductors, and the L's are co-axial sections with a coiled thin wire for the center conductor. A few layers of mylar provide insulation. Various configurations were tested and worked well.

The final adopted design has 6-1/2 sections in a 1/2" I.D. 8-5/8" long brass tube. The (brass) C sections are 0.478" diameter and 5/8" long and the L sections are made of 22 gauge tinned copper wire with a single loop in a longitudinal plane; the nominal length of an L section is also 5/8". Two wraps of 1.5 mil mylar provide insulation good to over 11 kV.

The filters were tested for RF tightness by directly measuring transmission of an 0.8 GHz signal and comparing

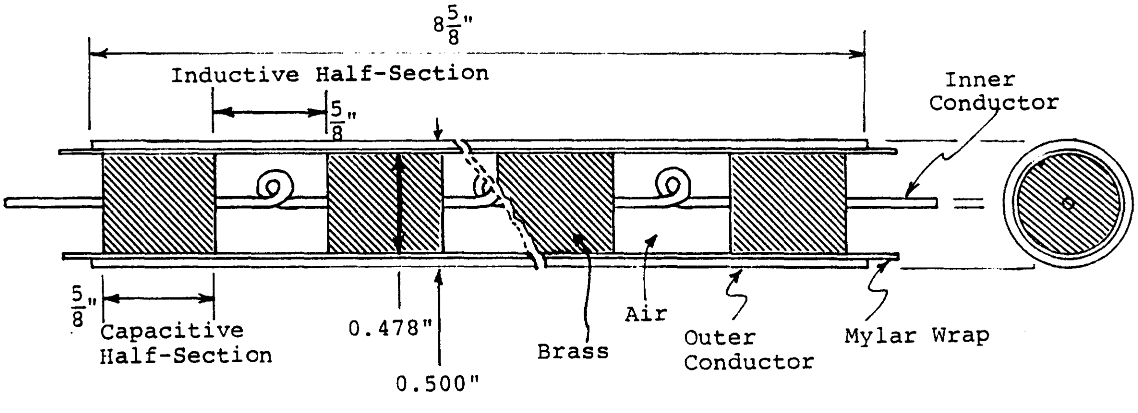

Fig 20.3 6-1/2 STAGE LC FILTER FEEDTHROUGH

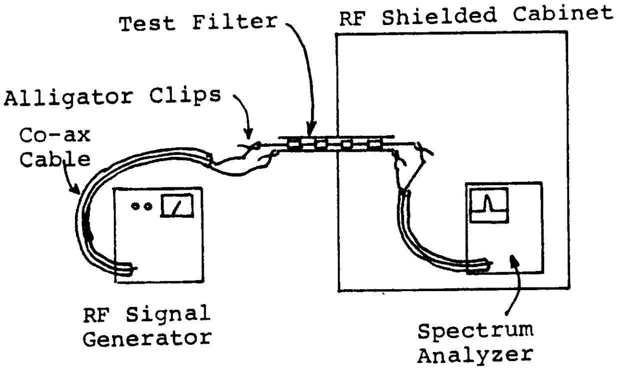

Fig 20.4
FILTER TRANSMISSION TEST SETUP

---

with the transmission of a simple co-axial wire-in-a-tube (so as to account for mismatches and radiative power loss at the input and output of the device; see Fig 20.4.) The difference in transmission is quoted as the filter attenuation. The test results are shown in Table 20.1 for all six devices, measured after installation at both 0.8 and 2.45 GHz. The worst attenuations are 72 dB at 0.8 GHz and 56 dB at the higher frequency.

Table 20.1 MEASURED TRANSMISSION OF 6-1/2 STAGE LC FILTER

Filter #	Transmission (dB) @ 0.8 GHz	Transmission (dB) @ 2.45 GHz
1	-78	-57
2	-72	-68
3	-72	-65
4	-76	-56
5	-76	-61
6	-78	-60

Appendix [21] COMPUTER PROGRAMS

- -

[21.1] Outline

The computer programs used (1) to determine scattering geometries and (2) to analyze data are described in this section.

[21.1] Outline
[21.2] SBATPREP2
[21.3] SCATBACL
[21.4] 2MM4016

The codes are all in FORTRAN for the Data General Nova IV. They are documented and on file at Versator.

[21.2] SBATPREP2

This is the current version of SCATPREP. It performs calculations to determine the geometry required for particular scattering measurements. The user provides (1) the plasma parameters, (2) the location and orientation of the incident and receiving horns, (3) the location of the scattering volume, and (4) the $N_{\|}$ and poloidal orientation of the waves of interest. Provision is made for looping over r/a and $N_{\|}$. The program determines the scattering angle by solving the lower-hybrid dispersion relation, and then computes the appropriate mirror positions. As an option, a sketch of the scattering geometry may be made (Fig 21.2.1). The program also calculates the product CP_L, where C is the factor used to convert measured (normalized) scattered power

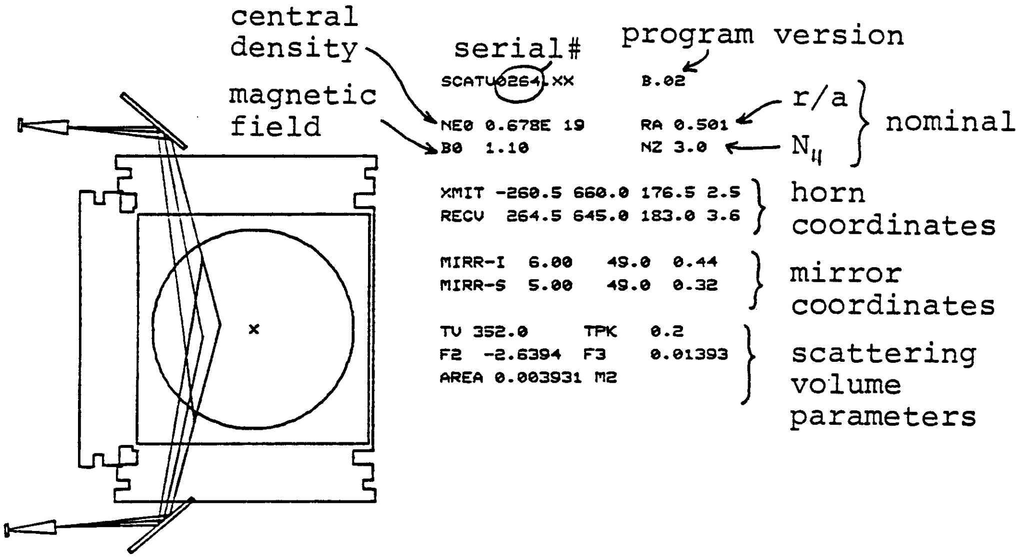

```
SCATU02641.XX          B.02

NE0 0.678E 19          RA 0.501
B0  1.10               NZ 3.0

XMIT -260.5 660.0 176.5 2.5
RECV  264.5 645.0 183.0 3.6

MIRR-I  6.00   49.0  0.44
MIRR-S  5.00   49.0  0.32

TV 352.0      TPK   0.2
F2  -2.6394   F3    0.01393
AREA 0.003931 M2
```

Fig 21.2.1 SCATTERING GEOMETRY PLOT FROM SBATPL2

$\hat{P}_S$ into lower-hybrid wave spectral intensity $\hat{I}(N_\parallel) = C\ \hat{P}_S$ (P_L is the launched lower hybrid wave power).

The plasma parameters to be specified are the line-average electron density and the toroidal field. The program assumes the following: (1) uniform toroidal field, (2) no poloidal field, (3) parabolic density profile, (4) plasma position centered on axis. With this simplified model, subroutine SCATANG calculates the local plasma parameters, and then solves the cold plasma electromagnetic dispersion relation (see Appendix [18.1]) to determine $N_\parallel$ and then the scattering angle θ_S. The electromagnetic dispersion relation is used because the electrostatic dispersion relation was found to be typically off by 10%.

The coordinates used are 2-D Cartesian coordinates in the scattering plane, with the origin at the tokamak center (ie at a major radius of 0). Angles are specified in a [0,360) degree range, with 0° being horizontally outwards and 90° vertically up.

Coordinate geometry calculations are performed by routines SCAT1, SBATRS and SBATM2. SCAT1 identifies the scattering volume location and the incident and scattered rays (rays are specified by a point and a direction). SBATRS finds the points at which the rays are reflected by the mirrors and identifies the ports out of which the incident and scattered rays emerge. SBATM2 finds the mirror locations which appropriately reflect the rays.

Subroutine SBATPL2 makes the scattering volume sketch, which includes the tokamak cross-section (routine CROSEC), the horns (routine PHORN) and mirrors (PMIRR), the central rays through the system, and the side rays at the 3dB points which define the scattering volume. The sketch is annotated with the values of numerous quantities that identify the particular case.

The terms that go into C are calculated in appropriate places; the factor containing plasma and wave quantities is calculated in SCATANG, and the geometry factor is computed in SBATPL2.

[21.3] SCATBACL

SCATBACL, the current version of SCATBACK, complements SBATPREP2 by returning $N_{\parallel}$ and r/a for given mirror positions. The problem is that the mirrors may only be positioned in 1/2" steps and rotated to 1/2° accuracy, and SBATPREP2 returns mirror coordinates of arbitrary accuracy. So some fine-tuning is necessary to get mirror coordinates that may actually be set and yet have the right (or at least close enough) position and scattering angle. With SCATBACL, this fine-tuning may easily be done.

The structure of SCATBACL is very similar to that of SBATPREP2. The user inputs the plasma parameters and horn positions. The program then sits in a loop where the user enters the mirror positions and the program returns the location of the scattering volume and the particulars of the detected wave.

Subroutine SCAT2 traces the (central) rays to the nominal center of the scattering volume. Subroutine SCAT3 determines the local plasma parameters and solves the dispersion relation for $N_{\parallel}$. Subroutine SBATPL2 is used to prepare the optional sketches of the scattering geometry.

[21.4] 2MM4016

This program is used to analyze shot data: it computes scattered power from the measured signal, and also multiplies by the factor C to get lower-hybrid spectral intensity $\hat{I}(N_{\parallel})$.

The experimental data files contain electronically processed data (described in Section 9.8) proportional to the log of the measured power. Program 2MM4016 converts the signal from log to 'real' units and subtracts out the plasma emission and noise from the measured signal. Let V_N be the datafile voltage corresponding to the receiver noise level (measured, for example, on a no-plasma shot). Let F be the electronics calibration factor (in dB/Volt). Then if V_E is the datafile voltage before the lower hybrid pulse is turned on (this corresponds to plasma emission and noise) and V_S is the datafile voltage during the lower hybrid pulse (scattered power plus emission plus noise), the scattered power $\hat{P}_S$ may be calculated (in units of the receiver noise power).

$$P_S = 10^{\frac{F}{10}(V_S - V_N)} - 10^{\frac{F}{10}(V_E - V_N)} \tag{21.4.01}$$

The quantities V_E and V_S are taken by averaging over typically 1/2 ms intervals (6 or 7 points). This calculation assumes that the plasma emission remains unchanged when the RF power is turned on. By measuring V_S within the first millisecond after RF turn-on, the error due to changing plasma emission can be held to less than one noise power unit, entirely acceptable when $\hat{P}_S$ is typically in the 10 to 1000 range. V_E is measured just before RF turn-on.

The user enters (1) data array indices for the two time intervals, (2) the baseline level (= noise power) in computer units, (3) the electronics calibration factor in dB/Volt, (4) the scattering channel on the A-to-D converter, (5) the run number, and (6) the injected lower-hybrid power P_L. The program then sits in an outer loop where the user enters (7) $N_{\parallel}$, (8) r/a and (9) the correction factor CP_L calculated by either SCATBACL or SBATPREP2. At this level the user may change data directories or stop. Within the outer loop is an inner loop where the user enters (10) a shot number, which is analyzed by the program.